Dissertation

submitted to the

Combined Faculty of Natural Sciences and Mathematics

of the Ruperto Carola University Heidelberg, Germany

for the degree of

Doctor of Natural Sciences

Presented by

M.Sc. Johanna von Gerichten

born in Speyer, Germany

Oral examination:

13.11.201

Development of Mass Spectrometric Methods for Tissue Imaging and LC-based Quantification of Glycosphingolipids/Gangliosides including Tay-Sachs disease based Neuraminidase-deficient Mouse Models and Human Gut Microbiota

Referees:

Prof. Dr. Matthias Mayer

Dr. PD Roger Sandhoff

List of figures

List of tables

Summary

Tay-Sachs disease (TSD) is an autosomal-recessive genetic disorder which results in the dysfunction of the metabolic enzyme hexosaminidase A (HexA). It leads to severe lysosomal storage of acidic glycosphingolipid, namely ganglioside GM2, and early fatalities for humans with the infantile on-set form. Despite fifty years of research, to date there is no effective treatment beyond palliative care. It was found that mouse models of HexA deficiency display only moderate GM2 accumulation, which was connected with a late onset neuronal phenotype. Therefore neuraminidases were investigated as possible bypass enzymes for the degradation of GM2 and offer a new opportunity for therapeutic approaches in humans. However, to assess the extent of side effects for such a therapeutic bypass, the substrate specificity and ganglioside (GG) turnover has to be defined in detail. This work presents the development of an HILIC-based LC-MS^2 method as well as mass spectrometry imaging (MSI) using DESI-(QqQ)MS^2 and MALDI-TOF to monitor GG pattern changes in mouse brains. The HILIC-MS^2 analysis of mouse brain tissue with neuraminidase 3 or 4 deficiency in the background of TSD as well as combined knockouts of GG synthesis enzymes revealed an overlapping but distinct substrate processing for the neuraminidases Neu3 and Neu4. MSI of the same tissue samples displayed similar patterns in spatial neural GM2 accumulation that suggest rather a broad distribution of these sialidases in mouse brain. Proposed neuroinflammation and demyelination in mouse brains of TSD led to a modulated HILIC-MS^2 method with which hexosylceramide isomer separation of GG precursor β-glucosylceramide (β-GlcCer) and prominent myelin sheath component β-galactosylceramide (β-GalCer) was achieved. Decreased levels of β-GalCer as a marker for demyelination in brains of TSD combined with neuraminidase deficiency could not be observed at the age of 6 month. Furthermore, proof-of-concept study and screening of various WT mouse tissues revealed the adaptability of this method. Even α-anomeric HexCers could be separated from mammalian β-anomers. In contrast to the mentioned β-HexCers, invariant natural killer T cells are activated most effectively when recognizing galactosylceramide with an α-glycosidic linkage appearing on the cell surface receptor CD1d of antigen presenting cells. One natural bacterial source of this compound in contact with our body is *Bacteroides fragilis*, a bacterial member of the human gut microbiome. This work highlights the detection and separation of α-GalCer(d17:0;h17:0) in *B.fragilis* and three other bacteria of the human gut microbiome β-HexCers. Very recent preliminary studies indicate the identification of an α-glycosidic GalCer in the mouse microbiome with the proposed structure of BdS-α-GalCer(d18:0;h16:0).

Zusammenfassung

Die Tay-Sachs Krankheit (TSK) ist eine autosomal-recessive genetische Funktionsstörung, die in einer Dysfunktion des metabolischen Enzymes Hexosaminidase A (HexA) resultiert. TSK führt zu einer schweren lysosomalen Akkumulation des sauren Gykosphingolipids GM2 und zu einem Tod im Alter von 2-3 Jahren bei der Kindesform der Krankheit. Trotz fünfzig Jahren an Forschung gibt es bis heute keine erfolgreiche Behandlung neben palliativer Pflege. Jedoch wurde entdeckt, dass Maus Modelle mit HexA Insuffizienz nur eine moderate Akkumulation von GM2 aufweisen, zusammen mit einem spät auftretenden neuronalen Phänotyp. In der Folge wurden Neuraminidasen als mögliche Bypass-Enzyme des GM2 Abbaus untersucht und somit eine neue Chance für therapeutische Anwendung im Menschen gefunden. Trotzdem besteht die Notwendigkeit mögliche Nebeneffekte für solch einen therapeutischen Bypass zu ergründen, indem man Substratspezifität und Gangliosid-Umsatz im Detail bestimmt. Diese Arbeit präsentiert die Entwicklung einer HILIC basierten LC-MS2 Methode wie auch massenspektrometrische Bildgebung (MSI) mit Hilfe von DESI-(QqQ)MS2 und MALDI-TOF um Veränderungen im GG Muster des Maus-Gehirn zu verfolgen. Die Analyse von Maushirn-Gewebe mit einem Mangel an Neuraminidase 3 oder 4 im Hintergrund von TSK kombiniert mit knockouts von GG Synthese-Enzymen mittels HILIC-MS2 ließen eine überlappende aber leicht unterschiedliche Substrat-Verarbeitung für Neu3 und Neu4 erkennen. MSI desselben Mausgewebes zeigte ähnliche Verteilungsmuster von neuraler GM2 Akkumulation, die zudem eine breite Verteilung dieser Sialidasen im Maushirn zeigt. Suggerierte Neuroinflammation und Demyelinisierung in Gehirnen von TSK-Mäusen führte zu einer modifizierten HILIC-MS2 Methode mit der Hesosylceramid-Isomere des GG Vorläufers β-Glukosylceramid und β-Galaktosylceramid (β-GalCer), welches als Myelinscheiden Bestandteil bekannt ist, getrennt werden können. Verringerte Mengen an β-GalCer als Marker für Demyelinisierung in Gehirnen von TSK-Mäusen im Alter von 6 Monaten kombiniert mit Neuraminidase Defekt konnten nicht bestätigt werden. Weiterhin wurde eine proof-of-concept Studie durchgeführt, wobei verschiedenste Wildtyp-Mausgewebe analysiert wurden um die Anwendbarkeit dieser Methode, auch für α-anomerische HexCer, zu demonstrieren. Im Gegensatz zu den bereits erwähnten β-HexCers, werden invariante natürliche Killer T Zellen am effektivsten aktiviert, wenn sie Galaktosylceramid mit eine α-glykosidischen Bindung am Zelloberflächen-Rezeptor CD1d von Antigen präsentierenden Zellen erkennen. Eine natürliche Quelle für dieses α-GalCer in Verbindung mit dem menschlichen Körper stellt das Bakterium *Bacteroides fragilis* dar, ein Mitglied des menschlichen Darm Mikrobioms. Diese Arbeit zeigt ebenso die Detektion

und Trennung der β-HexCers von α-GalCer(d17:0;h17:0) im *B.fragilis* und drei weiteren Bakterien des menschlichen Darm-Mikrobioms. Des Weiteren werden einleitende Studien zur Identifikation eines α-glykosidischen GalCer gezeigt, welches im Maus Mikrobiome detektiert wurde, und die berechnete Struktur von BdS-α-GalCer(d18:0;h16:0) aufweist.

1 Introduction

The first aim of this work was to develop a LC-MS/MS method for the robust and reproducible analysis of gangliosides, acidic glycolipids, in mouse tissue. The method developed was used to screen mouse brain samples for pattern changes in the ganglioside metabolism when neuraminidase and/or ganglioside-synthesis enzymes are deleted in mouse strains with Tay-Sachs disease or GM2 gangliosidosis background. The results were expected to conclude the degree to which ganglioside substrates were processed by neuraminidase 3 and 4. Additionally, an imaging mass spectrometry (MSI) method based on desorption electrospray ionization (DESI), was set up for the tissue analysis of gangliosides. The results were compared with the commonly used MSI ionization technique Matrix-associated laser desorption/ionization (MALDI) to assess the benefit of DESI-MS/MS. Tissue sections of the above mentioned brain samples were screened for GM2 accumulation with a MALDI time-of-flight (TOF) instrument. Differences in local ganglioside distribution were monitored to combine these results with other detection techniques such as immunohistochemistry and *in situ* hybridization for neuraminidase. All of this to gain insight into the correlation between loss of neuraminidase activities and GM2 accumulation.

The second aim of this work originated from the first. An LC-MS/MS method for the separation of hexosylceramide isoforms in the brain was needed to distinguish the precursor of neuronal gangliosides (glucosylceramide) and the abundant myelin-component galactosylceramide (cerebroside). Galactosylceramide and Glucosylceramide differ only in the stereochemistry of the hydroxyl group in 4-position of the sugar ring. Thus they cannot be separately detected by mass spectrometry (neither MS^1 nor MS^2) alone. Therefore a HILIC-MS^2 based method for the separation of these diastereomers, including their corresponding α-anomers, was developed. As proof-of-concept, a wide range of different WT mouse tissues and various genetically modified mouse tissues were screened for the verification of the different hexosylceramide species as well as bacteria strains related to the human gut microbiome. *Bacteroides fragilis,* a member of the human gut microbiome, expresses an α-glycosidically linked galactosylceramide in contrast to the mammalian β-linked anomers. The α-anomeric galactosylceramide is of special interest for the field of immunology. It is so far the most competent ligand to stimulate invariant natural killer T cells (iNKT cells), when presented on CD1d of antigen presenting cells (APCs). Here, α-GalCer was proofed to differentiate from β-HexCers with the developed HILIC-MS^2 method. Therefore, as in human gut microbiota, a

search for a corresponding component in the intestinal tract and gut microbiome of the model organism mouse was performed.

1.1 Glycosphingolipids

Glycosphingolipids (GSL) are glycosylated derivatives of sphingolipids with a core formed by ceramide. Ceramide is an amino alcohol composed of a fatty acid linked by an amide bond to a long chain base (sphingoid base), most commonly sphingosine (Figure 1 A). Thus, GSLs are amphipathic molecules consisting of a hydrophilic carbohydrate head group and a hydrophobic anchor [1]. They are widely found on the outer leaflet of plasma membranes in eukaryotic cells, as well as in some prokaryotic organisms and viruses. Their specific functions in cellular processes are dictated by their structural diversity [2–9]. In their simplest forms sphingosine, phytosphingosine (4-hydroxysphinganine) and dihydrosphingosine (sphinganine) serve as the backbone of ceramide combined with the fatty acid moiety. They differ in chain length, degree of saturation, hydroxylation and esterification, which leads to a huge molecular variation of ceramide anchors. This complexity is further enhanced by the combination of different carbohydrates such as glycan residues and neuraminic/sialic acid in their head group (Figure 1 B and C). GSLs are divided broadly into two categories depending on their glucosylceramide (GlcCer; glucocerebroside) or galactosylceramide (GalCer; cerebroside) base for further synthesis. GlcCer based GSLs are further defined into different series depending on the structure, including (neo)lacto-, (iso)globo-, ganglio- and muco-series (Figure 2).

1.1.1 Hexosylceramides

Hexosylceramides (HexCer) consist of a ceramide backbone with a monosaccharide residue added as head group (Figure 1 B). In mammalians the most common forms of HexCer are glucosylceramides (GlcCer) and galactosylceramides (GalCer). Whereas GlcCer appears to be omnipresent in almost all cell types of the mammalian body, GalCer has mainly been restricted to the brain, especially myelin structures, and to the kidneys [10,11]. The glycosidic linkage to ceramide is of the β configuration in mammalian lipids. Enzymes catalyzing the production of corresponding α-anomers in mammals have not been observed so far. However, recently it has been proposed that, at very low levels, α-GalCer is endogenously present [12]. Nevertheless, other species such as the marine sponge, *Agelas mauritianus*, and bacteria such as *Bacteroides fragilis*, have been shown to produce α-GalCer [13,14].

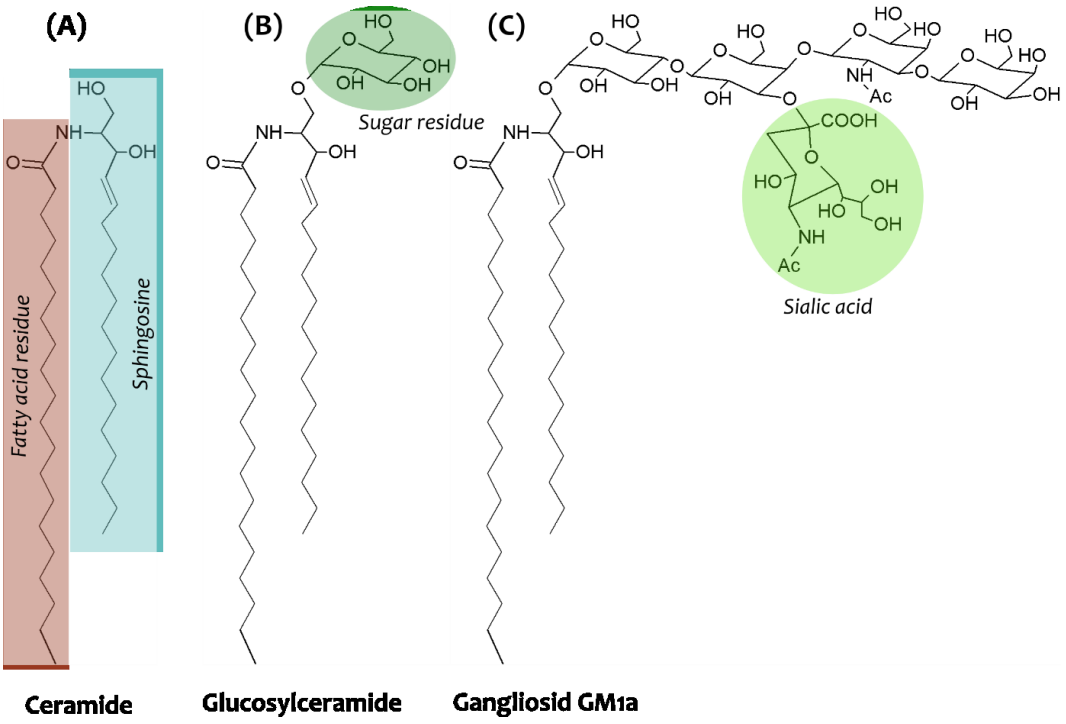

Figure 1: Structure of ceramide, simple and complex glycosphingolipids (GSL). A) Ceramide displaying the typical composition of a long chain base, in this case sphingosine (blue; d18:1), and a fatty acyl chain (red; 18:0). B) β-Glucosylceramide as the simplest GSL reflecting a ceramide with a glucose attached as head group (dark green). C) Ganglioside GM1a as one of the most prominent gangliosides present in the brain with a neutral tetrasaccharide added to a ceramide backbone and an additional sialic acid group (light green).

1.1.2 Gangliosides

In 1942 Ernst Klenk first discovered gangliosides (GG) in brain extracts from patients with amaurotic familial idiocy and Niemann-Pick disease. He labelled them after their predominant location in ganglion cells [15]. The first correct chemical structure was described for the complex ganglioside GM1 (Figure 1 C), which is part of the a-series of neuronal GGs [16]. The basic composition of GGs, ceramide-Glc-Gal-NeuNAc (GM3), expands with one or more varying hydrophilic oligosaccharides that are linked in 1-*O*-position to a hydrophobic ceramide anchor. Most of them contain at least one *N*-acetyl neuraminic acid in the head group. There are more than 60 different ganglioside structures present in almost all tissues and organs of vertebrates with cell type specific expression. Nevertheless GGs are highly enriched in neuronal membranes [1,17,18]. In most tissues GG expression changes during development, for example as the brain develops, the expression of simple gangliosides (GM3, GD3) is down-regulated with parallel up-regulation of complex gangliosides such as GM1a, GD1a, GD1b and GT1b, representing the GG composition of mature neurons (Figure 2)[19]. Adjacent to the influence of the glycan properties on molecular interactions, structural properties play an important role as the long chain base of the ceramide anchor for brain GGs shifts from palmitic acid (d18:1) to

stearic acid (d20:1) during aging [20]. Gangliosides, as part of the outer leaflet of the plasma membrane can participate in microdomains, serve as ligands of lectins and attune the activity of transmembrane proteins such as insulin receptor, leptin receptor or EGF receptor [21–24].

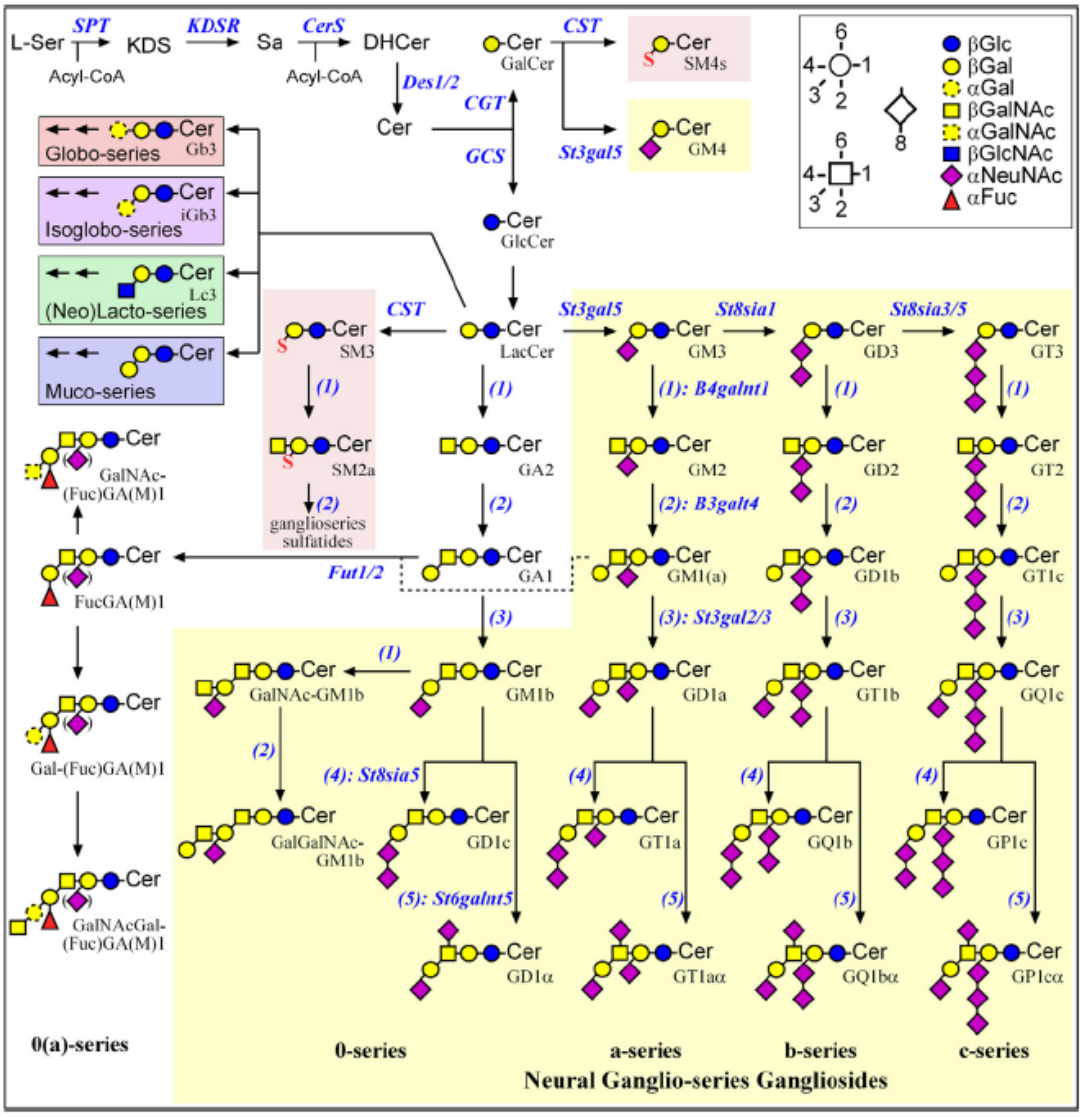

Figure 2: Glycosphingolipid biosynthesis [4] with the focus on glucosylceramide (GlcCer) based synthesis of gangliosides (light yellow).

1.2 Metabolism of Hexosylceramides and Gangliosides

1.2.1 Biosynthesis of Hexosylceramide and Gangliosides

De novo biosynthesis of glycosphingolipids is described according to the reviews of Jennemann and Gröne, and Sandhoff *et al* [4,5]. The first steps of biosynthesis are initiated in the cytosolic side of the endoplasmatic reticulum (ER), where the basis for all sphingolipids,

ceramide, is formed (Figure 3). There, serine palmitoyltransferase (SPT) condensates the amino acid L-serine and an activated fatty acid into 3-Ketosphinganine, which is then reduced into sphinganine by 3-ketosphinganine reductase (KDSR). One of six different ceramide synthases (CerS1-6) proceed sphinganine by *N*-acylation with an activated fatty acid to gain dihydroceramide Likewise, sphingosine from the salvage pathway can be directly acylated to produce ceramide. Dihydroceramide is converted by dihydroceramide desaturase into ceramide with sphingosine (DES1) or phytosphingosine (DES2). In the luminal side of the ER galactosylceramide (GalCer) is synthesized by modulating ceramide with UDP-GalCer via β-galactosylceramide synthase (UGT8A). Additionally, ceramide is transported to the Golgi by vesicles or ceramide transfer protein (CERT), where glucosylceramide synthase (UGCG) transfers Glc to ceramide from UDP-Glc, and GlcCer is released in the cytosolic leaflet of the early Golgi membranes. Complex gangliosides (GG) are synthesized by stepwise addition of monosaccharides to GlcCer on the luminal side of the Golgi membrane. This means GlcCer has to flip to the other side of the bilayer. The primary addition of UDP-Gal by galactosyltransferase (B4Galt5/6) reveals lactosylceramide (LacCer), which is a branching point of complex GSL synthesis. The first and basic ganglioside GM3 is synthesized via transfer of sialic acid from CMP-sialic acid to LacCer in α-2,3-linkage by GM3/GM4-sialyltransferase ST3GalT5. GM4, which results from GalCer after vesicular transport to the Golgi, is a minor component of the brain and little is known about its biological function. More abundant in the brain are sulfatides which are synthesized by the cerebroside sulfotransferase (CST), converting GalCer or LacCer to form SM4s or SM3. Furthermore, LacCer is used as substrate to the globotriaosylceramide synthase (Gb3S) starting the neutral glycosphingolipid pathway of the globo-series. The first step in this pathway is the addition of galactose in α-glycosidic linkage to LacCer forming Gb3. GM3 in the ganglio-series can be further sialylated into GD3 via GD3-synthase (St8sia1), with a second sialic acid in α-2,8-linkage to the first sialic acid, and additional sialylation by sialyltransferase (St8sia3/5) forms GT3. Downstream, glycosyltransferases for the synthesis of complex GGs are mediated in enzyme multisystem. These are often arranged in a modular organization in homo- or hetero-multienzyme complexes in the membranes of the Golgi and trans-golgi network (TGN). LacCer, GM3, GD3 and GT3 are substrates for *N*-acetylgalactosaminyl transferase (B4galnt1), which transfers *N*-acetyl galactosamine (GalNAc) in β-1,4-linkage to form GA2, GM2, GD2 and GT2. This is the prior step dividing the gangliosides into four groups, the 0-, a-, b- and c-series. Depending on their basic horizontal GG they are synthesized from (Figure 2). Likewise, the

next steps are processed by a galactosyltransferase (B3galt4) resulting in GA1, GM1a, GD1b and GT1c, and then by sialyltransferase (St3gal2/1) gaining GM1a, GD1a, GD1b and GT1b, the major brain GG's (Figure 3).

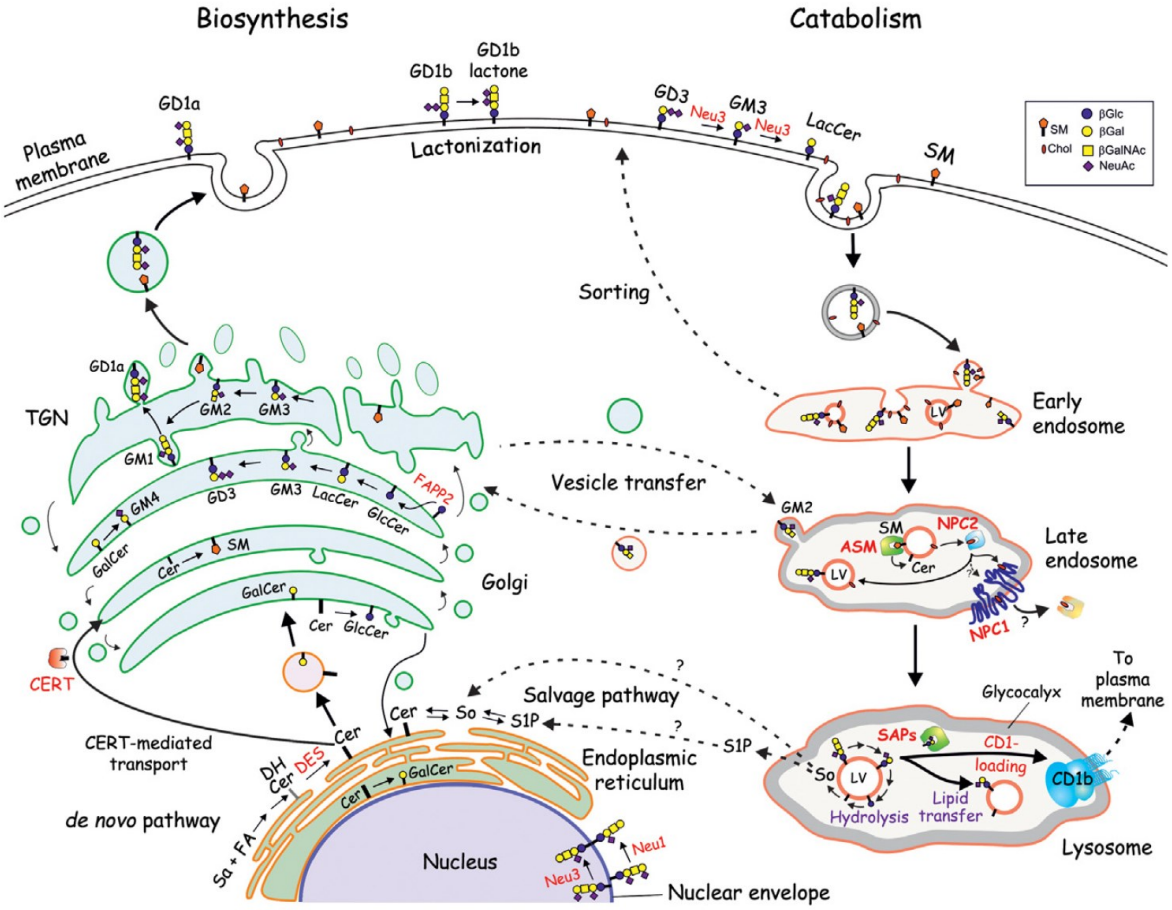

Figure 3: Subcellular compartmentalization and intracellular trafficking of hexosylceramide and ganglioside biosynthesis and catabolism [4].

1.2.1.1 GalCer-Synthase (UGT8A) mouse model

Galactosylceramide synthase, encoded by the *Ugt8a* gene, catalyzes the formation of galactosylceramide (GalCer) by adding galactose from UDP-galactose to ceramide. GalCer mainly occurs in neural cells such as oligodendrocytes (CNS) and schwann cells (PNS) and is highly enriched in myelin sheaths that covers axons (together with its sulfated form SM4s; Figure 2). Initially, two independent groups had generated *Ugt8a*-deficient mouse lines through convential targeting of the *Ugt8a* gene [25,26]. Homozygous *Ugt8a*$^{-/-}$ mice were viable and expressed higher levels of glucosylceramide (GlcCer) which nonetheless do not compensate the GalCer depletion. Additionally, the sulfated derivative of GlcCer were synthesized, as well as a higher amount of α-hydroxy fatty acids in their ceramide moiety. These mice were smaller

in size with a shortened life span and displayed tremors, loss of locomotor activity and disruption of nerve conduction. With the GlcCer produced to balance the lacking GalCer, oligodendrocytes and schwann cells were able to form only slightly thinner myelin sheaths. These however, became unstable and degenerated in older mice. Thus, GalCer synthesis is needed for long-term maintenance of the myelin structure and function.

1.2.1.2 GlcCer-Synthase (UGCG) mouse model

Glucosylceramide synthase encoded by the *Ugcg* gene catalyzes the formation of glucosylceramide (GlcCer) by adding glucose from UDP-glucose to ceramide. GlcCer is the main basis for glycosphingolipid (GSL) biosynthesis and when modified gives rise to hundreds of complex GSLs (Figure 2). Systemic disruption of *Ugcg* caused embryonic lethality starting at stage E7.5 [27]. To study the influence of GlcCer and especially the gangliosides in the brain a floxed *Ugcg*$^{-/-}$ mouse line combined with strains expressing *Cre* recombinase transgene under the control of different promotors was established. The first Cre/loxP system was developed by two different groups with *Ugcg* under the nestin promotor. This is expressed early in neuronal cells during development from day E9.5 [28,29]. These mice appeared normal at birth but showed severe neurological dysfunctions, defects in axonal branching, hypertrophic neurons and broadened myelin sheath. Additionally, in one of the two generated mouse lines all animals died within 3 weeks after birth. This was due to the lower level of residual *Ugcg* expression. Together, these reports show that GlcCer-based GSL synthesis is required for neuron differentiation, brain maturation and stability after birth. Another mouse line deleted functional *Ugcg* under the L7 promotor, which is only expressed in Purkinje cells [30]. Mice showed Purkinje cell degeneration and abnormal myelination, implicating a role for GSLs in axonal-glial interactions. In a separate study of neuronal-specific deletion of *Ugcg,* the neuronal calcium/calmodulin-dependent kinase II α (*CamK*) promotor was used for an inducible *Cre* recombinase (Cre-ERT2) [23]. Lacking GSLs in the forebrain leads to progressive body weight gain, hypometabolism and hypothermia. Furthermore leptin and insulin[31] signalling was impaired which could be connected to the absence of gangliosides and their interaction with the corresponding insulin and leptin receptors on the plasma membrane. Oligodendrocyte specific deletion of *Ugcg* was achieved by using myelin-associated enzyme 2', 3' cyclic nucleotide 3' phosphodiesterase (*Cnp*) promotor, where mice showed no myelin abnormalities. Therefore these GSLs are not essential for myelin structure and stabilization [32]. Besides research for the role of GlcCer and specifically gangliosides in the nervous system, there were a lot of other cell type-specific *Ugcg* KO mouse lines developed to show the

importance of GSLs in varying tissue types such as in hepatocytes of the liver (*AlbCre*) [33], enterocytes of the intestine (VilCre) [34], tubular epithelial cells of the kidney (*Pax8Cre*) [35] and keratinocytes of the skin (*K14Cre)* [36].

1.2.1.3 Cerebroside sulfotransferase (GAL3ST1) mouse model

Cerebroside sulfotransferase (CST) catalyzes the 3-*O*-sulfation of terminal galactosyl moieties on GSLs such as galactosylceramide. Thereby forming the sulfatide SM4s, which is most prominent in oligodendrocytes (CNS) and schwann cells (PNS) [37–40] (Figure 2). Additionally, high amounts of SM4s can be found in kidney, gastric mucosa, lung and endometrium. *CST*$^{-/-}$ mice were normal at birth but developed severe neurological defects due to myelin vacuolization, degeneration and deformation, as well as impaired ion channel cluster formation [41–43]. Primary cultures of *CST*$^{-/-}$ mice showed increased oligodendrocyte maturation and therefore the role SM4s play as a negative regulator of oligodendrocyte maturation [44]. Mice with a deletion of *CST* under the *Pax8* promotor displayed a normal kidney morphology but lower pH and less ammonium excretion in the urine indicating the critical role of sulfatide for physiologic acid-base homeostasis [35].

1.2.1.4 Gb3-Synthase (A4GALT) mouse model

Gb3 synthase (Gb3S) forms Gb3 by addition of a α-1, 4-linked galactose to lactosylceramide (LacCer) and this initiates the globo-series of glycosphingolipids (Figure 2). The first developed mouse line with a Gb3S deficiency appeared normal and lacking in any phenotype. Therefore these mice were protected from the bacterial endotoxin shigatoxin [45]. *Gb3S*$^{-/-}$ mice generated by another group showed an increased amount of LacCer and an involvement of Gb3 in invariant NKT cell number [46]. Latest investigations revealed albuminuria in these mice, apparently due to reduced endocytic uptake in renal proximal tubular epithelia cells [47].

1.2.1.5 GM3-Synthase (ST3GAL5) mouse model

GM3 synthase (GM3S) transfers a sialic acid to lactosylceramide in α-2, 3-linkage to form GM3, the simplest of the gangliosides. In mice deficient in GM3S all a-, b- and c-series gangliosides are absent in the brain and substituted by 0-series gangliosides GM1b, GD1c and GD1α [48,49] (Figure 2). These mice showed neither major neurological phenotype nor histological abnormalities in brain, but are protected from high-fat diet-induced insulin resistance. The diabetic wound healing defect in diet-induced obese mice is prevented[50], and neuropathic pain and small fiber neuropathy is reversed in diet-induced diabetic mice[51]. Additionally, a gender-specific impairment of neuropsychological behaviors in juvenile *GM3*$^{-/-}$ mice was observed [52].

1.2.1.6 GD3-Synthase (ST8SIA1) mouse model

GD3 synthase (GD3S) adds another sialic acid to ganglioside GM3 in α-2, 8-linkage to form GD3 and thereby catalyses the synthesis of b-series gangliosides (GD3, GD2, GD1b, GT1b and GQ1b) (Figure 2). *GD3S*$^{-/-}$ mice show no apparent abnormalities in brain development and exhibit a normal life span, concluding that b-(and c-)series gangliosides are not necessary for neuronal differentiation [53–55]. The loss of b-series gangliosides was compensated by a corresponding increase of a-series GGs, mainly GM1a and GD1a as well as increased GT1aα. Initially, the disruption of hypoglossal nerves in GD3S deficient mice showed a reduced regeneration and decreased number of surviving neurons [53], and another study showed morphological abnormalities in the sciatic nerve and decreased peripheral nerve regeneration [56]. Additionally, reduced expression of EGFR was observed together with a diminished self-renewal of neuronal stem cells, indicating an interaction of GD3 or b-series GGs with the EGF receptor [57]. Similar GD3 deficiency was linked to impaired neurogenesis due to progressive loss of hippocampal neural stem cells, associated with depression-like behavior [58]. In mouse models of Alzheimer and Parkinson the lack of b-series gangliosides revealed protective traits, evident by less accumulation of aβ-plagues and reduced neurodegeneration [59–61].

1.2.1.7 N-acetyl-galactosaminyl transferase (B4GALNT1) mouse model

β-1, 4-GalNAc transferase (Galgt1; GM2/GD2 synthase) catalyses the transfer of UDP-activated *N*-acetyl-galactosamine to lactosylceramide, GM3 and GD3, and thereby synthesizing all neuronal complex gangliosides (Figure 2). Galgt1$^{-/-}$ mice show only minor neurological abnormalities, but a decreased myelination of central axons led to motoric symptoms with age [62–66]. Additionally, gangliosides, which are ligands of MAG displayed by oligodendrocytes to promote axon-glia interactions and decreased levels of MAG expression were observed in these mice only expressing GM3 and GD3 [63,67]. Mice depleted of complex gangliosides revealed impaired capacity for calcium regulation and degeneration in the presence of depolarizing levels of potassium and glutamate [68,69].

1.2.2 Catabolism of Hexosylceramide and Gangliosides

The constitutive catabolic pathway of glycosphingolipids (GSL) and gangliosides (GG) finalizes via numerous vesicle trafficking pathways including endocytosis, phagocytosis and autophagy in lysosomes (Figure 3). Lysosomes are small organelles with an acidic interior (pH4-5), in which soluble hydrolases degrade a variety of macromolecules and complex lipids to release corresponding breakdown components into the cytosol for recycling, nutrient sensing and membrane repair (salvage pathway). Their limiting membrane is spanned by the glycocalix containing numerous transmembrane proteins which are highly glycosylated at the luminal side. This protects proteins and lipids at the lysosomal perimeter membrane from hydrolytic digestion. GSLs and GGs catabolism starts in late endosomes where a protein machinery known as ESCRT mediates the inward budding of the endosomal perimeter membrane with continued budding off into luminal space and sorts this into intralysosomal luminal vesicle (LV). The degradation of GSLs and GGs occurs at the surface of LV's in a stepwise fashion, releasing monosaccharide units from the non-reducing end of the oligosaccharide chain (Figure 4). As the lipid substrates for the degrading soluble hydrolases are embedded into vesicles, five small non-enzymatic glycoproteins mediate the interaction. These are saposins (SAP A-D) and GM2 activator protein (GM2AP). Additionally, removal of the terminal sialic acid unit via sialidases (neuraminidases) is an important step in GG degradation that could have already taken place at the plasma membrane or later in the early and late endosomes. The mono-sialylated GGs are further degraded by surface-bound lysosomal enzymes. GM1 is processed into GM2 by the removal of terminal galactose with GM1-β-galactosidase in the presence of GM2AP or Sap B. GM2 is then degraded via the cleavage of terminal *N*-acetylgalactosamine by β-hexosaminidase A (HexA) and assisted by GM2AP to form GM3. α-Sialidase and Sap B finally modulate GM3 into LacCer by removing the sialic acid [2,4,70].

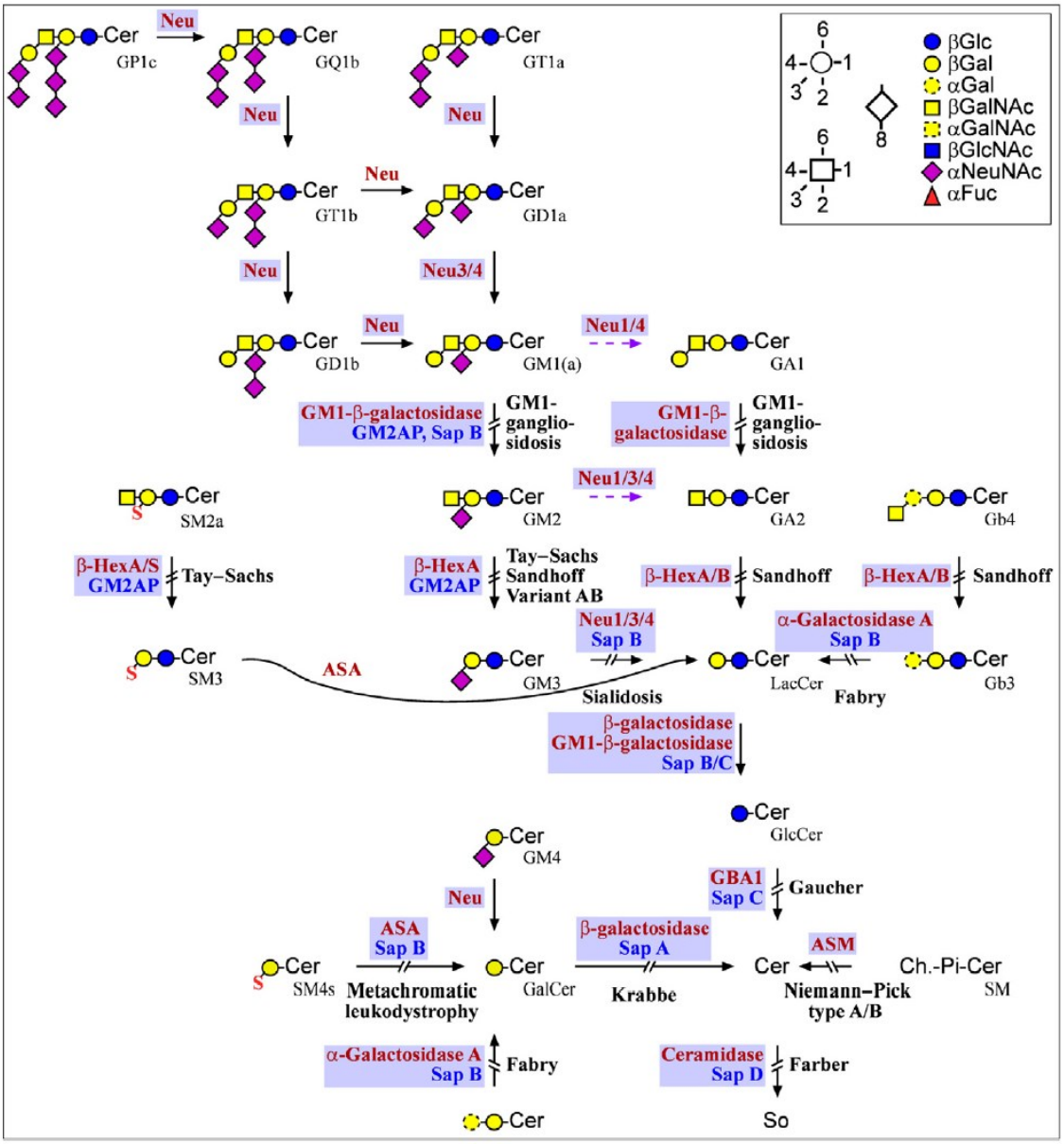

Figure 4: Lysosomal ganglioside catabolism [4].

1.2.2.1 Neuraminidases (Sialidases)

Complete degradation of Gangliosides (GG) occurs in lysosomes, whereas initial steps by some neuraminidases/sialidases can take place at the plasma membrane. Sialidases cleave off the non-reducing sialic acid that is glycosidically linked to the glycan head group of GG (Figure 4). There are four isoforms of neuraminidases based on their initial subcellular localization. These are Neu1 in lysosomes, Neu2 in the cytosol, Neu3 at the plasma membrane, endosomes and lysosomes, and Neu4 in lysosomes, mitochondria and/or intracellular membranes [71]. In the brain only Neu1, Neu3 and Neu4 hydrolyze sialic acid residues from GGs, whereby Neu1 acts only as part of a multienzyme complex with β-galactosidase and cathepsin A in the lysosomes [72–76]. Neu3 is not only located at the plasma

membrane, but also facing inward on membranes of endosomes and lysosomes, consistent with its two pH optimum at pH 4.6 and pH6-6.5 [77–80]. Its main substrates have been described *in vitro* to be GM3 and disialo-gangliosides such as GD1a and GD3, and a minor activity toward GM2, GM1 and GT1b [81–85]. Neu4 is more widely distributed in cellular membranes such as ER, mitochondria and lysosomes [86–88] and the main substrate in the brain is presumably GD1a [89].

1.2.2.2 β-glucosylceramidase (GBA2) mouse model

The non-lysosomal β-glucosylceramidase GBA2 degrades glucosylceramide (GlcCer) to glucose and ceramide. It is ubiquitously distributed in tissues, but mainly expressed in brain, heart, skeletal muscle, testis and kidney, and to minor levels in small intestine, spleen, liver and lung [90,91]. *Gba2*$^{-/-}$ mice showed increased homeostatic levels of GlcCer in brain, liver and testis. While not any impairment was observed in the central nervous system, these mice displayed decreased fertility, and dysfunction of the liver [92].

1.3 GM2-gangliosidosis: Tay-Sachs disease

Tay-Sachs disease (TSD) is a lysosomal storage disease and one of three GM2-gangliosidosis forms that result from defects in degradation of GM2 and related glycolipids by hexosaminidases and GM2 activator protein (GM2AP) [93,94] (Figure 4). GM2AP is a non-enzymatic protein that mediates interaction between the water-soluble enzyme hexosaminidase A (HexA) and its membrane-embedded substrate GM2 at the lipid water interface. Depending on the types of hexosaminidases or if there is a defect in GM2AP, three clinical phenotypes are known. Whereas the hexosaminidase type depends on the combination of the two subunits α and β, defects in the α-subunit are associated with TSD and affect mainly the catalytic activity of HexA (αβ). HexA cleaves terminally linked *N*-acetylhexosamine from acidic glycosphingolipids. Hexosaminidase B (ββ) cleaves *N*-acetylhexosamines only from uncharged GSLs such as GA2 or Gb_4Cer. Defects in the beta subunit are known as Sandhoff disease and affect HexA (αβ) and HexB (β/β) activities, but not those of the minor component HexS (α/α). The minor isoform HexS degrades sulfated glycolipid SM2a as well as GM2 and GA2 [95]. Tay-Sachs disease is an autosomal-recessive disorder mainly detected in patients with a Jewish background, especially in populations of Ashkenazi Jews with ancestry in Middle and Eastern Europe. There are three on-set forms of this disease, depending on residual HexA enzyme activity. An infantile form leading to death within 3-5 years, a juvenile form showing severe phenotypes between 5-15 years and an adult form diagnosed in the patients late teens. The infantile form is clinically characterized by

blindness, paralysis and dementia due to massive neurodegeneration and occurs in 1 out of 4000-6000 Jewish births and 1 out of 300.000-500.000 non-Jewish births, respectively. To date there is no effective treatment beyond palliative care despite the research for several treatment approaches such as gene therapy, inhibitors, cord blood transplant, chaperone therapy, stem cell therapy and enzyme replacement therapy [70,96–100]. Nevertheless, the detailed molecular and cellular events remain to be delineated, e.g. with adequate mouse models. Mutations in the β subunit of β-hexosaminidase, leading to Sandhoff disease, and therefore the elimination of both HexA and HexB showed a severe neurological phenotype. In contrast, mice lacking HexA and HexS via a mutation in the α subunit show no significant neurological phenotype in comparison to TSD patients with high neurodegeneration and an infantile onset variant. The reason is mouse sialidases do to some extent bypass in vivo GM2 storage by degrading GM2 slowly to GA2 which is substrate for the remaining intact isoenzyme HexB [101]. The latter is not observed in humans, either because GM2 is not substrate for human sialidases or because corresponding human sialidases are not expressed in corresponding tissues in sufficient amounts. The involvement particularly of sialidases Neu3 and to a lesser extent Neu4 in this bypass were recently demonstrated in mice [85,89,102].

1.4 Glycosphingolipids in T cell immune response

Glycosphingolipids can be recognized by a T cell lymphocyte subpopulation known as invariant natural killer T cells (iNKT) that only recognizes lipids presented by the MHC class I-like protein CD1d [103,104]. The T cell receptor (TCR) of iNKT cells is limited to a single α chain combined with a restricted selection of TCR β chains, while CD1d is mainly expressed on B-cells, dendritic cells, macrophages and epithelial cells. Presented antigenic lipids require lysosomal trafficking of CD1d as well as lipids, and the assistance of lipid transfer proteins (Saposins, GM2AP) for sufficient CD1d-lipid loading [105–107]. The interaction of presented lipids by dendritic cells with the TCR of iNKT cells activates these iNKT cells and triggers the release of a variety of cytokines and chemokines modulating and/or stimulating the immune system [108]. Hence, the interest in iNKT cells stems from their respons to endogenous and exogenous (e.g. microbial) lipid antigens, as well as their potential to activate adaptive (T and B cells) as well as innate (dendritic and NK cells) immune response [109–112]. The lingering research for possible self-lipid antigens for iNKT cells is based on the involvement of these cells in many autoimmune diseases. These are, for example, type 1 diabetes, multiple sclerosis, rheumatic arthritis and asthma, as well as cancer and host defense to bacteria, fungi and viruses [113,114]. Nevertheless, the first identified CD1d antigen was a foreign lipid found in a marine sponge

(*agelas mauritianus*) and identified as galactosylceramide with an α-glycosidic linkage and a phytosphingosine in the ceramide backbone [13]. Over the last years a variety of endogenous lipids were reported, starting with the neutral glycosphingolipid iGb3, which was found because of decreased iNKT cell number in HexB deficient mice. However, the relevance of iGb3 was complicated by the lack of iGb3 synthase in humans and the lack of impact on iNKT cells in iGb3 synthase deficient mice [115–117]. Others tried and partially succeeded to identify lipid antigens via co-precipitation of lipids within the CD1d complex such as lysophosphatidylcholine (LPC), phosphatidylinositol (PI) and peroxisome-derived ether-bonded phosphoethanolamine (eLPA and pLPE) [118–121]. Additionally, there are GSLs identified by direct testing of synthesized or purified cellular lipids such as β-hexosylceramides [122–125], β-LacCer [126], GD3 [127,128] and sulfatide [129]. Until now, however, α-GalCer remains the most potent activator of iNKT cells when presented vial CD1d. Currently under investigation is the potential of endogenous (mammalian) α-GalCer and the natural stimulation of iNKT cells via CD1-presented α-GalCer from members of the gut microbiome [14,130,131].

1.4.1 Microbiota and Inflammation

Humans share most of the same gut bacterial species, a core microbiota which is dominated by two anaerobic bacteria the Firmicutes and Bacteroidetes [132]. The composition of the gut microbiome is affected by host phenotype, genotype, immune function and diet. The colonic mucosa is constantly exposed to gut microbiota and therefore the bacterial stimulation of the immune system. Inflammation in the intestinal tract has been shown to cause reduced barrier function that enables bacteria to interact with the epithelium and lead to lesions in the epithelium with bacterial translocation [133,134]. Additionally, inflammation can result in the enrichment of certain bacterial groups that have pro-carcinogenic traits such as *Bacteroides fragilis* [135]. Vice versa, *B.fragilis* were reported to cause diarrhea and colitis, which results in a higher risk for cancer [136,137]. More detailed, *B. fragilis* has been shown to negatively regulate iNKT cells in mice colons by acting as a competitive inhibitor, instead of a true antagonist, when not exposed in early life [138]. Nevertheless, the glycosphingolipid α-GalCer produced and isolated from *B.fragilis* was shown to stimulate mice and human iNKT cells [14]. Applying high fat diet to mice for obese mouse models and analyzing the gut microbiome resulted in a reduction of Bacteroidetes and an increased risk of developing colitis [139,140]. Currently, there are a lot of questions left regarding the understanding of host-microbiome interaction and how specific molecules/lipids and immune mechanisms of microbes effect health issues.

1.5 Analysis of Glycosphingolipids

The analysis of glycosphingolipids (GSL) and its complexity is dependent on the degree or type of information required. A robust and stable way to perform GSL analysis is thin layer chromatography (TLC). It is adequate to show an overview pattern of the GSLs in the selected tissues or cells. However, it is dependent on the standards available and difficult for the identification of unknown structures as well as improper for detailed structure analysis of, for example, the ceramide anchor. The use of mass spectrometry (MS) exposes a lot of different techniques and information depth. There are 'untargeted' approaches where high-resolution mass spectrometry is used to compare sets of samples (healthy/diseased; control/treated) to show changes in tissues/cells (fingerprint analysis), but lacking in the structural information of the lipids analyzed. Whereas 'targeted' approaches are highly lipid specific and provide structural information, they lack additional information besides the selected set of lipids for detection. Isomers basically complicate the analysis of GSLs as for example glucose and galactose share the same mass and can't be separated by MS alone. Additionally, the higher gangliosides can share the same number and type of sugar building blocks, but differ in order or type of linkage, which again is not detected by MS. A common method to analyze GSL for their glycan structure is to cleave the ceramide backbone and detect the sugar head group via normal phase-liquid chromatography (LC), missing the structural information about the lipid moiety [141]. The combination of LC or TLC and MS is the most sufficient and flexible for the analysis of GSLs, whereby reversed phase (RP) analysis can be used for the separation and determination of the lipid moiety by LC with specific fragmentations for detailed identification via MS. In contrast, normal phase or hydrophilic interaction chromatography (HILIC) is realized for the separation of the glycan structures, again in combination with specific fragmentations or multiple fragmentation (MS^n) via MS. Recently, the combination of LC-MS and ion mobility offered some interesting aspects for the analysis of GSLs, which is also a technique practical for mass spectrometry imaging (MSI). There exists MSI techniques using MALDI and DESI, which allow the scanning of a tissue sections with mass spectrometry to gain an image containing the information of one mass spectra per spatially resolved area (pixel), and therefore the distribution of a distinct GSL within the tissue [142–152].

1.5.1 Electrospray ionization-Tandem Mass Spectrometry (ESI-MS^2) of Glycosphingolipids

Electrospray ionization (ESI) is a technique for liquid samples, ionizing the sample on a nebulizer needle with a strong electric field. A nitrogen flow coaxial to the liquid flow from the needle generates a focused fine aerosol of charged particles. The particles dry in the nitrogen counter stream from the instrument and ions are transported via electric field to the analyzers and detector. ESI is a soft ionization technique and often used in combination with liquid chromatography (LC) techniques such as UPLC for the analysis of non-volatile compounds in complex biological samples [153]. Tandem mass spectrometry describes in general the selection of primary ions by mass analyzers for fragmentation and the subsequent mass spectrometric analysis/selection of these product ions, either in space or in time. In a typical “triple quadrupole” instrument (QqQ, MS^2 in time) two quadrupoles working as mass analyzers are separated by a third quadrupole (or multipole/ion guide) working as a collision chamber. To this end the latter is flooded with inert gas, typically Ar, at low pressure (some 10^{-3} mbar) to trigger collision induced dissociation (CID). A QqQ can be operated in different measurement modes. *Full scan* mode detects all primary ions (precursor ions) within a defined mass range in a distinct period of time, generating an overview of (unknown) lipids/compounds in samples. *Precursor ion scan* is using the last quadrupole after the collision chamber for a fixed m/z (fragment) to search for the corresponding precursor ions with the first quadrupole scanning a mass range. In contrast, *product ion scan* selects with the first quadrupole a distinct m/z (precursor ion) and the last quadrupole scans for all generated product ions. *Neutral loss scan* detects precursor ions that all undergo a constant neutral loss. For this purpose the last quadrupole scans synchronal to the first quadrupole the same width in mass range but starting with a lower m/z corresponding to the neutral loss. The most sensitive and specific mode of detection is the use of *single ion monitoring* (SRM), where the first as well as the second quadrupole are set to a specific m/z, measuring this transition of a precursor ion to one of its product ions (reaction) over a distinct period of time. *Multiple ion monitoring* (MRM) is the use of many SRMs in line measuring in a distinct time window [153,154] (Figure 5). Tandem mass spectrometry especially in MRM mode is referred to as targeted analysis, whereas a biological sample is screened for a set of known substances. Consequently, a majority of other substances are excluded from detection and changes outside the selected set of substances remain unrecognized.

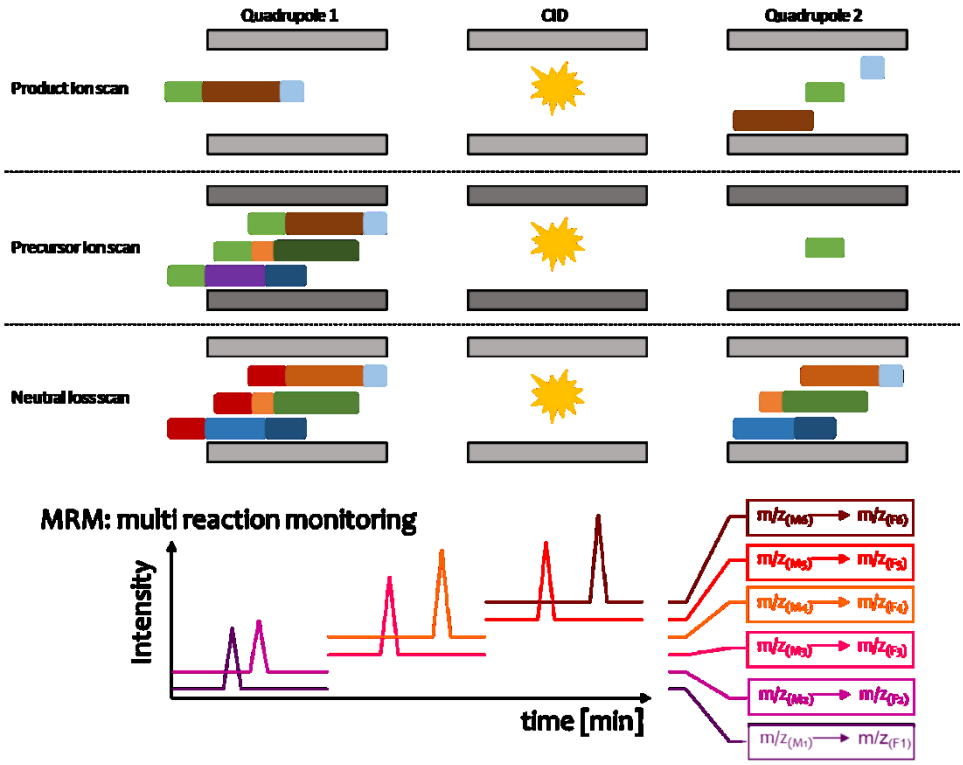

Figure 5: Scan modes in tandem mass spectrometry. A) Product ion scan is used to fragment a specific precursor ion and detect the specific fragments. B) Precursor ion scan identifies a class of lipids (precursor ions) which share a specific fragment. C) Neutral loss scan identifies a class of lipids (precursor ions) which share a specific neutral loss. D) Multi reaction monitoring is used to scan samples for defined compounds/lipids using corresponding specific transitions.

1.5.2 Imaging Mass Spectrometry of Glycosphingolipids

Tissue-based research is important for the understanding of a very broad spectrum of diseases. Where LC-MS/MS is a stable and reproducible method for lipid quantification using soluble tissue extracts, the morphology of the tissue is lost. Highly specialized tissue preparations can help that matter, e.g. by dissecting the brain in single areas such as hippocampus, cortex or cerebellum. But to separate the cerebellum in grey and white matter would extend sample preparation. Imaging mass spectrometry (MSI) emerged as a significant tool for unlabeled spatial tissue analysis.

1.5.2.1 MALDI-TOF/TOF

One of the most common techniques used for imaging mass spectrometry is matrix assisted laser/desorption ionisation (MALDI) coupled with a time-of-flight (TOF) mass spectrometer. The basic principle involves tissue sections of fresh frozen or paraffin embedded tissue that are covered by a matrix which locally extracts molecules from the tissue specimen and aids desorption/ionization for the mass analysis. The tissue is shot by a laser into an area of some few micrometers in diameter, while the matrix absorbs the energy ionizing the analytes and

transferring them into gas phase. The accelerated ions enter the TOF analyzer and are separated by their mass-to-charge (m/z) ratio, which defines the time they need to fly through the field free drift zone of the ToF analyzer. Every laser spot generates a mass spectrum and by plotting the intensity of a distinct lipid mass (m/z) for every spot in color-code, a distribution image of this lipid for the corresponding tissue area is generated. MALDI-TOF is a type of mass spectrometry assigned to untargeted analysis as every ion in the selected mass range is detected and the molecules behind the m/z are not necessarily identified. It is often used for fingerprint analysis where healthy/untreated and disease/treated tissues are compared for changes in the mass spectra combined with complex statistical analysis (reviewed in [155–158]) (Figure 6).

1.5.2.2 DESI – desorption electrospray ionization

A relatively new ionization technique for mass spectrometry imaging, not as common as MALDI, is desorption electrospray ionization (DESI). DESI is an ambient ionization method based on principles similar to electrospray ionization (ESI). A charged spray is generated by a capillary, but in contrast to ESI, this spray is used to desorb analyte ions from a surface. The charged micro-droplets of the spray build a thin liquid layer on the surface for analysis and bombardment with further charged droplets forces dissolved analytes into micron-droplets. A transfer capillary draws the micron-droplets and supports the drying process of gas-phase ions into the mass spectrometer. The tissue is screened with a defined velocity row by row, generating mass spectra in a defined time frame. Data is remodeled into images displaying the local distribution for a distinct lipid mass (m/z). By combining DESI with tandem-mass spectrometry, it should be possible to get specific, targeted information about defined lipid (ganglioside) locations within tissues. The advantage of DESI in comparison to common imaging techniques such as MALDI is the reduction of sample preparation and the relative high velocity of the measurements [159–161] (Figure 6).

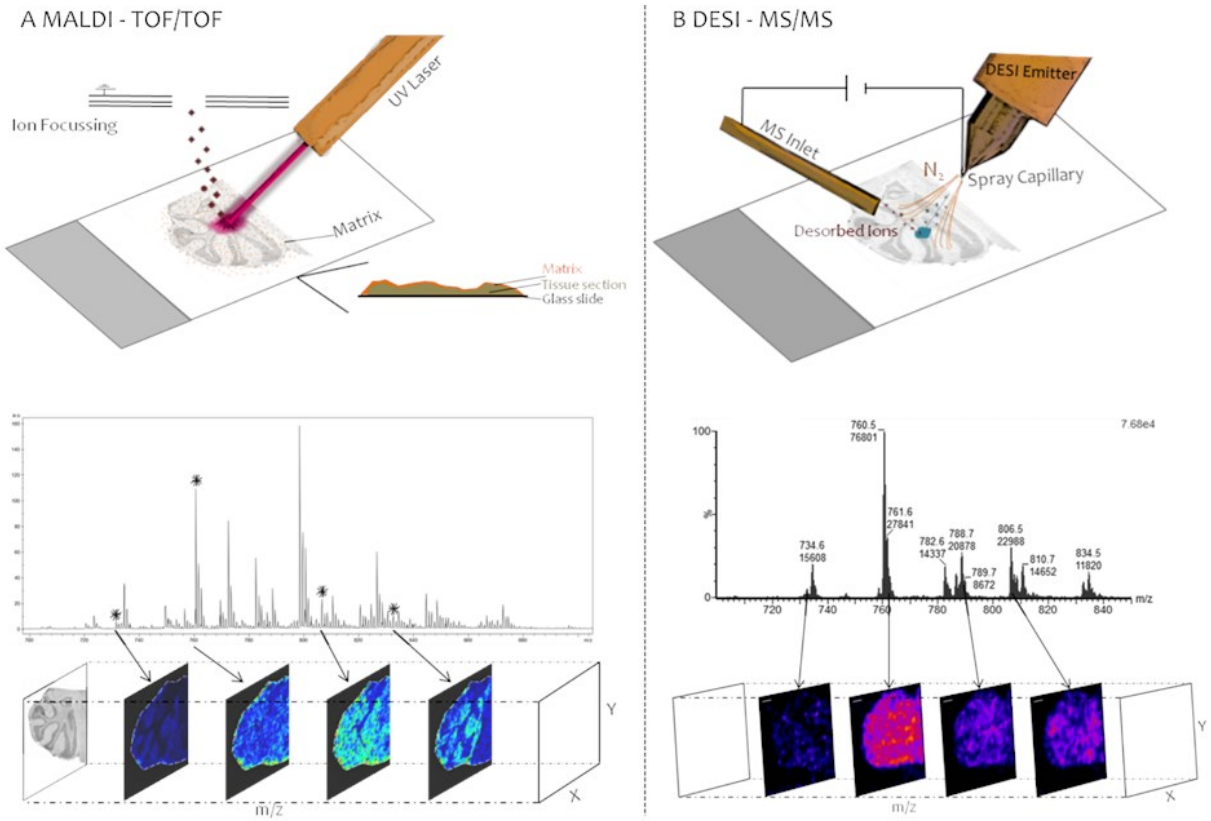

Figure 6: Mass spectrometry Imaging (MSI) techniques and their principle. A) MALDI-TOF/TOF using a laser in combination with tissue matrix to generate mass spectra for each spot. B) DESI – MS/MS screens tissue in a distinct velocity using a charged solvent spray to generate ions and dislocate them from tissue, whereby mass spectra for a defined time frame were gained. In both techniques mass spectra were remodeled to images representing the local distribution for a specific compound/lipid mass (m/z).

2 Material and Methods

2.1 Instruments

2.1.1 Sample Preparation

Table 1: Instruments for sample preparation

Instrument name	*Manufacturer*
ABT 120-4M scale (min 10 mg, d=0.1 mg)	Kern & Sohn GmbH (Balingen-Frommern, Germany)
Tissue Lyser II	Quiagen GmbH (Hilden, Germany)
DNA Speed Vac (DNA 110, Savant)	Thermo Life Sciences
Evaporator	Gebr. Liebisch GmbH & Co. KG (Bielefeld, Germany)
Vortex mixer 7-2020	neoLab Migge GmbH (Heidelberg, Germany)
Centrifuge 5415 C	Eppendorf AG (Hamburg, Germany)
Ultrasonic water bath Sonorex Super	Bandelin electronic GmbH & Co. KG (Berlin, Germany)
SpectraFluor Plus	Tecan Group AG (Männedorf, Switzerland)
20 port Vaccum Extraction Manifold (16x100 mm)	Agilent Technologies Inc. (California, USA)

2.1.2 Thin Layer Chromatography

Table 2: Instruments for TLC analysis.

Linomat IV	Camag Chemie-Erzeugnisse & Adsorptionstechnik AG & Co. GmbH (Muttenz, Switzerland)
TLC Scanner 3	

2.1.3 LC-MS/MS

LC-MS/MS analysis was performed on a Xevo TQ-S tandem mass spectrometer with an ESI source coupled to an automated Acquity I class UPLC system (Binary solvent manager and sample manager with flow-through needle) from Waters GmbH (Eschborn, Germany). Mass spectra were recorded at an ion source temperature of 90°C, cone voltage of 50 V, source offset of 50 V, desolvation temperature of 250°C and collision gas flow of 0.15 mL/min. Helium was used as inert gas, and nitrogen supply was ensured by a nitrogen generator from cmc instruments (Eschborn, Germany). MassLynx 4.1 software was used for data analysis and generation of chromatograms, and mass spectra were processed with TargetLynx as evaluation tool for the quantification of MRM data, both from Waters GmbH (Eschborn, Germany).

2.1.3.1 Columns

Table 3: LC analytical columns from Waters GmbH (Eschborn, Germany).

Particle type	*Phase material*	*Dimensions*
BEH	RP18	50 x 2.1 mm; 1.7 µm
CSH	RP18	100 x 2.1 mm; 1.7 µm
HSS	PFP	100 x 2.1 mm; 1.8 µm
BEH	HILIC	100 x 2.1 mm; 1.7 µm
BEH	Amide	100 x 1 mm; 1.7 µm
Cortecs	HILIC	100 x 2.1 mm; 1.7 µm
Cortecs	HILIC	150 x 2.1 mm; 1.7 µm

2.1.4 Imaging Mass Spectrometry

Table 4: Instruments for Imaging Mass spectrometry.

Instrument name	*Manufacturer*
Cryotom CM 3050 S	Leica Camera AG (Wetzkar, Germany)
DESI 2D source	Prosolia Inc. (Indianapolis, USA)
Omnislide (26x76; 66 well, HTC printed)	Prosolia Inc. (Indianapolis, USA)
Syringe pump	Harvard Apparatus (Massachusetts, USA)
MALDI Spotter SunCollect	SunChrom Wissenschaftliche Geräte GmbH (Friedrichsdorf, Germany)
Autoflex Speed MALDI-TOF/TOF	Bruker Corporation (Massachusetts, USA)
Rapiflex MALDI-TOF/TOF	Bruker Corporation (Massachusetts, USA)
CanoScan 9000F	Canon (Tokio, Japan)

2.2 Chemicals, Solvents and Consumables

2.2.1 Mouse Tissue samples and Bacteria strains

Mouse brain samples for the quantification of gangliosides in Tay-Sachs disease and the involvement of neuraminidases analysed with LC-M/MS and MALDI-TOF/TOF were provided by the Turkish collaboration partner Volkan Seyrantepe including the strains in Table 5.

Table 5: Mouse strains for the analysis of Tay-Sachs disease and the involvement of neuraminidases.

Bl6 wt	Neu3$^{-/-}$	Neu4$^{-/-}$
HexA$^{-/-}$	HexA$^{-/-}$ Neu3$^{-/-}$	HexA$^{-/-}$ Neu4$^{-/-}$
GM2AP$^{-/-}$	GM2AP$^{-/-}$ HexA $^{-/-}$	GM2AP$^{-/-}$ HexA $^{-/-}$ Neu4$^{-/-}$
Galgt1$^{-/-}$	Galgt1$^{-/-}$ HexA $^{-/-}$	Galgt1$^{-/-}$ HexA $^{-/-}$ Neu4$^{-/-}$
GD3S$^{-/-}$	GD3S$^{-/-}$ HexA $^{-/-}$	GD3S$^{-/-}$ HexA $^{-/-}$ Neu4$^{-/-}$
GM3S$^{-/-}$	GM3S$^{-/-}$ HexA $^{-/-}$	GM3S$^{-/-}$ HexA $^{-/-}$ Neu4$^{-/-}$

Mouse tissue analysis for the composition of hexosylceramide was performed with recently published mouse strains: *Gba2*$^{-/-}$ ([91]), *Gb3S*$^{-/-}$ ([46]), *Ugcgf/fAlbCre* ([33]), *Ugcgf/fPax8Cre*, *CSTf/fPax8Cre* and (*Ugcgf/f+CSTf/f*)*Pax8Cre* ([162]), and fatty acid 2-hydroxylase (*Fa2h*)$^{-/-}$ ([163]). Tissue samples were provided by the publication related laboratories. Additionally, WT Bl6 tissue from the strains housed by our own group were prepared. Animals were kept under specific pathogen-free conditions in barrier facilities, where a temperature of 22°C and a 12h light/ 12h dark cycle was maintained. Mice were housed in groups up to five animals and kept on a chow diet with ad libitum access to food and water. Cervical dislocation was used for euthanizing mice for tissue sampling conducted in accordance with guidelines from the European Communities Council Directive and approved by the Regierungspräsidium Karlsruhe (Germany). Caeca of mice were cut out and after 2 cm of either jejunum or colon (from the direction of caecum) tissue samples with the length of 1 cm were cut and immediately stored on dry ice (Figure 7).

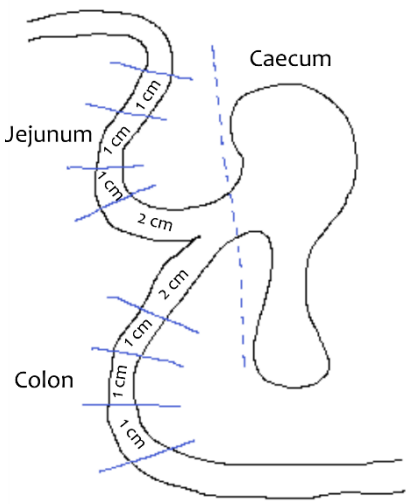

Figure 7: Tissue sampling scheme of mouse WT Bl6 jejunum, caecum and colon for the analysis of hexosylceramides.

Bacteria strains were obtained from Leibniz Institute DSMZ-German Collection of Microorganisms and Cell Cultures (Table 6). The bacteria were cultured at the University of Applied Sciences Mannheim in the laboratory of Dr. Matthias Mack. According to a previous publication [164], *Bacteroides* were grown anaerobically on Columbia agar plates with 5% sheep blood and *Bifidobacterium* on MRS medium plates containing L-cysteine-HCl (0.5 g/l) for 48 h. *Lactobacillus* was grown on MRS medium plates in an aerobic overnight culture. One culture plate was harvested and transferred in a tube containing 200 µL methanol.

Table 6: Bacteria strains used for HILIC-MS² analysis.

Genus	*Species*	*DSM No.*
Bacteroides	fragilis	2151
	vulgatus	1447
	ovatus	1896
	thetaiotaomicron	2079
	intestinalis	17393
	caccae	19024
	uniformis	6597
Prevotella	copri	18205
Bifidobacterium	longum subsp. infantis	20088
Lactobacillus	reuteri	20016

2.2.2 Solvents and LC-MS/MS additives

Table 7: Solvents and additives for Lipid analysis.

Solvent	*Grade*	*Manufacturer*
Water	LC-MS chromasolv	Honeywell Fluka (Fisher Scientific GmbH; Schwerte, Germany)
Acetone	≥99.5%	Honeywell (Fisher Scientific GmbH; Schwerte, Germany)
Acetic acid	Eluent additive for LC-MS	Honeywell Fluka (Fisher Scientific GmbH; Schwerte, Germany)
Formic acid	99-100%	VWR International (Pennsylvania, USA)
Acetonitrile	Chromasolv for HPLC ≥99.9%	Sigma-Aldich (Missouri, USA)
Propionitrile	For synthesis	Merck KGaA (Darmstadt, Germany)
Methanol	LC-MS chromasolv ≥99.9%	Honeywell (Fisher Scientific GmbH; Schwerte, Germany)
Chloroform	Chromasolv for HPLC ≥99.8%	Honeywell (Fisher Scientific GmbH; Schwerte, Germany)
2-Propanol	LC-MS chromasolv ≥99.9%	Honeywell (Fisher Scientific GmbH; Schwerte, Germany)
2-Butanol	For GC ≥99.5%	Honeywell (Fisher Scientific GmbH; Schwerte, Germany)
Ammonium formate	For mass spectrometry ≥99.0%	Sigma-Aldrich (Missouri, USA)
Ammonium acetate	chromanorm	VWR International (Pennsylvania, USA)
Citric acid monohydrate	TraceSelect ≥99.9998%	Honeywell Fluka (Fisher Scientific GmbH; Schwerte, Germany)
Potassium acetate	≥99.0%	Honeywell Fluka (Fisher Scientific GmbH; Schwerte, Germany)
Lithium acetate	99.95%	Sigma-Aldrich (Missouri, USA)

2.2.3 Sample preparation

Table 8: Sample preparation consumables.

Consumable	*Manufacturer*
Pasteur Capillary Pipettes 150 mm	Corning Inc. (New York, USA)
2 mL safe-lock PP tubes	Eppendorf AG (Hamburg, Germany)
SKRG tubes (16x100 mm; Pyrex)	Corning Inc. (New York, USA)

Stainless steel beads 5 mm	Quiagen GmbH (Hilden, Germany)
Reservoir with 1 frit 6 mL	Agilent Technologies Inc. (California, USA)
Frits 6 mL 1/2in 20 µm	Agilent Technologies Inc. (California, USA)
Reservoir 3 mL	Varian Inc (California, USA)
Frits 3 mL 3/8in 20 µm	Agilent Technologies Inc. (California, USA)
Pierce BCA protein assay kit	Thermo Fisher Scientific Inc. (Massachusetts, USA)
Preparative C18 125Å 55-105 µm	Waters GmbH (Eschborn, Germany)
DEAE Sephadex A-25	Pharmacia Biotech AB (Uppsala, Sweden)
NaOH	Riedel-de-Haen (Fisher Scientific GmbH; Schwerte, Germany)
KOH (emsure)	Merck KGaA (Darmstadt, Germany)
$CaCl_2$	Merck KGaA (Darmstadt, Germany)
KAc	Fluka (Fisher Scientific GmbH; Schwerte Germany)
KCl	Carl Roth GmbH + Co. KG (Karlsruhe, Germany)

2.2.4 TLC

Table 9: TLC consumables and syringes.

Consumable	*Manufacturer*
HPTLC silica gel 60 F_{254}	Merck KGaA (Darmstadt, Germany)
Orcinol monohydrate	Sigma-Aldrich (Missouri, USA)
Hamilton Syringe 25/50/100/250/500/1000 mL	Sigma-Aldrich (Missouri, USA)

2.2.5 LC-MS/MS and Imaging Mass spectrometry

Table 10: Consumables LC-MS/MS and MSI.

Consumable	*Manufacturer*
2 mL screw cap vial 12*32 mm (short)	Wicom GnbH (Heppenheim, Germany)
Screw cap (short) blue with pre-slit silicon/PTFE septum	Wicom GnbH (Heppenheim, Germany)
Micro insert 200 µL 5.5 mm	Wicom GnbH (Heppenheim, Germany)
Microscope slide Superfrost plus	Thermo Fisher Scientific Inc. (Massachusetts, USA)
ITO slide	Sigma-Aldrich (Missouri, USA)
Tissue-Tek O.C.T	Sakura Finetek GmbH (Staufen, Germany)
4-Phenyl-α-cyanocinnamic acid amide	Sirius Fine Chemicals GmbH (Bremen, Germany)
2,5-dihydroxybenzoic acid	Sigma-Aldrich (Missouri, USA)

2.2.6 Lipid standards

Table 11: Natural lipid standards.

Lipid	*Manufacturer*
Total ganglioside porcine brain	Avanti Polar Lipids Inc. (Alabama, USA)
Human gangliosides	Donation from the Herbert Wiegandt lab, Marburg
GM1	Fidia Farmaceutici s.p.a. (Abano Terme, Italy)
GM2 (Tay-Sachs)	Donation from the Herbert Wiegandt lab, Marburg
GM3 (bovine milk)	Avanti Polar Lipids Inc. (Alabama, USA)
GD1a	Donation from the Herbert Wiegandt lab, Marburg
GT1b	Fidia Farmaceutici s.p.a. (Abano Terme, Italy)
GD3 (bovine buttermilk)	Calbiochem (Merck KGaA; Darmstadt, Germany)
Kerasin	Avanti Polar Lipids Inc. (Alabama, USA)
Phrenosin	Avanti Polar Lipids Inc. (Alabama, USA)
LacCer	Matreya
GA1	Calbiochem (Merck KGaA; Darmstadt, Germany)
GA2 (Tay-Sachs)	Donation from the Herbert Wiegandt lab, Marburg
n-GSL mix 9 µL/band	Donation from the Herbert Wiegandt lab, Marburg
Sphingomyelin	Sigma-Aldrich (Missouri, USA)
Red marker	Sharpie (Illinois, USA)

Table 12: Synthetic Lipid standards.

Lipid	*Manufacturer*
C19-GM3	*
C14-GM2	*
C19-GM1	*
β-GalCer (d18:1;24:1) / (d18:1;16:0)	Avanti Polar Lipids Inc. (Alabama, USA)
α-GalCer (d18:1;24:1) / (d18:1;16:0)	Avanti Polar Lipids Inc. (Alabama, USA)
β-GlcCer (d18:1;24:1) / (d18:1;16:0)	Avanti Polar Lipids Inc. (Alabama, USA)
α-GlcCer (d18:1;24:1) / (d18:1;16:0)	Avanti Polar Lipids Inc. (Alabama, USA)
β-GalCer (d18:0;16:0)	Avanti Polar Lipids Inc. (Alabama, USA)
α-GalCer (d18:0;16:0)	Avanti Polar Lipids Inc. (Alabama, USA)
α/β-GalCer mix (85/15)	Avanti Polar Lipids Inc. (Alabama, USA)
α/β-GlcCer mix (85/15)	Avanti Polar Lipids Inc. (Alabama, USA)
R-/S-OH β-GalCer	Avanti Polar Lipids Inc. (Alabama, USA)

HexCer ISD mix 14, 19, 25, 31	*
Sphingomyelin ISD mix 14, 25, 31	*
LacCer ISD mix 14, 19, 25, 31	*
C19-GA1	*

* standards were self-synthesized in the Roger Sandhoff lab and self-mixed by Dr. Mariona Rabionet.

2.3 Methods

2.3.1 Sample preparation for glycosphingolipids

Tissue samples were transferred in pre-weighed 2 mL tubes and wet weight was determined before the samples were dried in the Speed Vac and again balanced to evaluate dry weight. Next, one stainless steel bead (5 mm) and 500 µL pre-cooled methanol (-20°C) were added and samples were homogenized by shaking two times 2 minutes at 25 Hz with pre-cooled (-20°C) adapters in the TissueLyser.

2.3.1.1 Lipid extraction by modified Bligh and Byer method

Lipids were extracted in 1 mL 10/10/1 (v/v/v) chloroform/methanol/water by incubation at 37°C in the ultrasonic water bath for 15 minutes and using sonication every 3 minutes for 2 minutes. Supernatant was transferred in a SKRG tube after centrifugation for 10 minutes at 2.000xg (RT). This extraction step was repeated with 1 mL 10/10/1 chloroform/methanol/water and 1 mL 30/60/8 chloroform/methanol/water. Supernatants were pooled and dried under nitrogen flow at 37°C in an evaporator. Lipid extracts were stored at 4°C for further analysis.

2.3.1.2 Protein determination

The dried pellet from lipid extraction was incubated for 4-6 hours with 1 M NaOH at 37°C in the ultrasonic water bath and sonication for up to 5 minutes was constantly turned on. Aliquots with 1:10 dilution in water were used for protein determination with Pierce BCA assay kit according to the manufacturer's protocol.

2.3.1.3 Desalination by reverse-phase (RP18) solid phase extraction

Reservoir columns were packed with C18 material and preconditioned with 3 times methanol and 2 times 0.1 M KCl. Lipid extracts were dissolved in 1 mL water and sonicated for 2 minutes before loaded onto the column. SKRG tubes were in addition washed twice with 1 mL 0.1 M KCl, sonicated and also loaded onto the column. The column with bound lipids was then washed 3 times with water and finally, lipids were eluted with 1 mL methanol into a clean SKRG tube, dried under nitrogen flow at 37°C and stored at 4°C for further analysis.

2.3.1.4 Anion exchange separation by DEAE solid phase extraction

Reservoir columns were packed with DEAE sephadex material and preconditioned with 3 times methanol and 2 times 30/60/8 chloroform/methanol/water (v/v/v). Lipid extracts were dissolved in 1 mL 30/60/8 chloroform/methanol/water (v/v/v) and sonicated for 2 minutes before loaded onto the column. SKRG tubes were washed twice with 1 mL 30/60/8 chloroform/methanol/water (v/v/v), sonicated and loaded onto the column. The column with bound lipids was then washed 2 times with methanol containing the neutral lipid fraction (fraction 1) and finally, acidic lipids (fraction 2) were eluted with 1 mL 0.5 M KAc each into a clean SKRG tube. Lipids were dried under nitrogen flow at 37°C and stored at 4°C for further analysis.

2.3.1.5 Saponification

Saponification or mild alkaline treatment was performed to remove phospholipids and reduce suppression effects during ionization. Lipid aliquots were dissolved in 1 mL 0.1 M KOH in methanol and incubated for 2 h at 37°C. Saponified lipid extracts were neutralized with 6 µL glacial AcOH and solvent was removed under nitrogen flow at 37°C. Lipid extracts were stored at 4°C for further analysis.

2.3.2 Thin layer chromatography of glycosphingolipids

2.3.2.1 TLC processing for neutral and acidic GSL

Lipid extracts were dissolved in 10/10/1 chloroform/methanol/water with a final concentration based on protein determination of 10 mg protein/mL and 20 µL (200 mg protein) were spotted to a TLC plate with Linomat IV from Camag. Total ganglioside porcine brain or human ganglioside standard with additional GM2 and GM3 were applied with a total concentration of 2.5 µg and 1 µg, respectively, for the analysis of the acidic fraction. The neutral fraction was outlined with 10 µL or 100 mg protein and n-GSL mix 9 µL/band was used as standard containing GlcCer, LacCer, Gb3 and Gb4. GA2 standard was added with a total concentration of 1 µg. Plate parameters are described in Table 13.

Table 13: TLC plate application parameter.

Start position	15 mm
Band	5 mm
Space	5 mm
Velocity	8 sec/µL

TLC plates were pre-run in 1:1 aceton/chloroform up to the top and dried under air exposure for approximately 10 minutes. Fraction 1 was processed for lipid separation in 60/35/8 chloroform/methanol/0.2% $CaCl_2$ (v/v/v) and fraction 2 in 45/45/10 chloroform/methanol/0.2% $CaCl_2$ (v/v/v) until 0.5 cm under the top in a TLC development chamber and dried under air exposure again for around 10 minutes. For both fractions orcinol reagent was used for staining glycan structures developing the plates for 10 minutes at 120°C.

2.3.2.2 Separation of diastereomeric hexosylceramides on borate-impregnated normal-phase TLC

Diastereomeric Hexosylceramide standards were separated on borate-impregnated normal phase HPTLC-plates according to previous work ([165,166]), with slight modifications. In brief, standards were applied with a Linomat IV (CAMAG) onto a HPTLC Silica gel 60 F254-plate (Merck, Darmstadt). This plate was then developed with chloroform/acetone (1/1) up to the top (no migration of HexCers, but of potential non-polar lipids). After drying the plate under vacuum (about 2.5 mbar) for 10 min, the plate was impregnated by spraying borate solution (1.5% sodium tetraborate-decahydrate) evenly all over followed by drying for 30 min under vacuum. Subsequently, the HPTLC-plate was developed with the running solvent chloroform/methanol/water/25% ammonia solution (65/25/4/0.5) and stained with orcinol reagent at 120 °C for 8-9 min detecting the glycoconjugates.

2.3.3 LC-MS/MS analysis of glycosphingolipids

Neutral glycosphingolipids were analysed as 2 mg wet weight or 0.1 mg protein/mL aliquots of lipid extracts in methanol containing synthetic internal standards for HexCer (5 pmol/mL), LacCer (5 pmol/mL) and C19-GA1 (8 pmol/mL). Quantification of lipids was performed in positive ion mode on a CSH C18 column (100x2.1 mm; 1.7 µm) using solvent A 50:50 methanol/water (v/v) versus solvent B 99:1 2-propanol/methanol (v/v) with 10 mM ammonium formate, 0.1% formic acid and 5 µm citrate. The gradient is described in Table 14 and published in von Gerichten et al., 2017. Lipids were detected in multiple reaction monitoring (MRM) mode scanning for both the protonated and water loss molecular ions ($[M+H]^+$ / $[M-H_2O+H]^+ \rightarrow [Sph(d18:1+H-2H_2O]^+$). The intensities of both transitions were added up for quantification.

Table 14: Gradient system for the analysis of neutral glycosphingolipids.

Time (min)	*Flow rate (mL/min)*	*%A*	*%B*	*Curve*
Initial	0.35	57	43	Initial
0.2	0.35	57	43	6
0.4	0.35	50	50	6
4.0	0.35	30	70	6
10.0	0.35	5	95	6
11.0	0.35	5	99	6
11.5	0.35	1	99	6
12.0	0.35	57	43	6
13.0	0.35	57	43	6

Gangliosides, were analysed as 4 mg wet weight or 0.2 mg protein/mL aliquots of lipid extracts in 90:10 2-butanol/water (v/v) containing synthetic internal standards for C19-GM3, C14-GM2 and C19-GM1 (50 pmol/mL). Quantification of lipids was performed in negative ion mode on a Cortecs HILIC column (100x2.1 mm; 1.7 µm) using solvent A 90:10 acetonitrile/water (v/v) versus solvent B 50:50 acetonitrile/water (v/v) with 10 mM ammonium acetate. The gradient is described in Table 15. Lipids were detected in multiple reaction monitoring (MRM) mode scanning for the single or double deprotonated molecular ions ($[M-H]^-$ / $[M-2H]^{2-}$ → $[NeuAc-H]^-$).

Table 15: Gradient system for the analysis of gangliosides.

Time (min)	*Flow rate (mL/min)*	*%A*	*%B*	*Curve*
Initial	0.35	100	0	Initial
1.0	0.35	100	0	6
9.0	0.35	50	50	6
11.0	0.35	10	90	6
12.0	0.35	100	0	6
25.0	0.35	100	09	6

Hexosylceramides (HexCer) were analysed as 2 mg wet weight or 0.1 mg protein/mL aliquots of lipid extracts in 40/57/3 chloroform/propionitrile/2-butanol (v/v/v) containing synthetic internal standard for HexCer (5 pmol/mL). Quantification of lipids was performed in positive ion mode on a Cortecs HILIC column (150x2.1 mm; 1.7 µm) using solvent A 97:2:1 propionitrile/2-butanol/water (v/v/v) versus solvent B 97:2:1 methanol/2-butanol/water (v/v/v)

with 0.1% formic acid in solvent A and B, and 10 mM ammonium formate in solvent B. The gradient is described in Table 16 and published in von Gerichten et al., 2017.

Table 16: Gradient system for the analysis of hexosylceramides.

Time (min)	*Flow rate (mL/min)*	*%A*	*%B*	*Curve*
Initial	0.3	100	0	Initial
0.75	0.3	100	0	6
4.5	0.3	56	44	7
5.5	0.3	0	100	6
6.5	0.3	0	100	6
8.0	0.3	100	0	6
25.0	0.3	100	0	6

Lipids were detected in multiple reaction monitoring (MRM) mode scanning for HexCers with C18 long chain base (sphingosine d18:1; dihydrosphingosine d18:0; phytosphingosine t18:0) and fatty acyl (FA) chain between 16-26 C atom lengths. The set included non-hydroxylated fatty acyl chains combined with sphingosines (NS), dihydrosphingosines (NdS) and phytosphingosines (NP) as well as α-hydroxylated (AS/AdS/AP). Structures published for the bacteria were accommodated with d17:0, d18:0 and d19:0 dihydrosphingosine base and β-hydroxylated C16 and C17 FA (BdS) [14,138]. Transitions and optimized collision energies are listed in Table 17.

Table 17: HILIC-MS^2 transitions and collision energies for hexosylceramide analysis in MRM mode.

HexCer	*Precursor ion*	*Product ion*	*Collision energy [eV]*
NS	$[M+H]^+$ $[M+H-H_2O]^+$	$[So+H-2H_2O]^+$	44
AS	$[M+H]^+$ $[M+H-H_2O]^+$	$[So+H-2H_2O]^+$	44
NP	$[M+H]^+$	$[So+H-2H_2O]^+$	36
AP	$[M+H]^+$	$[So+H-2H_2O]^+$	35
AdS	$[M+H]^+$	$[So+H-2H_2O]^+$	44
BdS	$[M+H]^+$	$[So+H-2H_2O]^+$	44

2.3.4 MALDI-TOF/TOF Mass Spectrometry Imaging

MALDI-TOF/TOF mass spectrometric Imaging (MSI) was performed at the University of Applied Sciences Mannheim in the laboratory of Dr. Carsten Hopf. The frozen brains of transgenic and control mice were mounted onto a metal chuck with frozen section compound and cut into 12 µm cryosections using a Leica cryostat, according to a literature procedure [168]. The cryosections were thaw-mounted onto precooled conductive indium tin oxide (ITO) slides. Before application of the matrix, the ITO slides were desiccated overnight under vacuum at room temperature. For the analysis of Neu3 related brain samples a 5 mg/mL solution of phenyl-cyano-cinnamamide in acetonitrile/water (90:10 v/v) was applied to the tissue sections by spray coating using the following parameters of the SunCollect device. First, three initial matrix layers were applied using flow rates of 10 µL/min, 15 µL/min, and 20 µL/min followed by six layers at 25 µL/min with a velocity of 1000 mm/min to ensure a homogeneous matrix layer on the tissue slides. MALDI imaging mass spectrometry (MALDI-MSI) was performed in negative linear mode in the m/z range of 900–2600 using an Autoflex Speed TOF/TOF with a 2000 Hz modulated Nd:YAG laser (355 nm) and the FlexImaging 4.0 software (Bruker Daltonics). Prior to analysis, the acquisition method was calibrated using the total ganglioside porcine brain extract. A total of 200 laser shots were accumulated per raster spot with a laser width of 100 µm. In addition, baseline subtraction was performed and the images were visualized after total ion current (TIC)-normalization.

For the analysis of Neu4 related brain samples a solution of 2,5-dihydrobenzoic acid (DHB) [60 mg/ml in acetonitrile/water (50:50 (v/v)), 0.5% TFA] was deposited onto the tissue sections. For matrix deposition, a SunCollect MALDI Spotter (SunChrom, Friedrichsdorf, Germany) was used at an air pressure of 2.2 bars. DHB was deposited in 5 layers, flow rate for the 1st layer set to 10 µl/min, 15 µl/min (2nd layer) and 20 µl/min for the last three layers. The distance between sprayer and tissue was 25.3 mm. A distance of 2 mm between spray lines and speed of 300 mm/min was used to ensure a homogeneous matrix layer on the tissue slides. Mass spectra were acquired on a rapifleX MALDI tissuetyper instrument (Bruker Daltonics) with a SmartbeamTM laser (modulated Nd:YAG laser, 355 nm) and 5 kHz repletion rate. Samples were analyzed in reflector negative ion mode with extraction at a source voltage of 20 kV and reflector voltage of 20.95 kV in the m/z range from 940 to 2600 Da (deflection < 900 Da) at a spatial resolution of 50 µm with 500 laser shots per position. Optimized laser energies were determined before measurement and kept constant during the measurement. The MS was calibrated internally using a list of theoretical masses of detected lipids. Spectra were

determined with flexImaging 5.0 software (Bruker Daltonics). Mass filters were chosen with a width of 0.2 Da. In addition, baseline subtraction was performed and the images were visualized after total ion current (TIC)-normalization.

2.3.4.1 Hematoxylin and eosin staining of brain section samples measured by MALDI-TOF/TOF

Tissue sections on ITO slides were put for two minutes on a 65°C heating plate after measuring with MALDI-TOF/TOF. First, the matrix had to be removed by incubating the slides in 50 mL falcons filled with 50% methanol in water, 70% methanol in water, and two times 100% methanol each for three minutes. Additionally, a five minutes incubation in 100% acetone was implemented to fix the tissue on the glass slide. Afterwards, the tissue was rehydrated rinsing the slides shortly with tap water and immersing those five minutes in distilled water. The nuclei were stained blue using Mayer's hematoxylin for two minutes followed by washing in water for three minutes and 30 seconds of 0.3% acid alcohol (350 mL EtOH + 150 mL H_2O + 1.5 mL conc. HCl). After another wash step in water for one minute the slide was immersed into blueing solution (10 g $NaHCO_3$ + 100 g $MgSO_4$ in 5L H_2O) for two minutes followed by an additional washing for two minutes in water. The red staining of eosinophilic structures was achieved by incubating the slides in Eosin for two minutes with a following was step for one minute in water. Finally, the tissue was dehydrated by three incubation steps each two minutes in 80% ethanol in water, 96% ethanol in water and 100% ethanol. The slide was dried for approximately 15 minutes at air exposure and was mounted with a glass cover using Eukitt mounting medium for microscopic evaluation.

3 Results

3.1 LC-MS/MS method development for the analysis of Gangliosides

In current literature a set of LC-ESI-MS/MS methods for the analysis of gangliosides are already published, using mostly normal phase or hydrophobic interaction liquid chromatography in combination with negative ion mode mass spectrometry for the separation of gangliosides (GG) [169–172]. Positive ion mode detection and/or the use of reversed phase (RP) liquid chromatography are less common despite higher sensitivity for positive ions and shorter re-equilibrium time, this is due to a higher complexity in possible fragmentation and adduct ions as well as weak separation of the different gangliosides [173,174]. In this work parameters for both the positive and negative ion mode in addition to the advantages and disadvantages of RP- and HILIC-MS/MS were determined in order to obtain a stable method for the quantitative analysis of gangliosides. In optimal case this should be a RP-MS/MS method in positive ion mode with baseline separation for the most abundant GGs.

3.1.1 In-source decay of gangliosides in ESI-MS/MS

A drawback of electrospray ionisation (ESI) - mass spectrometry, despite the soft ionization, is the possibility of in-source decay (ISD), the fragmentation of e.g. glycosphingolipids (GSL) in the ionization-source prior to analysis by the mass spectrometer. As intact building blocks like sialic acid or monosaccharides are lost, ISD complicates a correct identification and quantification of the analyzed lipids. The ganglioside GM1 for example can shed the terminal galactosyl and/or the *N*-acetyl-galactosaminyl moiety to mimic GM2 and/or GM3 respectively in mass spectrometric analysis (Figure 8). To evaluate the degree of ISD synthetic and natural ganglioside standards for GM3, GM2 and GM1 (10 ng/µL) were injected and analyzed with a BEH C18 column (1.7 µm, 50x2.1) and 60:40 methanol/water (v/v) versus 20:79:1 (v/v/v) isopropanol/methanol/water gradient containing 10 mM ammonium formate with and without 0.2% formic acid on the basis of previous work [85] (Table 18). In negative ion mode the precursor (M) to product ion transition of single negatively charged ganglioside (GG) to the fragment corresponding to the deprotonated and dehydrated sialic acid was used: $[M-H]^- \rightarrow [NeuAc-H_3O]^-$ (m/z 290). The ISD in negative mode was below the limit of detection (not shown). In contrast substantial and increasing ISD with more complex the ganglioside structures occurred in positive mode, in which the transition of positively charged GG to a sphingoid base fragment ($[M+H]^+ \rightarrow [So+H-2H_2O]^+$, m/z 264), was used for detection in MRM. Whereas simple GM3 was only detected as intact ion, ISD of GM2 induced detection of GM3

at the retention time of GM2 and GM1 was more than fifty percent damaged to yield the ISD ions of GM2 and GM3 respectively (Figure 8). These results revealed the importance of strict chromatographic separation for the different gangliosides to prevent false positive detection.

Table 18: RP18-MS² gradient for the analysis of gangliosides adopted from previous work to test in-source decay [85].

Time [min]	*Flow [mL/min]*	*Solvent A [%]*	*Solvent B [%]*	*Curve*
Initial	0.45	100	0	Linear
0.25	0.45	100	0	Linear
1.00	0.45	50	50	Linear
5.50	0.45	0	100	Convex
6.50	0.45	0	100	Linear
7.00	0.45	100	0	Linear
7.50	0.45	100	0	Linear

3.1.2 Ammonium adducts and ISD-water loss of ganglioside with LC-MS/MS

Using distinct solvent systems for liquid chromatography has impact on the ions detectable with mass spectrometry as described now. The addition of ammonium formate and/or formic acid to the gradient solvents can lead to ammonium $[M+NH_4]^+$ or formate $[M+HCO_2]^-$ adduct ions besides the protonated $[M+/-H]^{+/-}$ molecular ions. Another ISD that can occur is the water loss to yield $[M-H_2O+H]^+$. Synthetic and natural ganglioside standards for GM3, GM2 and GM1 (10 ng/µL) were injected and analyzed with a BEH C18 column (1.7 µm, 50x2.1) and 60:40 methanol/water versus 20:79:1 isopropanol/methanol/water gradient containing 10 mM ammonium formate with and without 0.2% formic acid to determine the degree of adduct formation and ISD-water loss in positive as well as negative ion mode (Table 18). In negative ion mode no significant adducts were detected (not shown). The positive ion mode revealed only minor ISD-water loss ions (6%) and ammonium adduct ion formation (11%) for GM3. GM2 and GM1 display the same minor water loss ions (6%/10%), in contrast the percent of ammonium adduct ions seemed to increase with increased complexity of the GGs (55% and 56%, respectively) (Figure 8).

3.1.3 Mass Spectrometry Parameter Optimization

The sensitivity for detecting ions with mass spectrometry depends on various parameters used for the electron ionization and collision induced dissociation (CID), which influence the degree of fragmentation, adduct ion formation and overall ionization capacity. Intact positive ions $[M+H]^+$ of ganglioside GM3, GM2 and GM1 were monitored while using distinct parameters of source temperature and capillary voltage for the electron spray. Ganglioside standards (10 ng/µL) with a BEH C18 column (1.7 µm, 50x2.1) and 60:40 methanol/water versus 20:97:1 isopropanol/methanol/water gradient containing 10 mM ammonium formate and 0.2% formic acid (Table 18) were injected. Three temperature points for source temperature were evaluated, namely 90°C, 120°C and 150°C. At 120°C the highest signal intensities for all measured GGs was observed (Figure 8). The capillary voltage was tested with six different high voltage value settings in the range of 2.6-3.6 kV for $[M+H]^+$, $[M-H_2O+H]^+$, and $[M+NH_4]^+$ of GM3 and GM1. For all voltages the $M+H]^+$ of both, GM3 and GM1 was the most intense ion with an optimimum at 3.0 kV (Figure 8).

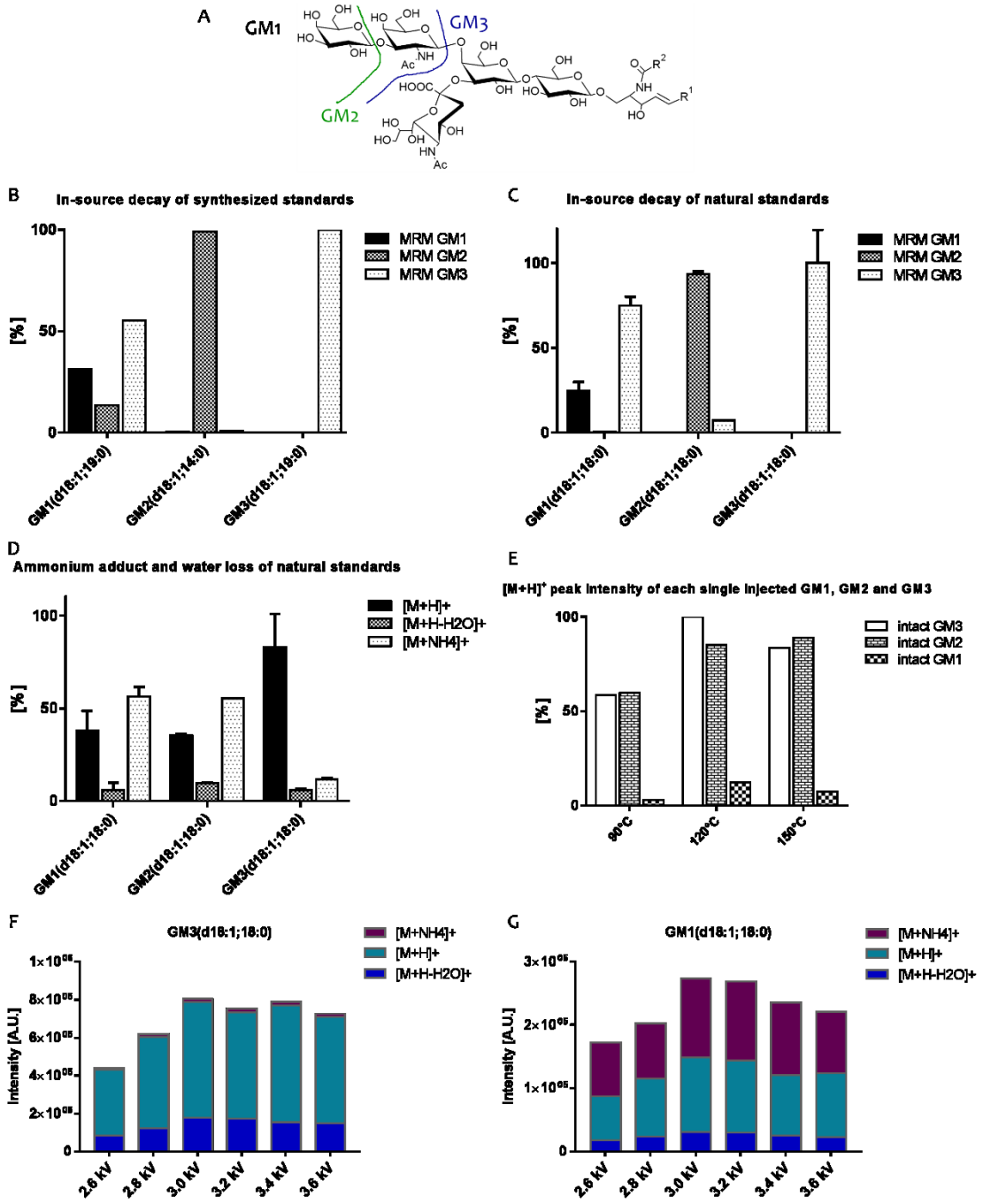

Figure 8: In-source decay (ISD) with loss of monosaccharides, ammonium adduct ion formation, ISD with water loss, and influence of source temperature and capillary voltage for the ganglioside standards GM3, GM2 and GM1. A: GM1 structure with indicated ISD for GM2 and GM1. B and C: Synthetic (N=1) and natural (N=3) standards were injected with 10 ng/µL each and measured via RP-MS/MS with MRM transitions for $[M+H]^+ \rightarrow [So+H-2H_2O]^+$ for GM1, GM2 and GM3 ISD. ISD increase with complexity of ganglioside (GG). D: Ammonium adduct formation and water loss compared to protonated ions of GM1, GM2 and GM3 natural standards (N=3). Ammonium adduct ion formation is prominent for complex GG. E: Source Temperature parameter optimization for 90°C, 120°C and 150°C revealing 120°C as improved temperature for intact $[M+H]^+$ ion of GM1, GM2 and GM3 synthesized standards. (N=1). F and G: Capillary voltage optimization of GM3 and GM1 natural standard with 3.0kV as improved value for detection. Capillary voltage displayed no influence on ammonium adduct formation and water loss. (N=3)

Optimal collision induced dissociation (CID) was tested with synthetic and natural standards for each ganglioside GM3, GM2, GM1, GD3, GD1a and GT1b (10 ng/µL) in positive and negative ion mode for different product ion fragments. Fragmentation energy via electron voltage (eV) was stepwise changed during direct injection of the standards with product ion scans for each ganglioside (predominantly (d18:1;18:0)). Optimum values were evaluated (Table 19) by gaining mass spectra for 5 minutes with a scan time of 2 seconds in the selected mass range of each ganglioside.

Table 19: Optimal CID parameters for gangliosides.

Ganglioside	*MRM*	***[eV]***	*Ganglioside*	*MRM*	***[eV]***
GM3	$[M-H]^-$ > 290.1	**50**	*GD3*	$[M-2H]^{2-}$ > 290.1	**30**
	$[M-H]^-$ > 87	**65**		$[M-2H]^{2-}$ > 581	**35**
	$[M+H]^+$ > 264.2	**50**		$[M+H]^+$ > 264.2	**38**
GM2	$[M-H]^-$ > 290.1	**60**	*GD1*	$[M-2H]^{2-}$ > 290.1	**35**
	$[M-H]^-$ > 87	**75**		$[M+2H]^{2+}$ > 264.2	**38**
	$[M+H]^+$ > 264.2	**60**		$[M+2H]^{2+}$ > 204.1	**38**
	$[M+H]^+$ > 204.1	**60**		$[M+2H]^{2+}$ > 366	**25**
GM1	$[M-H]^-$ > 290.1	**65**	*GT1*	$[M-2H]^{2-}$ > 290.1	**32**
	$[M-H]^-$ > 87	**85**		$[M+2H]^{2+}$ > 264.2	**32**
	$[M+H]^+$ > 264.2	**60**		$[M+2H]^{2+}$ > 204.1	**32**
	$[M+H]^+$ > 204.1	**60**		$[M+2H]^{2+}$ > 366	**25**
	$[M+H]^+$ > 366	**25**			

3.1.4 Adduct ion formation in the presence of diethylenetriamine

Total ganglioside porcine brain standard (16 µg/mL) was spiked with 10 mM diethylenetriamine (DETA) and ion adduct formation tested by direct injection mass spectrometry in positive ion mode. Mass spectra were generated by acquisition for 5 minutes and scan times of 2 seconds with 20 eV collision energy in the full scan mode and 65 eV in precursor ion scan mode for m/z 264/292/204. All mass spectra showed the shift of m/z 103 due to DETA adduct ion formation, exemplary visualized for GM1 and GD1 (Figure 9). Importantly, the DETA-GG adducts yielded the base peaks in precursor ion scans using the sphingoid base fragments m/z 264 or m/z 292 and the HexNAc fragment m/z 204, which demonstrates the potential of DETA addition for a more sensitive MRM detection of GGs in positive mode. However, further investigations with

DETA were stopped as a fine yellow mist had been forming in the spray chamber during acquisition to avoid further contamination of the mass spectrometer.

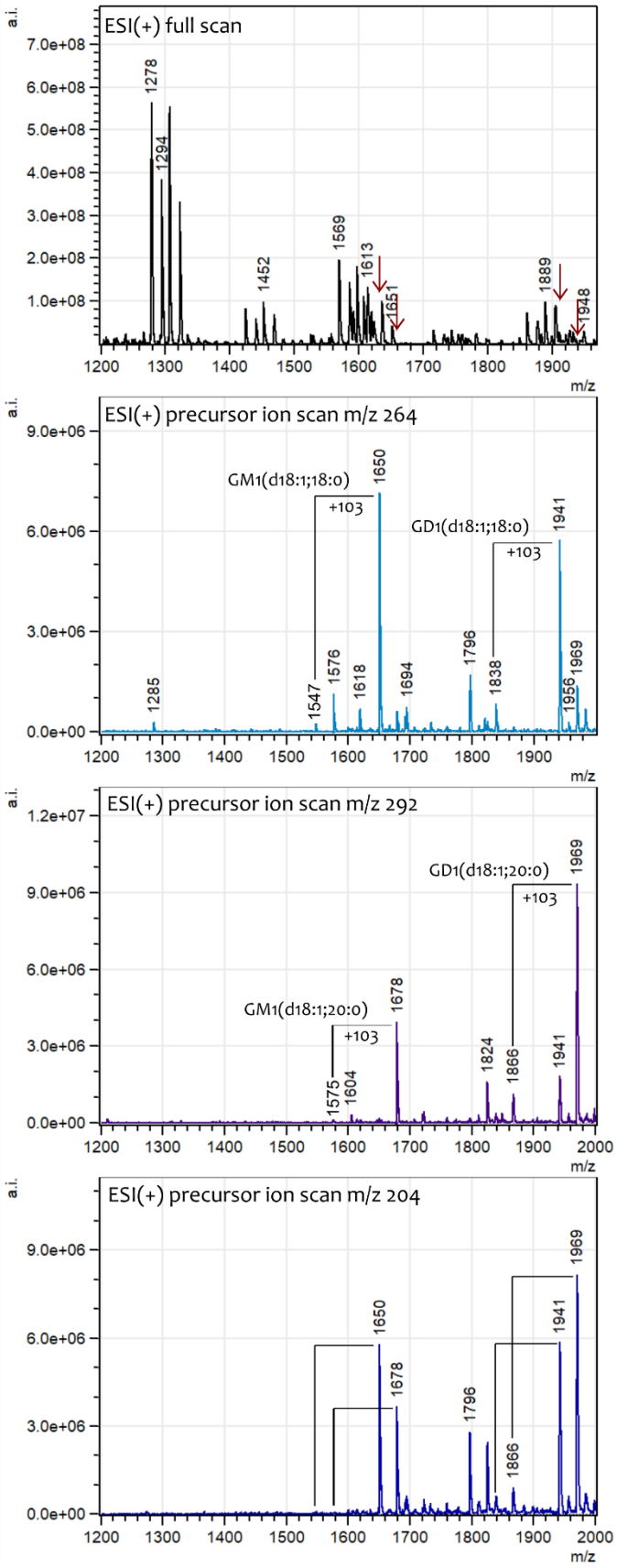

Figure 9: Adduct ion formation in the presence of 10 mM diethylenetriamine in total ganglioside porcine brain standard (16 µg/mL) measured by direct injection in the positive ion mode. From top down: full scan overview, precursor ion scan (PS) of m/z 264 for sphingosine base d18:1, PS of m/z 292 for sphingosine base d20:1, and PS of m/z 204 for the loss of HexNAc fragment.

3.1.5 Liquid Chromatography Parameter Optimization

Liquid chromatography offers many types of adsorption chemistry that can be used for separating substances. Reversed phase (RP) chromatography contains of a hydrophobic stationary phase in contrast to normal phase. Another possibility is the use of hydrophilic interaction chromatography (HILIC), which uses a hydrophilic stationary phase. With respect to gangliosides separation is mainly based on either structural differences of the hydrophobic ceramide backbone (RP) or the hydrophilic glycan moiety (HILIC) (Figure 10). The solvents used for each chromatographic type are different attending to the different chemistry, e.g. in HILIC chromatography acetonitrile is used as methanol tends to broaden the peak width. Although in positive mode methanol would be the preferred solvent for better ionization efficacy. The attempt of this work was to find either a RP based chromatography with enough resolving power to separate gangliosides in positive ion mode to benefit of higher sensitivity and/or develop a HILIC based chromatography method for analyzing gangliosides in negative and positive ion mode.

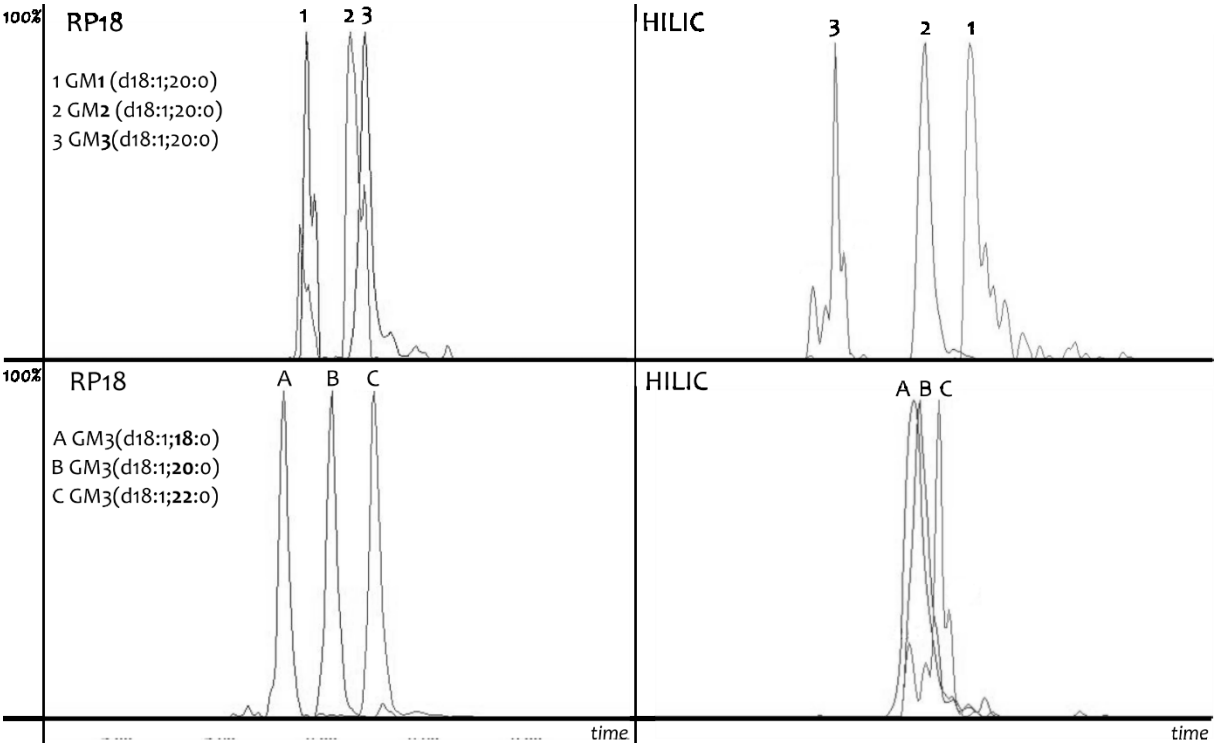

Figure 10: Separation of gangliosides on RP18 based chromatography (left) and HILIC based chromatography (right) of natural standards GM3, GM2 and GM1 10 ng/µL detected with LC-MS/MS in negative ion mode. Separation power of RP18 versus HILIC for glycan head group (top) and ceramide moiety (bottom) of gangliosides.

3.1.5.1 Gradients for reversed phase chromatography

Routine analysis of neutral sphingolipids with LC-MS/MS was based on reversed phase (RP) chromatography in our lab. Starting from the established gradient with a 60:40 methanol/H_2O (v/v) versus 20:97:1 isopropanol/methanol solvent system (v/v/v) containing 10 mM ammonium formate and 0.2% formic acid in combination with a BEH C18 column (1.7 µm; 50x2.1) (Table 18), the gradient was systematically tested for different solvent compositions and gradient course to gain a baseline separation of gangliosides (chromatographic resolution R ≥ 1.5). Additionally, a CSH C18 column (1.7 µm; 100x2.1) with a smaller pore size of 130 A° compared to 150 A° of BEH C18 and a higher efficacy due to longer column length was tested. As an alternative to classical C18 columns the HSS PFP column (1.8 µm; 100x2.1) was examined, which has a pentafluorophenyl phase with optimized performance at low pH values and an even smaller pore size of 100 A° compared to the above mentioned columns. The different solvent systems tested on the BEH C18 column are mentioned in Appendix I, the result with the highest chromatographic resolution (gradient #5 R=1) is shown in Table 20. Nevertheless, all seven tested gradients failed to gain a baseline separation for gangliosides with R≥1.5 (Figure 11).

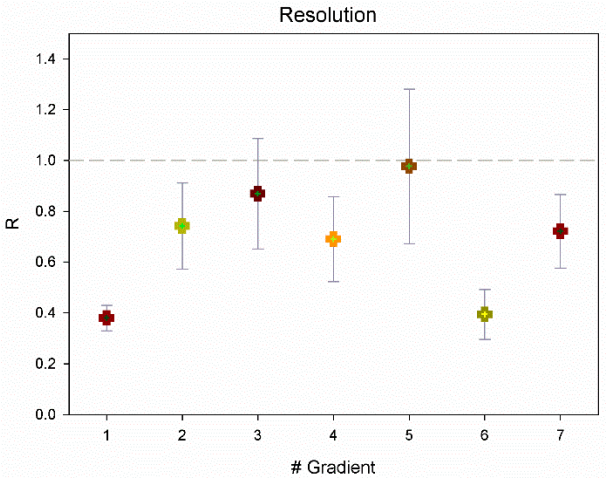

Figure 11: Calculated chromatographic resolution of GGs GM1/GM3 for different solvent systems and gradients used for BEH C18 column (1.7 µm; 50x2.1). Gradient #5 showed the highest resolution with R=1, but failed to separate gangliosides with baseline separation (R≥1.5).

Natural standard mixture of gangliosides GM3, GM2 and GM1 (10 ng/µL) were injected and measured in positive ion mode to gain chromatograms of each ganglioside with the ceramide backbone d18:1;20:0, where retention time (t_R) and peak width at half peak heights (FWHM) were extracted to calculate chromatographic resolution $R = 1.18 * (\frac{(tR2-tR1)}{(FWHM2+FWHM1)})$. The same natural standards mixture as mentioned above was used for the CSH C18 column with a similar

solvent system shown in Table 21 and for the HSS PFP column with a solvent system modified from Basit *et al.*, *2015* [175] shown in Table 22. The results of chromatographic resolution for each column and gradient are outlined in Table 23 revealing that the tested RP columns fail to resolve all three gangliosides with baseline separation. The CSH C18 and HSS PFP columns are sufficient to differ between GM3 and GM1 as well as GM3 and GM2. That, diminished the false-positive detection for GM1 in-source decay, but both fail to separate GM1 from GM2 completely. The overlay of extracted ion chromatograms for natural ganglioside standards in a mixture of LacCer, GA2, GA1, GM1, GM2, GM3 and GD1a (10 ng/µL) run on the HSS PFP column revealed that LacCer, GA2 and GA1 are only separated by about 50% of the peak heights similar to GM2 and GM1. GD1a detection resulted in a small double peak with a high peak width, which was not base line separated from GM1 (Figure 12).

Table 20: LC gradient used for BEH C18 column (1.7 µm; 50x2.1) ; A: 60% acetonitrile/40% H_2O, B: 99% isopropanol/1% methanol, 10 mM ammonium formate, 0.1% formic acid.

Time (min)	*Flow rate (mL/min)*	*%A*	*%B*	*Curve*
Initial	0.45	50	50	Initial
0.1	0.45	50	50	8
5.5	0.45	15	85	8
7.0	0.45	10	90	6
7.25	0.45	50	50	6
8.0	0.45	50	50	6

Table 21: LC gradient used for CSH C18 column (1.7 µm; 100x2.1) ; A: 50% methanol/50% H_2O, B: 99% isopropanol/1% methanol, 10 mM ammonium formate, 0.1% formic acid.

Time (min)	*Flow rate (mL/min)*	*%A*	*%B*	*Curve*
Initial	0.35	50	50	Initial
0.2	0.35	50	50	6
7.0	0.35	10	90	6
7.5	0.35	10	90	6
8.0	0.35	50	50	6
9.0	0.35	50	50	6

Table 22: LC gradient used for HSS PFP column (1.8 µm; 100x2.1) ; A: 40% acetonitril/60% H_2O, B: 20% acetonitril/80% isopropanol, 0.1% formic acid

Time (min)	*Flow rate (mL/min)*	*%A*	*%B*	*Curve*
Initial	0.45	100	0	Initial
0.5	0.45	100	0	7
2.5	0.45	60	40	7
4.5	0.45	40	60	7
6.5	0.45	21	79	6
7.5	0.45	0	100	6
8.0	0.45	100	0	6
10.0	0.45	100	0	6

Table 23: Chromatographic resolution of different reversed phase columns.

LC column	*R (GM3/GM1)*	*R (GM3/GM2)*	*R (GM2/GM1)*
BEH C18	1.16	0.54	0.51
CSH C18	1.54	1.26	0.44
HSS PFP	3.95	5.77	0.57

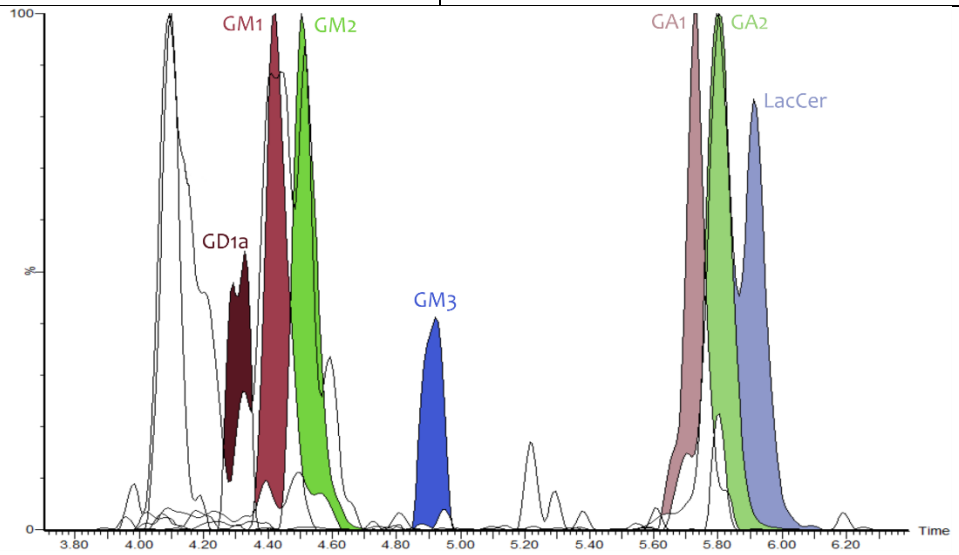

Figure 12: Overlay of extracted ion chromatograms generated by HSS PFP column for GSL standard mix.

3.1.5.2 Gradients for normal phase and hydrophobic interaction chromatography

As the detection of gangliosides with a RP18 based chromatography is still limited despite the optimization attempt in chapter 3.1.5.1 the gangliosides were tested to separate by HILIC based chromatography. For the development of a HILIC phase based LC-MS/MS analysis a BEH HILIC column (1.7 µm; 100x2.1) was tested with a solvent system consistent of 90:10 acetonitrile/H_2O (v/v) versus 50:50 acetonitrile/H_2O (v/v) with 10 mM ammonium formate. Natural standards mixture of GM3, GM2 and GM1 (10 ng/µL) were injected and measured in positive as well as negative ion mode. To achieve a better ionization efficacy as well as better solubility of the gangliosides the methanol tolerance in the solvent system was tested. Gangliosides were measured with transitions for $M+H]^+/[M+H-H_2O]^+/[M+NH_4]^+ \rightarrow [Sph-2H_2O]^+$ in positive ion mode and $[M-H]^- \rightarrow [NeuAc-H]^-$ in negative ion mode. Ionization efficacy in positive mode was higher than in negative mode, to test if the ionization could be enhanced in negative ion mode a solvent system with A 45:45:10 (v/v/v) acetonitrile/methanol/water was used. The addition of methanol leads to a drastic peak widening on the BEH HILIC column together with the appearance of ghost peaks. Furthermore, a BEH amide column (1.7 mm; 100x2.1) and a CORTECS HILIC column (1.7 µm; 100x2.1) were evaluated for their chromatographic performance with the same acetonitrile based gradient (Figure 13). The Cortecs HILIC column showed the most similar adsorption power for all three gangliosides as well as the smallest peak width, additionally the number of theoretical plates could be enhanced about a factor of three (BEH N=1700, Cortecs N=5800).

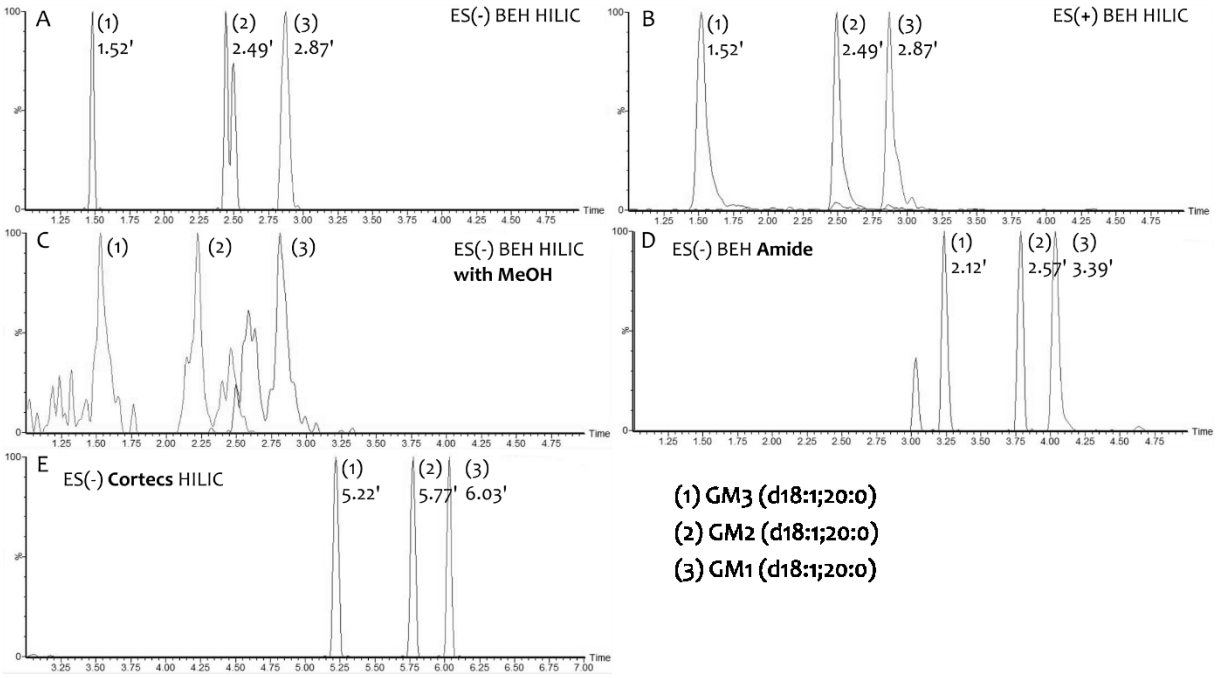

Figure 13: HILIC-MS² method development testing positive (A) and negative (B) ion mode with a BEH HILIC column as well as methanol (C) tolerance for a standard mixture of GG GM1, GM2 and GM3. Additionally, a BEH Amide (D) and Cortecs HILIC (E) column were tested with the same acetonitrile solvent system in negative ion mode.

3.1.5.3 Additives for negative ion mode detection

To accomplish better sensitivity for gangliosides in the negative ion mode different salt additives were tested. Their ionization efficacy was measured by direct injection of a human ganglioside standard (5 µg/mL; 10 minutes acquisition). The most abundant ganglioside in this standard is GD1a, which was detected as double negatively charged ion with the ceramide backbone composition of d36:1 (m/z 917.4) and d38:1 (m/z 931.8). Ion signals of these species were used as a quality parameter for signal intensity, as well as their calculated adduct ions. The human ganglioside standard was dissolved in methanol with no additive, 0.1% lithium acetate, 0.1% potassium acetate, 10 mM ammonium acetate and 10 mM ammonium formate. Mass spectra were generated by precursor ion scanning with the product ion for sialic acid loss of gangliosides (m/z 290). Methanol without any additives showed a weak signal for GD1a slightly above background noise, while the addition of either 0.1% lithium acetate or potassium acetate decreased the GD1a signal into background noise. Ammonium formate (10 mM) doesn't seem to change the GD1a signal intensity overall, although ions at 42 mass units higher than the corresponding GD1a peaks appeared. The most promising result was achieved with an additive containing 10 mM ammonium acetate showing the highest signal intensity for GD1a together with detectable signals for GM1 (m/z 1544/1573) and doubly charged GT1b (m/z 1062/1074) (Figure 14).

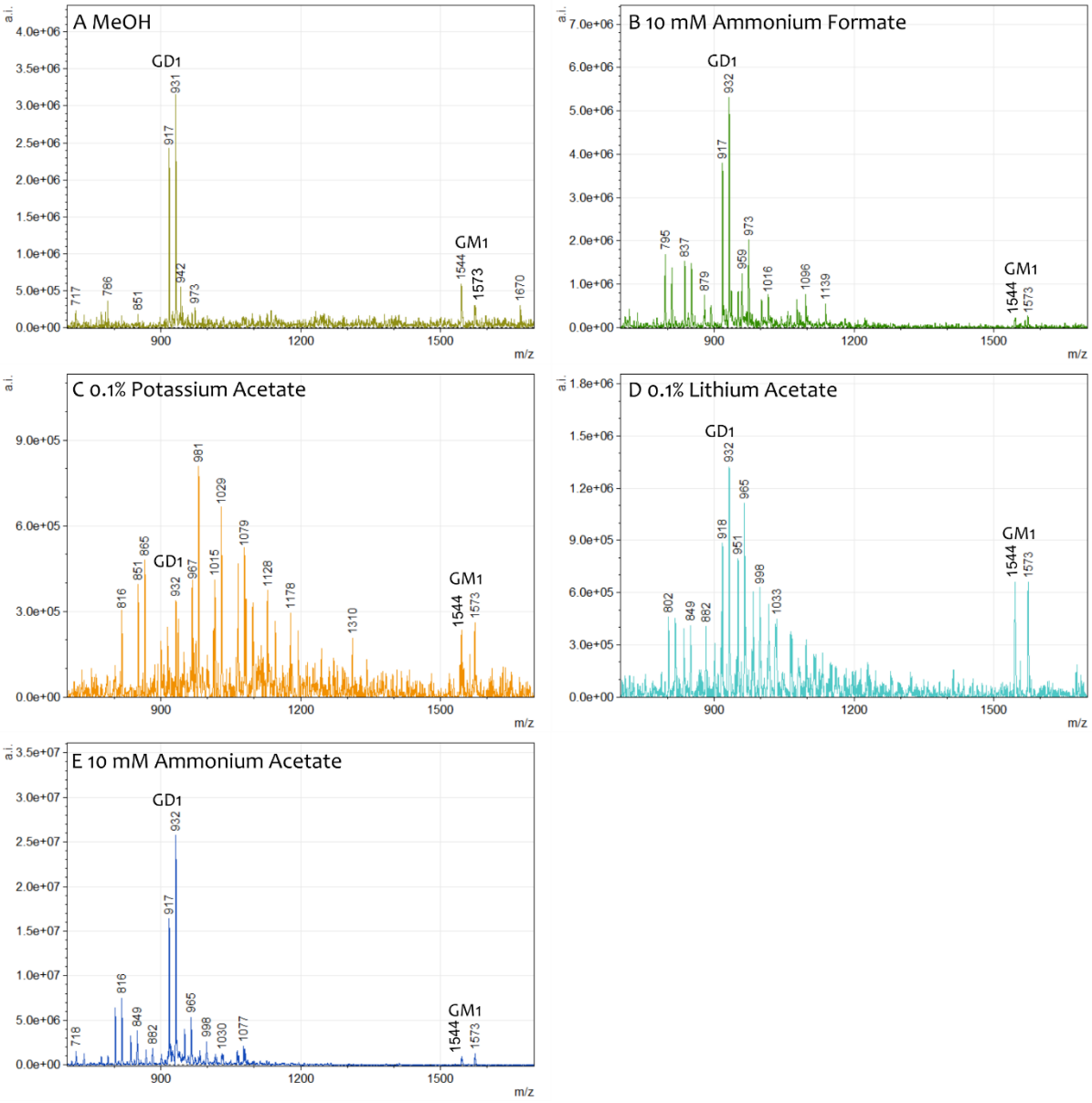

Figure 14: Additives test for ganglioside detection in negative ion mode. Human ganglioside standard (5 µg/mL) was measured with direct injection and precursor ion scan spectra were acquired within 10 minutes. Standard was solved in 100% MeOH (A) with 10 mM ammonium formate (B), 0.1% potassium (C) or lithium (D) acetate, and 10 mM ammonim acetate (E). GD1 (m/z 917 and 932) and GM1 (m/z 1544 and 1573) are the most abundant gangliosides in all spectra. Note that arbitrary intensity of the ammonium acetate spectrum (E) is approximately 10times higher than spectra with other additives.

3.1.6 Sample preparation

Sample preparation for gangliosides is complex and time consuming. To test the influence of different sample preparation steps, a WT Bl6 mouse brain was homogenized, then divided into five equal aliquots and further processed with five different methods of preparation. Gangliosides were detected with LC-MS/MS in negative ion mode with the transition $[M-H/2H]^{-/2-} \rightarrow [NeuAc-H_3O]^-$ using a 90:10 acetonitrile/H2O (v/v) versus 50:50 acetonitrile/H2O (v/v) gradient with 10 mM ammonium formate. The most sufficient protocol with a 5fold

increase in sensitivity compared to only desalination for the gangliosides GM3, GM2, GM1 and GD3 was to first separate the lipid extract with anion exchange chromatography in neutral and acidic fractions, next delete phospholipids via saponification and finally desalinate fractions with RP18 chromatography (Figure 15).

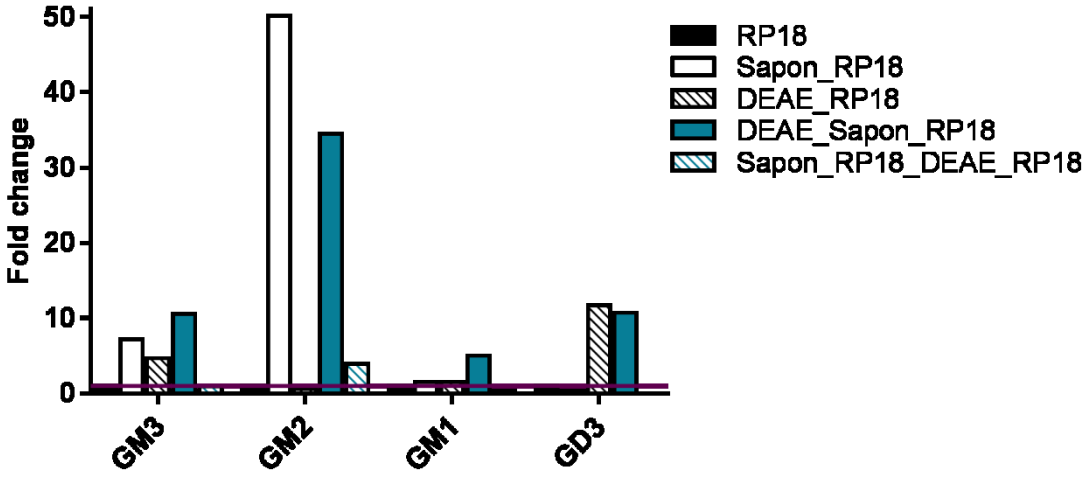

Figure 15: Sample preparation test for the analysis of gangliosides with HILIC-MS² analysis. Whole WT mouse brain was homogenized and separated into five equal aliquots. Desalination (RP18), saponification to eliminate phospholipids (Sapon), and anion exchange chromatography to use only acidic GSL (DEAE) was performed in different combinations. First anion exchange chromatography, followed by saponification and desalination (blue) revealed highest sensitivity for ganglioside detection.

3.2 Ganglioside processing by Neuraminidases in models of Tay-Sachs disease (GM2 gangliosidoses)

3.2.1 Neuraminidase 4

Tay-Sachs disease is a lysosomal storage disorder where ganglioside GM2 accumulates in the brain, which leads to severe neurodegeneration and death after 2-4 years in the infantile form. Complete genetic disruption of the Hexosaminidase A activity, which rather resembles the severe infantile forms of TSD, results in mice only in a mild GM2 accumulation and therefore mild neurologic phenotype. Neuraminidases in the mouse brain were found to bypass the defective GM2 degradation to GM3 by cleaving the terminal sialic acid and converting GM2 into GA2, which can then further be degraded by the remaining HexB to LacCer which is the normal degradation product from GM3. The cooperation partner of this work, Volkan Seyrantepe, reported neuraminidase 4 as a candidate involved in the GM2 bypass process and consequently a target for possible treatment [102]. In the consecutive chapter the impact of neuraminidase 4 on brain gangliosides was analyzed by HILIC-MS/MS in mouse models of

Tay-Sachs disease. This was combined with depletions of selected enzymes partaking in the ganglioside biosynthesis, to gain an overview of potential effects for neuraminidase 4 treatment. Lipid brain extracts were proceeded with anion exchange chromatography, saponification and desalination. Additionally, wet weights and protein content were determined (Table 24).

Table 24: Mouse brain samples for the LC-MS/MS analysis of gangliosides in Tay-Sachs disease with combined neuraminidase 4 deficiency and ganglioside synthesis enzymes depletion.

Name	*Age (month)*	*Colony*	*Genotype*	*acidic GSL MS*	*neutral GSL MS*	*HexCer MS*	*MALDI*	*wet weight [mg]*	*protein [mg]*
70	3	GD3S	WT	●	●		●	190.4	15.0
34	6	GD3S	WT	●	●	●		223.3	16.0
H7	3	GD3S	HexA	●	●			192.3	14.5
H17	6	GD3S	HexA	●	●			211.1	14.0
N12	3	GD3S	Neu4	●	●			213.0	13.9
N9	6	GD3S	Neu4	●	●	●		205.1	15.0
46	3	GD3S	GD3S	●	●			209.3	16.4
31	6	GD3S	GD3S	●	●			195.9	15.4
75	3	GD3S	Neu4GD3S	●	●			192.2	16.2
73	6	GD3S	Neu4GD3S	●	●			199.6	14.2
66	3	GD3S	HexAGD3S	●	●			237.1	17.8
44	6	GD3S	HexAGD3S	●	●			203.2	14.7
74	*3*	GD3S	Neu4HexAGD3S	●	●			215.3	15.9
64	12	GD3S	Neu4HexAGD3S	●	●			201.6	17.2
83	6	GD3S	Neu4HexAGD3S	●	●		●	129.0	10.3
84	6	GD3S	HexA	●	●	●	●	232.9	17.2
85	6	GD3S	Neu4GD3S	●	●		●	232.7	19.3
86	3	GD3S	Neu4GD3S	●	●			204.5	14.0
90	6	GD3S	HexAGD3S	●	●		●	267.9	20.1
27	3	GD3S	GD3S	●	●			186.5	
28	6	GD3S	GD3S	●	●			192.9	
32	6	GD3S	GD3S	●	●			224.5	
36	3	GD3S	GD3S	●	●			178.3	
87	3	GD3S	Neu4GD3S	●	●			197.0	
88	3	GD3S	Neu4GD3S	●	●			196.2	
109	6	GD3S	Neu4GD3S	●	●			392.2	

110	6	GD3S	Neu4GD3S	●	●			397.3	
707	3	GM2AP	GM2AP	●	●			220.6	
705	6	GM2AP	GM2AP	●	●	●		195.1	
704	6	GM2AP	HexAGM2AP	●	●			213.9	
703	6	GM2AP	Neu4HexAGM2AP	●	●			240.8	
708	3	GM2AP	HexAGM2AP	●	●		●	181.5	10.3
709	3	GM2AP	Neu4HexA	●	●		●	134.8	10.9
713	3	GM2AP	Neu4GM2AP	●	●	●	●	119.4	8.9
714	3	GM2AP	Neu4HexAGM2AP	●	●		●	130.9	7.5
717	6	GM2AP	Neu4HexA	●	●	●	●	174.6	10.7
724	6	GM2AP	Neu4HexA	●	●			182.7	13.2
722	3	GM2AP	GM2AP	●	●			181.5	
723	3	GM2AP	GM2AP	●	●			177.9	
732	3	GM2AP	Neu4GM2AP	●	●			156.6	
733	3	GM2AP	Neu4GM2AP	●	●			224.5	
745	6	GM2AP	Neu4GM2AP	●	●	●		180.8	
746	6	GM2AP	GM2AP	●	●	●		164.0	
747	6	GM2AP	GM2AP	●	●	●		153.4	
751	6	GM2AP	Neu4GM2AP	●	●	●		198.8	
21	3	GM3S	wt	●	●			196.1	13.7
34	3	GM3S	HexAGM3S	●	●			203.9	15.0
11	6	GM3S	wt	●	●		●	210.8	17.8
33	3	GM3S	HexA	●	●		●	202.1	11.5
42	3	GM3S	Neu4GM3S	●	●			198.9	14.4
43	3	GM3S	Neu4	●	●		●	188.7	10.4
44	3	GM3S	GM3S	●	●			207.5	12.7
46	3	GM3S	HexAGM3S	●	●			235.9	14.1
54	3	GM3S	Neu4HexAGM3S	●	●			184.5	12.3
24	3	GM3S	GM3S	●	●			189.0	
25	3	GM3S	GM3S	●	●			184.3	
36	6	GM3S	GM3S	●	●			191.2	
31	3	Galgt	Galgt1	●	●			164.8	13.1
36	6	Galgt	Galgt1	●	●			209.2	14.3
41	6	Galgt	HexAGalgt1	●	●			162.2	11.2
35	3	Galgt	Neu4Galgt1	●	●			192.6	14.9
47	6	Galgt	Neu4Galgt1	●	●			205.6	14.5
39	3	Galgt	Neu4HexA	●	●			161.9	12.5

40	6	Galgt	Neu4HexA	●	●			183.4	13.6
37	3	Galgt	Neu4HexAGalgt1	●	●			206.1	16.5
23	6	Galgt	Neu4HexAGalgt1	●	●			190.6	13.8
VS67	3	Galgt	Neu4HexAGalgt1	●	●			162.1	14.1
VS68	3	Galgt	Neu4Galgt1	●	●			190.2	14.3
VS69	6	Galgt	Neu4Galgt1	●	●			206.3	14.1
VS70	6	Galgt	Neu4HexAGalgt1	●	●			198.1	12.4
VS71	6	Galgt	Neu4HexA	●	●			220.4	14.1
19	3	Galgt	Neu4Galgt1	●	●			197.4	
20	3	Galgt	Neu4HexA	●	●			221.9	
24	3	Galgt	Neu4HexA	●	●			173.1	
25	3	Galgt	Neu4HexA	●	●			120.8	
49	6	Galgt	Neu4HexA	●	●		●	215.8	
61	6	Galgt	Neu4Galgt1	●	●			216.7	
62	6	Galgt	Neu4HexA	●	●		●	212.8	
54	3	Neu4	wt	●	●			186.3	
83	3	Neu4	wt	●	●			209.8	
C6	6	Neu4	wt	●	●		●	403.4	
C7	6	Neu4	wt	●	●		●	405.1	
N11	3	Neu4	Neu4	●	●			238.7	
N13	3	Neu4	Neu4	●	●			219.6	
N29	6	Neu4	Neu4	●	●		●	220.5	
N30	6	Neu4	Neu4	●	●		●	204.3	
H11	6	Neu4	HexA	●	●		●	224.0	
H15	6	Neu4	HexA	●	●		●	210.0	
H25	3	Neu4	HexA	●	●			394.3	
H26	3	Neu4	HexA	●	●			374.6	

Preliminary TLC analysis of mouse brain tissue with HexA$^{-/-}$, Neu4$^{-/-}$, GM2AP$^{-/-}$ and Neu4$^{-/-}$ HexA$^{-/-}$ showed a deletion of Neu4 reduced GM1 levels compared to WT or HexA$^{-/-}$. Accumulation of GM2 in the range of HexA$^{-/-}$ or more pronounced GM2AP$^{-/-}$ was not detected in mice with Neu4 deficiency (Figure 16). Nevertheless, the additional deletion of Neu4 to HexA$^{-/-}$ led to a more intense GM2 accumulation as in only HexA deletion mouse brains.

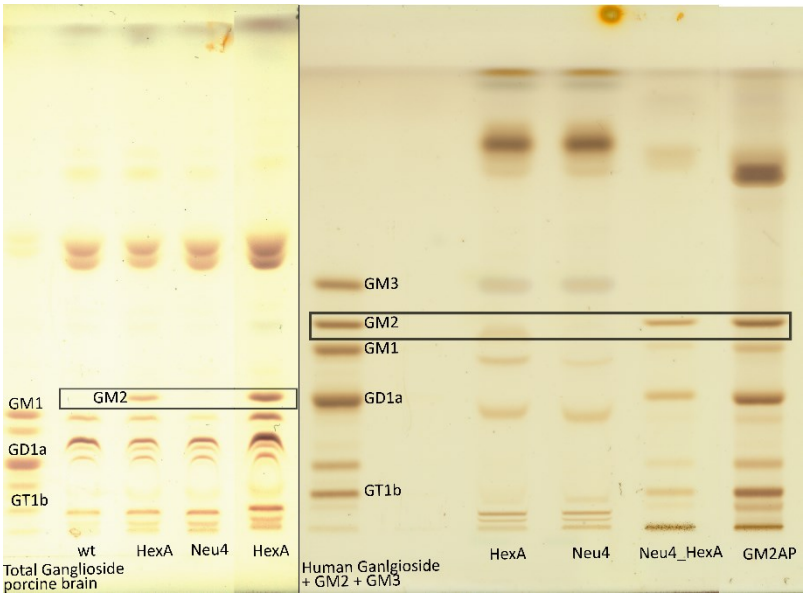

Figure 16: TLC of GM2 gangliosidosis mouse brain tissue and neuraminidase 4 deficiency mouse brain tissue from the age of 6 month. WT and Neu4$^{-/-}$ showed no GM2 band, whereby HexA$^{-/-}$, GM2AP$^{-/-}$ and Neu4$^{-/-}$/HexA$^{-/-}$ displayed a clear GM2 accumulation.

3.2.1.1 Neuraminidase 4 in GM2 gangliosidosis mouse model

Gangliosides from brain lipid extracts were measured in negative ion mode as $[M\text{-}H]^- \rightarrow [NeuAc\text{-}H]^-$ transitions on a Cortecs HILIC column with an 90:10 acetonitrile/water (v/v) versus 50:50 acetonitrile/water (v/v) gradient containing 10 mM ammonium acetate. Neutral glycosphingolipids that were metabolic products from the gangliosides of interest were measured in positive ion mode as $[M+H]^+ \rightarrow [So+H\text{-}2H_2O]^+$ transitions on a CSH C18 column with a gradient of 50:50 methanol/water (v/v) versus 99:1 isopropanol/methanol (v/v) containing 10 mM ammonium formate, 0.1% formic acid and 5 µM citrate. Mouse brain samples from mice of 3 and 6 month age with a genetic background of Bl6 WT, Neu4$^{-/-}$, HexA$^{-/-}$, GM2AP$^{-/-}$, Neu4$^{-/-}$/ HexA$^{-/-}$ and Neu4$^{-/-}$/ GM2AP$^{-/-}$ were analysed in triplicates (n = 3) and ganglioside values were displayed as ratio of single ganglioside per direct metabolite, e.g. GD1a/GM1 ratio. Furthermore, the impact of Neu4 on ganglioside metabolism was highlighted by presenting the data as fold change ratio of Neu4$^{-/-}$/WT or double-knockout containing Neu4 per single knockout (e.g. (Neu4$^{-/-}$/ HexA$^{-/-}$)/ HexA$^{-/-}$), respectively. Figure 17 shows the fold

change values against the p value for ganglioside data of the different mouse models, whereby both age time points are included in the figure. The results reveal that Neu4 deletion led to increased ratios of GM3/LacCer (orange rhomb) and GD3/GM3 (grey dot), whereas GM1/GA1 (grey triangle) and GD1a/GM1 (red cross) ratios decreased (Figure 17, red encircled region).

3.2.1.2 Neuraminidase 4 in a GM3/GD3 only mouse model

Gangliosides were analyzed as described above (3.2.1.1.1) and presented as fold change values. The influence of Neu4 on GM3 and GD3 was determined by using mice deficient in *N*-acetyl-galactosaminyl transferase (Galgt1$^{-/-}$) with an age of either 3 or 6 month. Mice with a combined knockout in Neu4$^{-/-}$ and Galgt1$^{-/-}$ were compared to only Galgt1$^{-/-}$ deficient mice in a Bl6 WT background as well as in a Tay-Sachs disease model (HexA$^{-/-}$) (Figure 17). The influence of Neu4 on GD3 levels were not detectable due to low sensitivity of GD3 (not shown). Although, the increase of GM3/LacCer levels in mice deficient of Neu4 as shown in the previous chapter could be confirmed (Figure 17).

3.2.1.3 Neuraminidase 4 in a 0-series gangliosides only mouse model

Gangliosides were analyzed as described above (3.2.1.1.1) and presented in fold change values. The influence of Neu4 on 0-series gangliosides was resolved by using mice deficient in GM3 synthase (GM3S$^{-/-}$) with an age of 3 month. Mice with a combined knockout in Neu4$^{-/-}$ and GM3S$^{-/-}$ were compared to only GM3S$^{-/-}$ deficient mice in a Bl6 WT background as well as in a Tay-Sachs disease model (HexA$^{-/-}$) (Figure 17). The results show that Neu4 may have an influence on GD1c or GD1α per GM1b ratios.

3.2.1.4 Neuraminidase 4 impact on gangliosides in a GD3 synthase deficient mouse model

Gangliosides were analysed as described above (3.2.1.1.1) and presented in fold change values. The influence of Neu4 on mainly a-series gangliosides was determined by using mice deficient in GD3 synthase (GD3S$^{-/-}$) with an age of 6 month. Mice with a combined knockout in Neu4$^{-/-}$ and GD3S$^{-/-}$ were compared to only GD3S$^{-/-}$ deficient mice in a Bl6 WT background (Figure 17). As described above the increase in GM3/LacCer levels upon deletion of Neu4 was detected, as well as the decrease of GM1/GA1 levels similar to the results of the GM2 gangliosidosis model combined with Neu4 deficiency (Figure 17). The results show that the main activity of neuraminidase 4 is on GM1/GA1 and GM3/LacCer levels with minor activity extended to GM2/GA2 and GD1/GM1 levels.

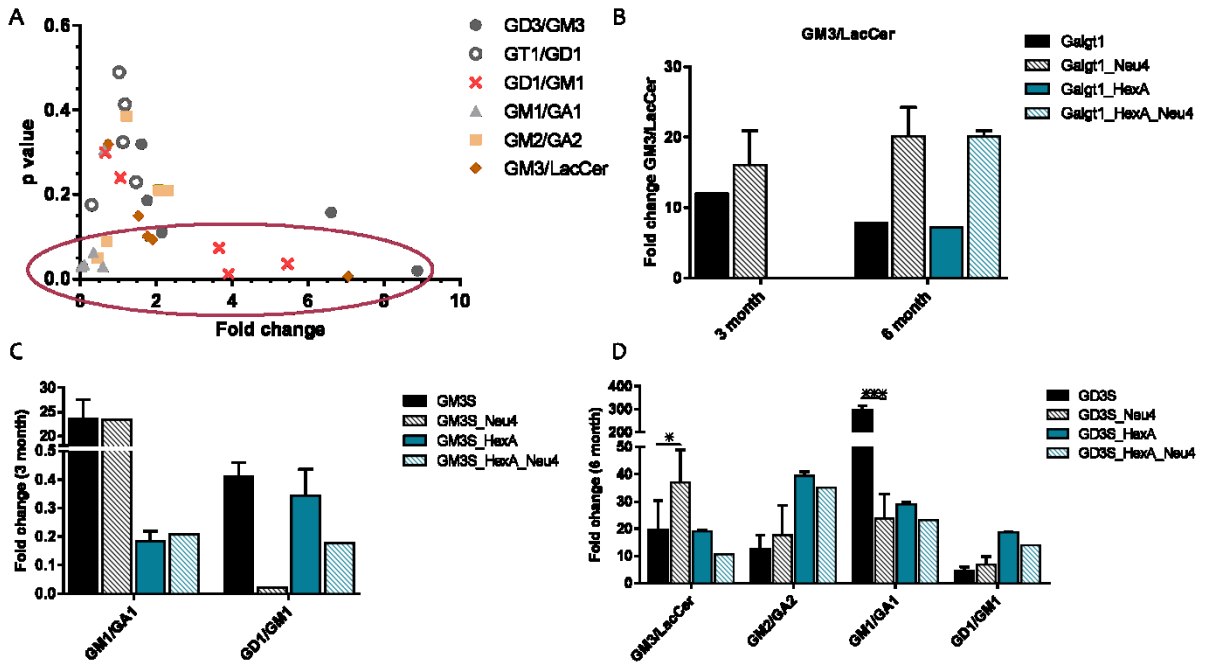

Figure 17: Ganglioside pattern in mouse models of Tay-Sachs disease (TSD) and neuraminidase 4. A: Scatter-plot reflecting the foldchange of Neu4/WT, Neu4_HexA/HexA, Neu4_GM2AP/GM2AP of mouse brains with the age of 3 and 6 month. Red circle highlights significant changes for GM3/LacCer, GM1/GA1, GD1/GM1 and GD3/GM3 levles (N=3). B: GM3/LacCer levels increase in knockouts where Neu4 is incorporated in the background of Galgt1 (N=3, except Galgt1 N=1). C: GD1α or c/GM1b decrease in mice with combined GM3S and Neu4 deficiency (N=3, except GM3S_Neu4 and GM3S_HexA_Neu4 N=1). D: GM3/LacCer increase and GM1/GA1 decrease detected in GD3S KO mice combined with Neu4 deficiency (N=3-4).

3.2.2 Neuraminidase 3

In parallel to the evaluation of neuraminidase 4 (Neu4) role in the bypass of GM2 degradation, neuraminidase 3 was investigated as a likely candidate for Tay-Sachs disease medical investments [85]. On the basis of the HILIC-MS/MS analytic of Neu4 mouse models described earlier in this work, Neu3$^{-/-}$ deficient mouse brain samples with the age of 2.5 and 4.5 month combined with the mouse model of Tay-Sachs disease (HexA$^{-/-}$) were investigated. Prior to HILIC-MS/MS analysis thin layer chromatography (TLC) was performed according to the method described in material and methods. Already the TLC showed the massive accumulation of GM2 in the double knockout of Neu3$^{-/-}$/HexA$^{-/-}$ mice brains compared to the detected GM2 accumulation on only HexA$^{-/-}$ mice (Figure 18). The mass spectrometric data confirmed the severe GM2 accumulation with additional increased values of GA2, GM3 and LacCer, but not GA1 or GM1 (Figure 18).

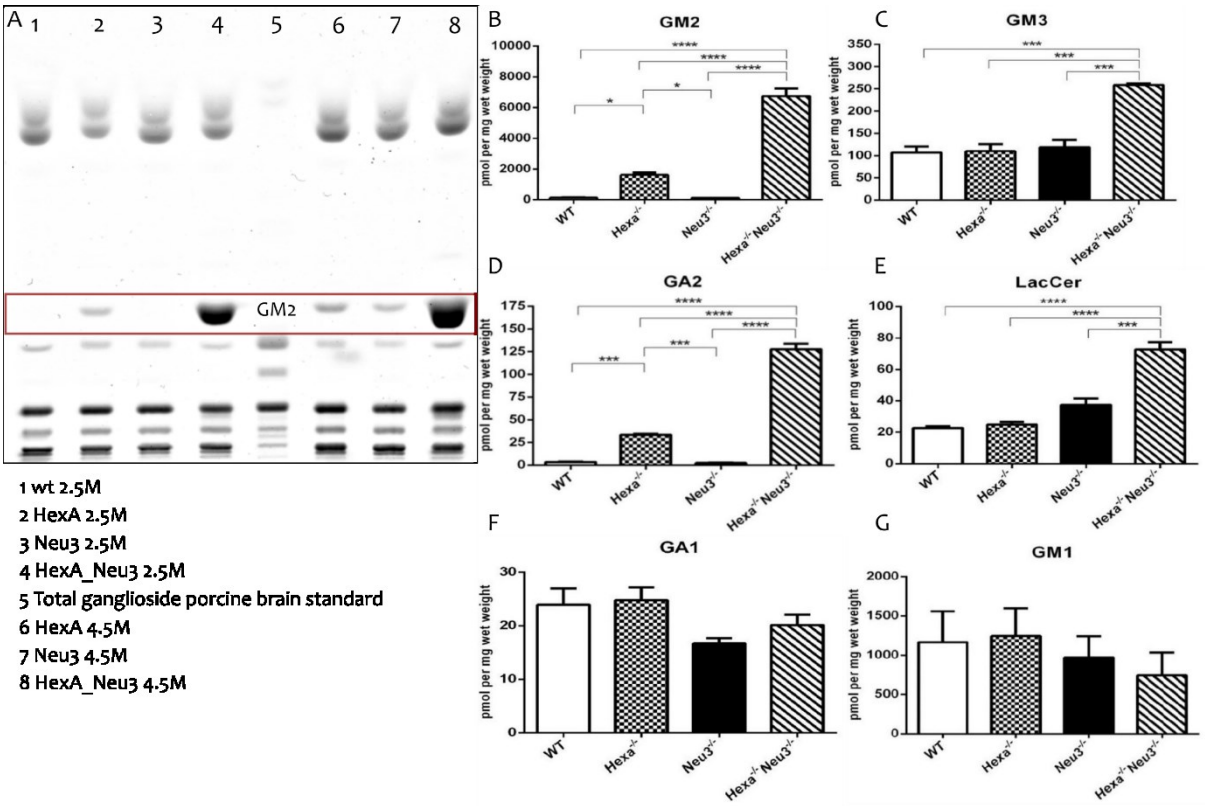

Figure 18: Ganglioside GM2 accumulation in a mouse model of Tay-Sachs disease combined with Neuraminidase 3 deficiency. A: TLC of acidic GSL fraction from mouse brain lipid extracts. GM2 accumulation is displayed in Hex$^{-/-}$ and more prominent in HexA$^{-/-}$/Neu3$^{-/-}$ brains of 2.5 and 4.5 month old mice. Light GM2 band of Neu3$^{-/-}$ brain only detectable for age of 4.5 month. B-G: LC-MS/MS analysis of gangliosides in mouse brain extracts. GM2 and GA2 accumulation is higher in double knockout mouse brains of mice with the age of 4.5 month. Additional GM3 and LacCer enhancement is detected and no changes in GA1 and GM1 levels. N = 3, mean ± SEM.

3.3 Mass spectrometric imaging - method development for comparison of DESI-MS/MS and MALDI-TOF

LC-MS/MS analytic has limits when it comes to the localization of distinct substances into special tissue compartments of organs. While it is possible to dissect a mouse brain in different areas such as cortex, cerebellum, hippocampus or hypothalamus prior to lipid extraction and LC-MS/MS analysis, it is time-consuming and experts are necessary. Mass spectrometric imaging is a technique to circumvent these drawbacks. It is able to screen tissue sections and generate mass spectra for each pixel to finally show reconstructed images for distinct masses with intensities as local distribution. Matrix-assisted laser desorption ionization (MALDI) has become the current standard for mass spectrometry imaging, however there are other methods that seems content for future analysis. DESI is an ambient ionization method based on principles similar to electrospray ionization (ESI). Combining DESI with tandem-mass spectrometry using SRMs would add specificity to conventional imaging MS, and specific

information about defined lipid (ganglioside) locations can be gained. The advantage of DESI in comparison to other imaging techniques is the reduction of sample preparation and the relative high velocity of the measurements. In the following chapter the development of DESI-MS/MS methods for measuring lipids (gangliosides) in mouse brain sections and its direct comparison to MALDI-TOF is described.

3.3.1 DESI-MS/MS

The signal intensity of desorption electrospray ionization (DESI) is highly dependent on the geometric parameter of the DESI-source, especially capillary tip to MS inlet distance, capillary tip to surface distance, MS inlet to surface distance and MS inlet to surface angle (Figure 19). These parameters were roughly set by using a Sharpie marker and detecting the rhodamine (m/z 443). Additionally, optimal nitrogen pressure, spray solvent, spray solvent flow rate and capillary voltage were determined (Figure 19).

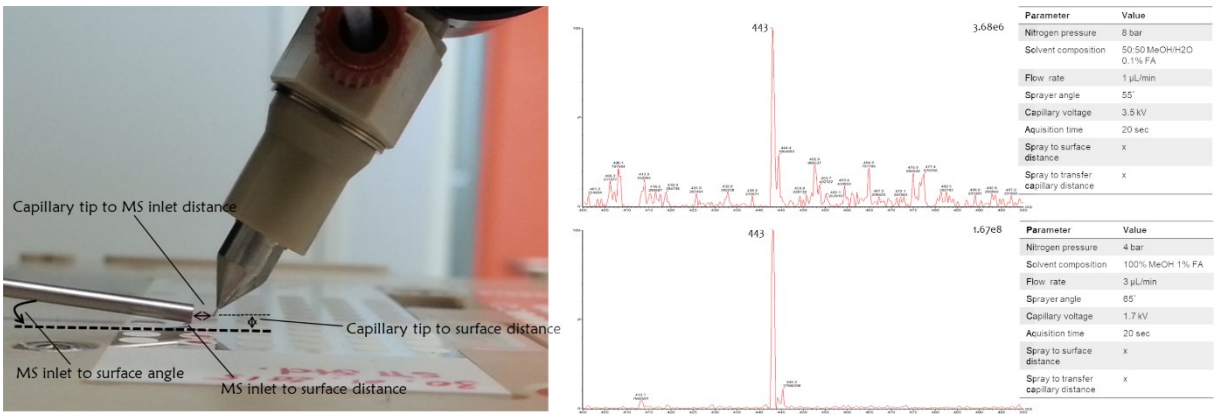

Figure 19: DESI geometry and DESI parameter for optimization and rhodamine signal.

Sphingomyelin was used as a standard to improve the parameters for the analysis of sphingolipids. Further, the precursor ion scan (and finally SRM) as a new tool for mass spectrometry imaging was tested. Spots with a volume of 1 µL containing 0.1 mg/mL sphingomyelin in methanol were placed on special DESI slides prepared with a roughened surface for better ionization and let dry. DESI acquisition was performed using a constant velocity with 300 µm/sec over a defined number of standard spots to compare signal changes. Precursor ion scan of m/z 184, representing the head group loss of phosphatidylcholine in positive ion mode, showed reproducible signals for each standard spot. Five structurally different sphingomyelin compartments in the standard were identified (Figure 20).

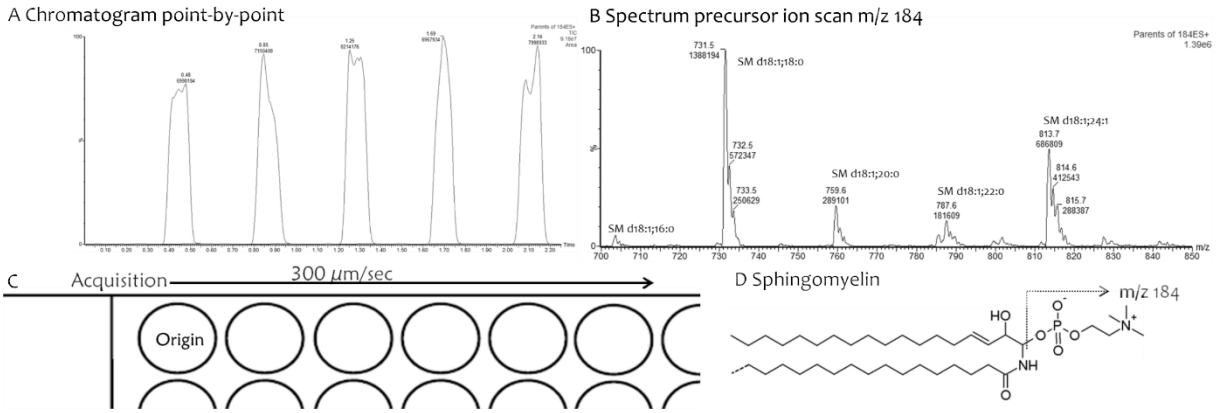

Figure 20: DESI parameter optimization by sphingomyelin standard (0.1 mg/mL; 1 µL droplet) acquisition with constant velocity (300 µm/sec) point-by-point setting (A and C) in precursor ion scan mode for m/z 184 (B and D).

For investigating sphingomyelin on brain tissue cryo-sections of fresh frozen brains with 12 µm thickness were generated and measured by DESI-MS/MS in full scan mode as well as precursor ion mode for m/z 184 without further sample preparation. Two spray solvent systems (pure methanol without additives and 95% methanol in water (v/v) with 1% formic acid) that showed moderate signal sensitivities for standard detection were tested on the brain tissue slices. Pure methanol extractions led to a mass spectrum in full scan mode with the typical phospholipid pattern of mouse brain. Water and formic acid addition caused a reduction in signal intensity of these phospholipids as well as additional peaks in the range of m/z 600-700. Nevertheless, the precursor ion scan for m/z 184 showed clear signals for sphingomyelin and phosphatidylcholine (PC) revealing a more specific and more sensitive approach for mass spectrometric imaging (Figure 21).

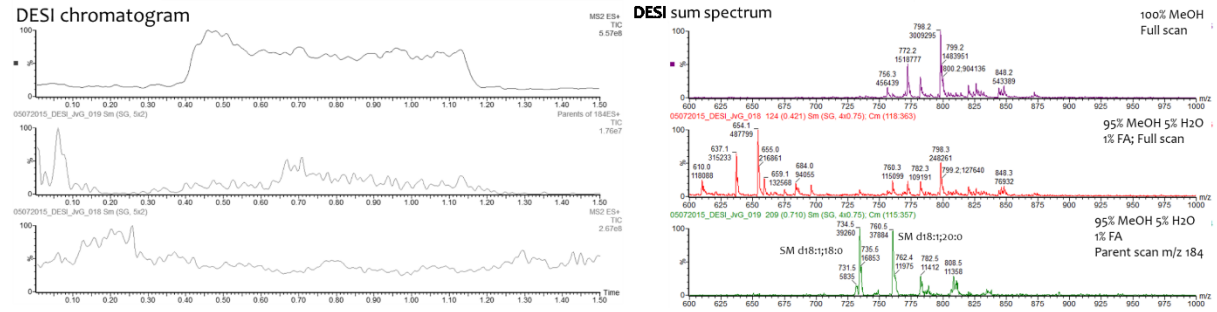

Figure 21: DESI chromatogram and spectrum for brain tissue acquisition in full scan positive mode and precursor ion scan of m/z 184.

To enhance sensitivity for fresh frozen tissues measured with DESI-MS/MS different types of wash steps as sample preparation were evaluated. Brain slices from WT mice were washed by applying 200 µL of either 10% acetic acid, 40% methanol, 10 mM ammonium acetate or 1:1 $CHCl_3$/acetone (v/v). Incubation was performed for 20 seconds and solutions removed by vacuum. Sphingomyelin (SM) and phosphatidylcholine (PC) were measured by scanning the

cerebellum in precursor ion scan for m/z 184. Sphingomyelin signal was enhanced with 10% acetic acid and 40% methanol treatment, but PC signals were not affected (Figure 22). Additionally, signal stability of detected SM and PC decreased with all tested wash steps, indicating a drop in robustness. Gangliosides and SM show similar sensitivity in the brain and appear only in small amounts compared to phospholipids, especially phosphatidylcholine. Further the ionization efficacy is not as efficient as the ionization of PC. To increase detection of ganglioside and sphingomyelin a sample preparation similar to LC-MS/MS was tested. By using an on-tissue saponification the phospholipid signals of brain tissue should be decreased. Therefore a solution of 0.1 M KOH in 40% or 10% methanol in water (v/v) were sprayed on fresh frozen brain slices either untreated or washed with 10% acetic acid by SunChrome spotter (35 µL/min, five repeats, total of 10 µL) and incubated for 2 hours at 37°C in a humidity chamber. Hydrolysis was performed on-slide and in-solution as positive controls and an untreated brain lipid standard was applied prior to incubation as negative control. Brains were measured by DESI-MS/MS in precursor ion scan mode for m/z 184 as well as MALDI-TOF/TOF on the same slide (Figure 23). The DESI images yielded no clear results for enhanced signal sensitivities when washed with 10% acetic acid and treated with 0.1 M KOH solution. Possible negative effects of spraying the KOH solution were excluded by comparing the signals of sprayed tissue with signals detected when a 30 µL droplet of 0.1 M KOH was applied. Again, fresh frozen brain slices were used and either no treatment, washing with 10% acetic acid, KOH droplet and washing, and KOH sprayed and washing tested after incubation at 37°C for 2 hours. Slides were measured with DESI-MS/MS in precursor ion mode for m/z 184 and MALDI-TOF/TOF. The DESI-MS/MS result images showed a highly unstable signal generation over the scanned tissue. Nevertheless, the signals of tissue treated with a droplet of KOH did not differ from the control tissues, the spray-method seemed to show a degrading effect besides the unchanged sphingomyelin signal (Figure 23). As the signals generated with DESI turned out to be highly unstable, all described sample preparation testing was in addition performed with MALDI-TOF/TOF on the same slides as the DESI-MS/MS detection to confirm the results (Appendix II).

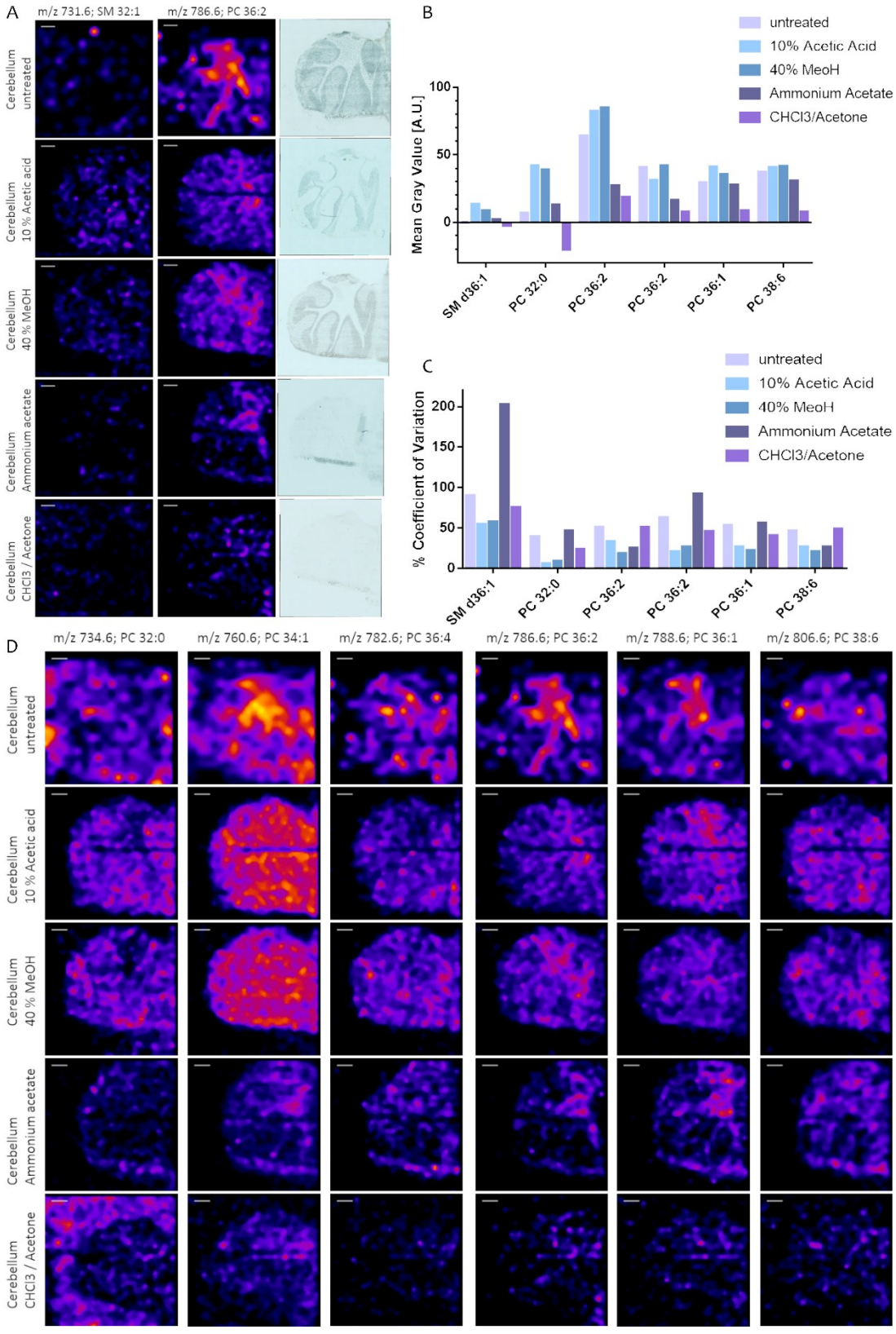

Figure 22: Sample preparation test for DESI-MS/MS scanning mouse WT cerebellum with precursor ion scan for m/z 184 and detecting sphingomyelin and phosphatidylcholine. A and D: Comparison of sphingomyelin (SM) and phosphatidylcholine (PC) signal for untreated, 10% acetic acid, 40% MeOH, ammonium acetate and 1:1 $CHCl_3$/acetone (v/v) cerebellum images. B and C: Mean gray value and variation within one cerebellum evaluated with ImageJ. SM and PC signals show no changes after wash treatment and the signal variation over the tissues decreased, which may be due to dislocation effects of the solvent droplets.

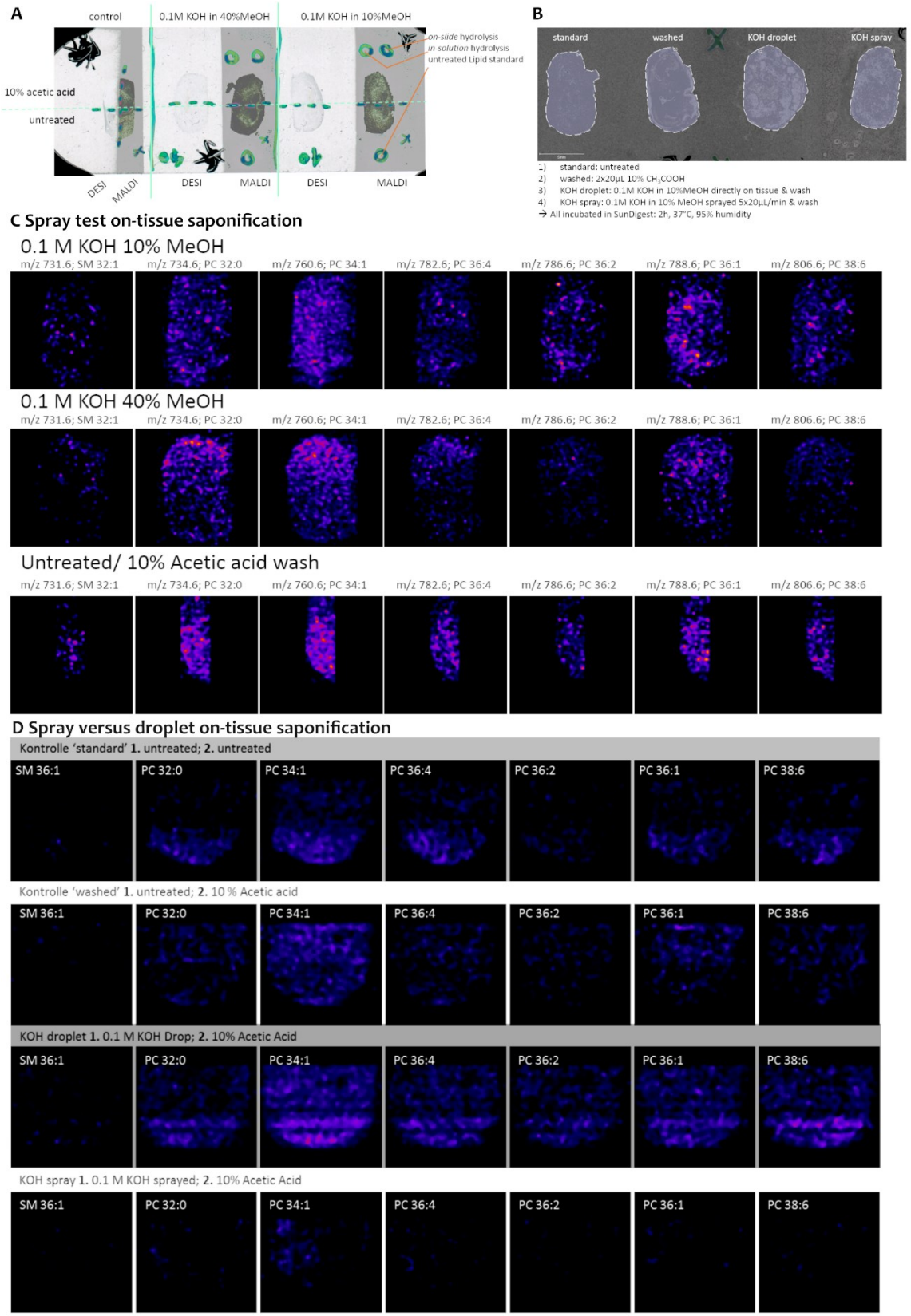

Figure 23: Sample preparation test for the on-tissue saponification of phospholipids with 0.1 M KOH. A and C: WT brain slices were measured, untreated or washed with 10% acetic acid, after saponification with 0.1M KOH in 40% or 10% methanol sprayed with SunChrome spotter. B and D: WT brain slices were measured untreated, washed with 10% acetic acid and after saponification with 0.1 M KOH sprayed and applied as 30 µL droplet. Sphingomyelin (SM) and phosphatidylcholine (PC) were measured with DESI-MS/MS by precursor ion scan of m/z 184.

Finally, the negative ion mode with DESI-MS/MS were investigated, and as in positive ion mode, no gangliosides could be detected (not shown). Brain slices of fresh frozen WT mice were measured in full scan and precursor ion scan for m/z 241 in negative ion mode, using a spray solvent of 90:10 methanol/water (v/v) according to Skraskova *et al* [151]. Expected signals for phosphatidylserine (PS) and phosphatidylinositol (PI) as well as signals for sulfatides could not be detected or confirmed with precursor ion scan (Figure 24).

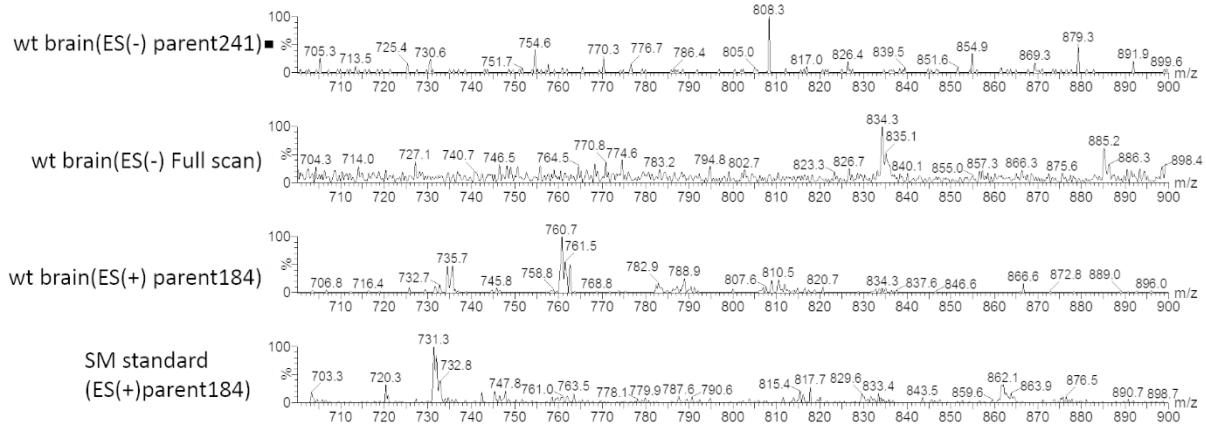

Figure 24: DESI-MS/MS analysis of wt mouse brain lipids in negative ion mode with full scan (bottom) and precursor ion scan of m/z 241 for phosphatidylinositol (PI) and phosphatidylserine (PS) (top). Full scan displayed two main peaks, whereby m/z 885 would correspond to PI(38:4) and m/z 834 to PS(40:6). Both peaks were not detectable in precursor ion scan and therefore do not reflect PI or PS lipid species.

3.3.2 DESI-MS/MS in direct analogy to MALDI-TOF

Certainty about the advantages DESI-MS/MS could bring will only be achieved by comparing the results with MALDI-TOF, the current standard for mass spectrometry imaging. Serial cryo-sections of sagittal brain halves from Bl6 WT mice were made and H&E staining as well as either MALDI-TOF or DESI-MS/MS analysis of the cerebellum performed. Images of certain sphingolipids were generated and mean mass spectra over the whole cerebellum were extracted and compared after data processing such as baseline correction, peak picking and alignment (Figure 25). Additionally, a set of different wash steps for fresh frozen tissue sections and its influence on mass spectrometric imaging were investigated.

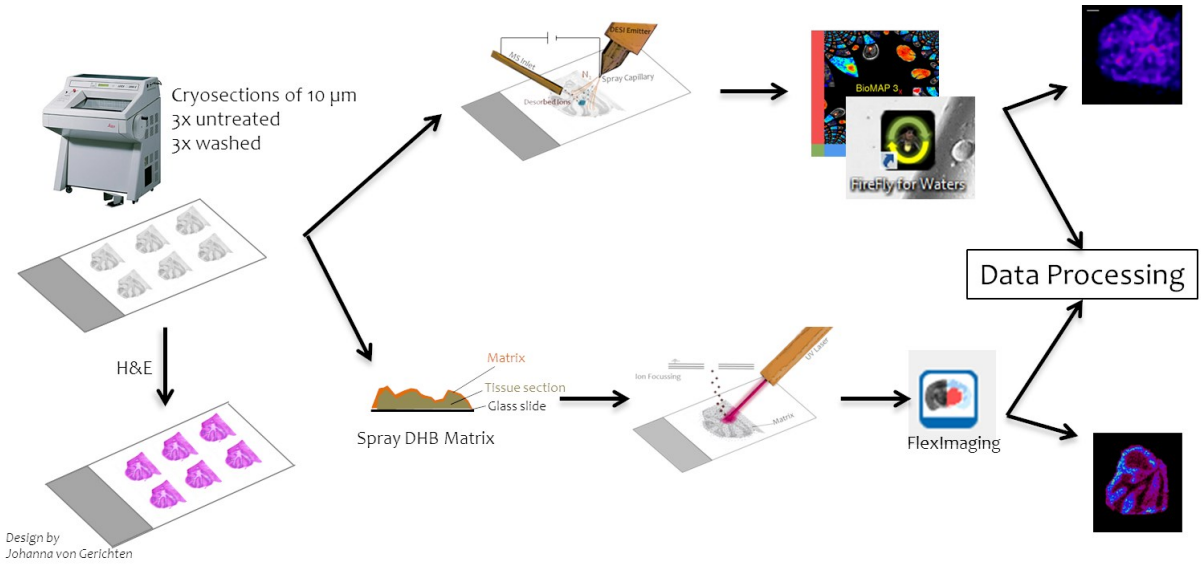

Figure 25: Workflow DESI-MS/MS and MALDI-TOF comparison. In brief, subsequent fresh frozen brain sections (sagittal) of mouse cerebellum were measured in parallel with DESI-MS/MS and MALDI-TOF, as well as stained with H&E protocol. Images were generated with each manufacturer software (Biomap/FlexImaging) and spectrum data were exported and further processed with self-written MATLAB manuscript and SCiLS software.

The ionization pattern of DESI and MALDI was comparable for brain phospholipids in full scan positive ion mode showing mainly phosphatidylcholine (PC) in the mass spectra and revealing potassium as well as sodium adducts with even higher signal intensities as corresponding protonated peaks. DESI-MS/MS showed enhanced sensitivity and specificity in precursor ion scan of m/z 184 by significantly reducing background noise and adduct ions. To enhance signal sensitivity and ionization efficacy different wash steps were tested (3.3.1), whereby 10% acetic acid applied in a 100 µL layer on the brain tissue for 20 seconds displayed the most improvement on phospholipid detection. The increased signal intensities by a simple wash step were also fact for MALDI imaging as the washing removes most of the salt-adduct ions. Therefore phospholipid pattern of MALDI mass spectra were detected similar to patterns of DESI product ion scan mass spectra. The wash step improved the reproducibility of MALDI tissue-to-tissue detection, too. Overall sensitivity and ionization efficacy of MALDI was shown to be higher compared to DESI (Figure 26). Nevertheless, the spatial resolution of DESI did not reveal the typical tissue structure of the cerebellum (grey and white matter), which roughly means less than 200 µm resolution power was achieved.

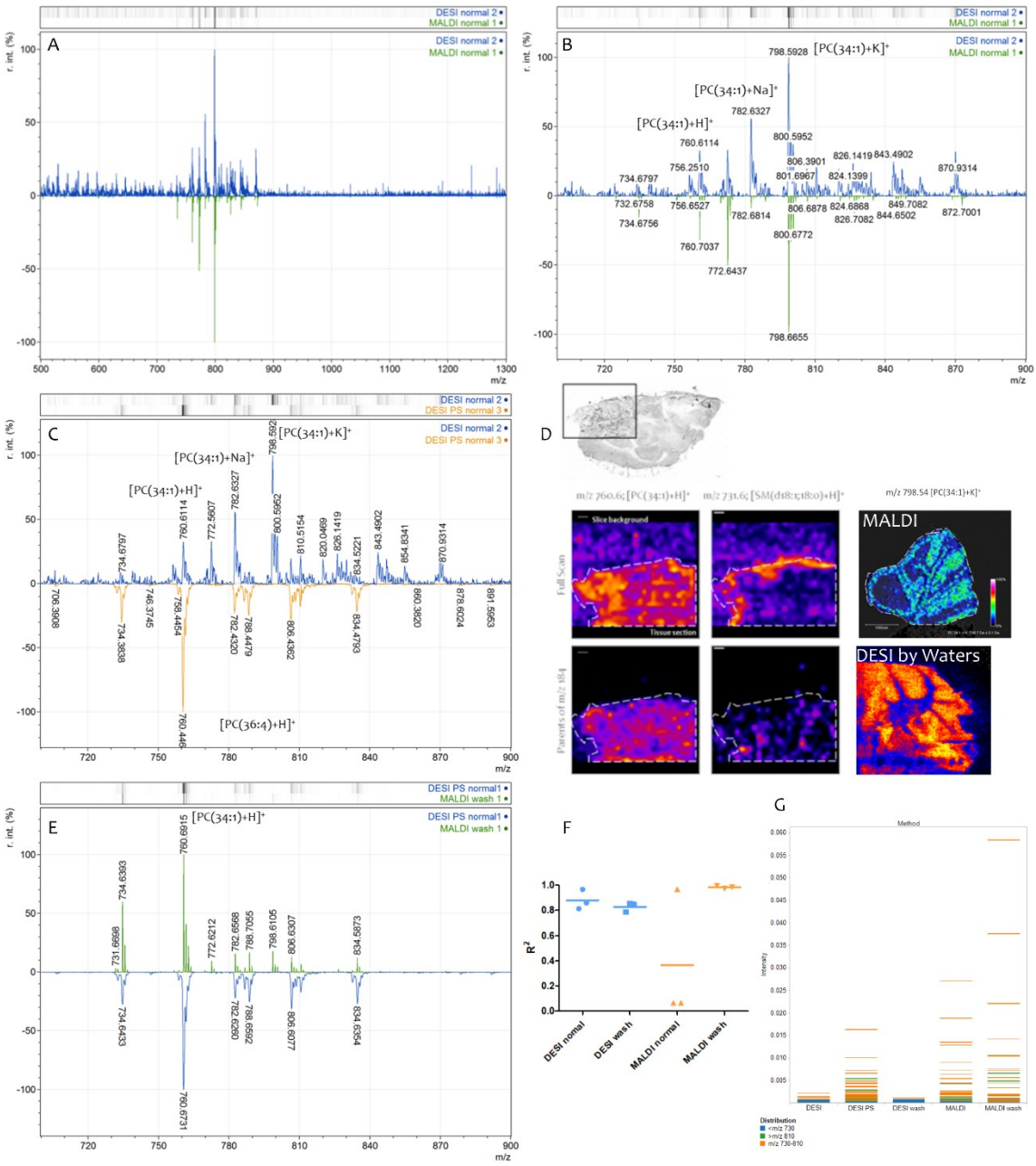

Figure 26: DESI and MALDI comparison in positive ion mode using fresh frozen brain sections in combination with precursor ion mode of m/z 184 for sphingomyelin (SM) and phosphatidylcholine (PC) in combination with wash steps. A: Overview full scan (FS) spectra of DESI (blue) and MALDI (green) showing a similar peak pattern. B: Zoom FS spectra m/z 700-900 displaying typical PC brain pattern with similar ionization of protonated PC, sodium adduct and potassium adduct for DESI and MALDI. C: DESI FS and DESI precursor ion scan (PS) of m/z 184 (yellow) spectra of mouse brain cerebellum showing enhanced S/N ratios for peaks. D: DESI Images of SM (right) and PC (left) in full scan (upper) and PS of m/z 184 (lower) reflecting the drop in background signals (black). Images of cerebellum gained with MALDI (upper) and improved DESI by Waters anticipating the low spatial resolution of the DESI source used in the Sandhoff lab. E: DESI PS of m/z 184 (blue) and MALDI after 10% acetic acid wash (green) spectra of mouse cerebellum displaying the similar ionization patterns. F: Inter-tissue reproducibility reflecting the importance of a wash step for MALDI acquisition. G: Absolute intensities of PC and SM peaks generated by the different methods – DESI FS, DESI PS, DESI wash, MALDI FS, MALDI wash – revealing MALDI in combination with a 10% acetic acid wash step as the most sensitive and stable MS imaging method for lipids in the positive mode. (N=3)

3.4 Local GM2 distribution in mouse brains of Tay-Sachs disease and Neuraminidase deficiency

The main GM2 accumulation in mouse brain was previously reported to regions of hippocampus and cortex using a GM2 antibody [102]. The local distribution of GM2 and the associated expression of neuraminidases is of high interest as there is not much known about the human sialidases and their chance for being therapeutic targets. Imaging mass spectrometry is a label-free, semi-quantitative method to measure not only GM2 but many other gangliosides and lipids simultaneously, which can be combined with immunohistochemistry or *in situ* hybridization. As DESI-MSI appeared not suitable, MSI was performed with a MAIDI-TOF instrument. This chapter reveals and compares the GM2 accumulation and general ganglioside pattern in Neu4 and Neu3 deficient mouse brains combined with mouse models of Tay-Sachs disease.

3.4.1 Neuraminidase 4

MALDI-TOF/TOF analysis of sagittal mouse brain cryo-sections were performed as described in material and methods (2.3.4). Images for each ganglioside of interest were generated from the average mass spectra The signals represent masses corresponding to gangliosides with d36:1 ceramide backbone which is mainly d18:1;18:0 as revealed by (+)ESI-MS/MS. In three month old brain samples of $HexA^{-/-}$, $Neu4^{-/-}HexA^{-/-}$, $GM2AP^{-/-}$, $Neu4^{-/-}GM2AP^{-/-}$, $HexA^{-/-}GM2AP^{-/-}$ and $Neu4^{-/-}HexA^{-/-}GM2AP^{-/-}$ a GM2 accumulation was detected, but not in $Neu4^{-/-}$ brain (Figure 27). A higher accumulation of GM2 in brains of $Neu4^{-/-}HexA^{-/-}$ compared to $HexA^{-/-}$ were confirmed. GM2 accumulation seems to start in regions of hippocampus, cortex and olfactory bulb in $HexA^{-/-}$ and $Neu4^{-/-}HexA^{-/-}$ mice, and an additional accumulation in the cerebellum was detected when $GM2AP^{-/-}$ deficiency is present. Especially in genotypes with highest GM2 accumulation such as $HexA^{-/-}GM2AP^{-/-}$ and $Neu4^{-/-}HexA^{-/-}GM2AP^{-/-}$ a very specific GM2 signal in structures of cerebellum, hippocampus, cortex, olfactory bulb and hypothalamus were presented. More detailed analysis by visualizing the data as GM2/GM1 ratio for each single brain region showed that ganglioside changes are specific to Neu4 in hippocampus and olfactory bulb (Figure 27). Other gangliosides such as GM1 and GD1 were more widely distributed and did not display such a specific accumulation compared to GM2. Similar but less pronounced results were obtained with gangliosides containing a longer ceramide anchor (d38:1) (Appendix III).

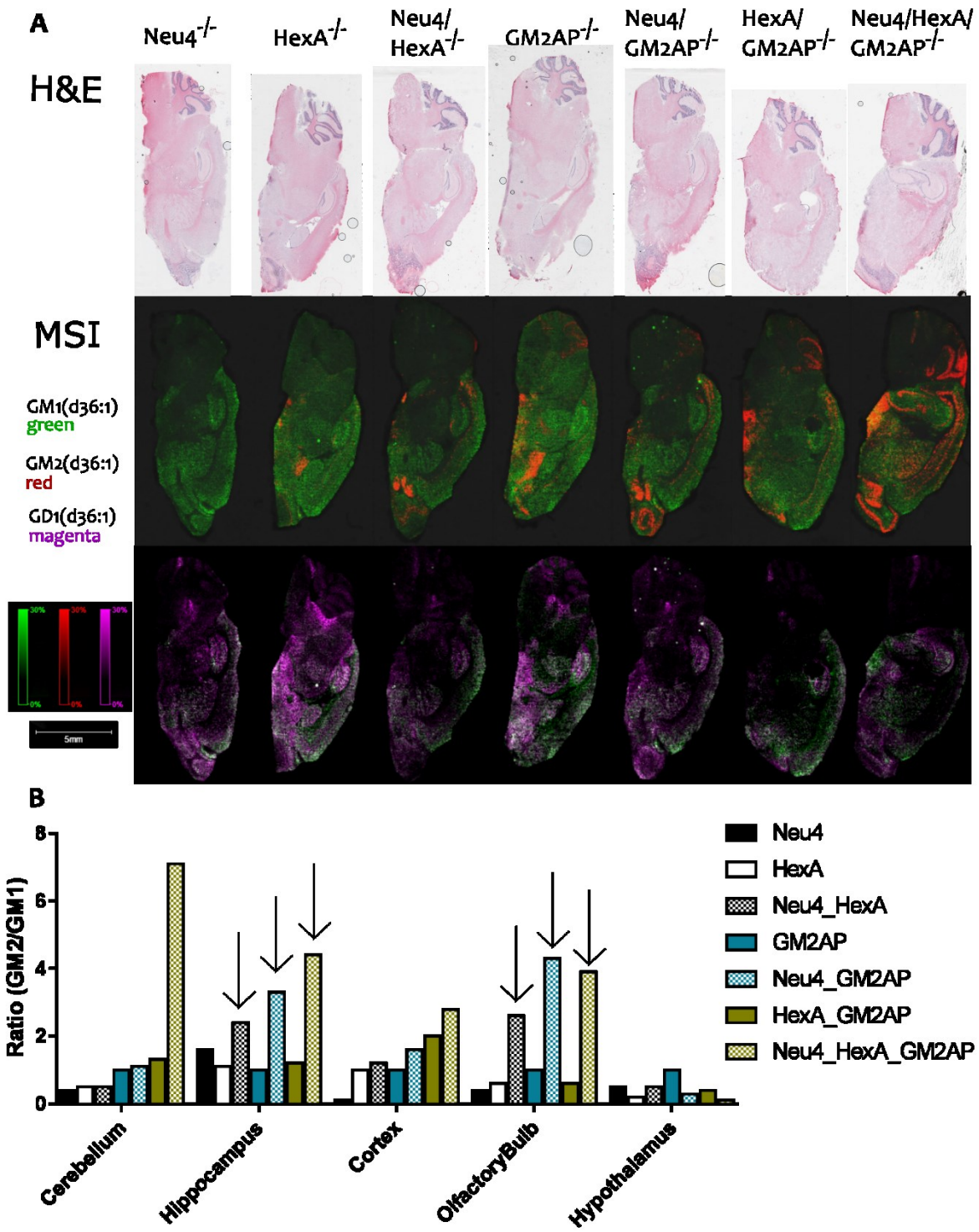

Figure 27: MALDI-TOF MSI of GM1, GM2 and GD1 in sagittal mouse brain slices of 3 month old GM2 gangliosidosis and Neu4 models. Fresh frozen brain slices were measured with DHB matrix in reflector negative mode with spatial resolution of 50 µm (A). Images were analyzed more detailed with SCiLs, whereby ROI of distinct tissue regions were selected by hand and mean signal intensity per ROI exported and shown in (B).

Brain samples of six month old mice were analyzed in the same manner to the above mentioned three month old samples (Figure 28). The results are comparable, showing GM2 accumulation in a very specific manner for regions of cerebellum, hippocampus, cortex, hypothalamus and olfactory bulb. The GM2AP$^{-/-}$ brain sample seemed to show no GM2 signal

at all, which has to be discussed. Samples with GD3S$^{-/-}$ background displayed no additional GM2 accumulation when combined with Neu4 deficiency. Similar but less pronounced results were obtained with gangliosides containing a longer ceramide anchor (d38:1) (Appendix IV).

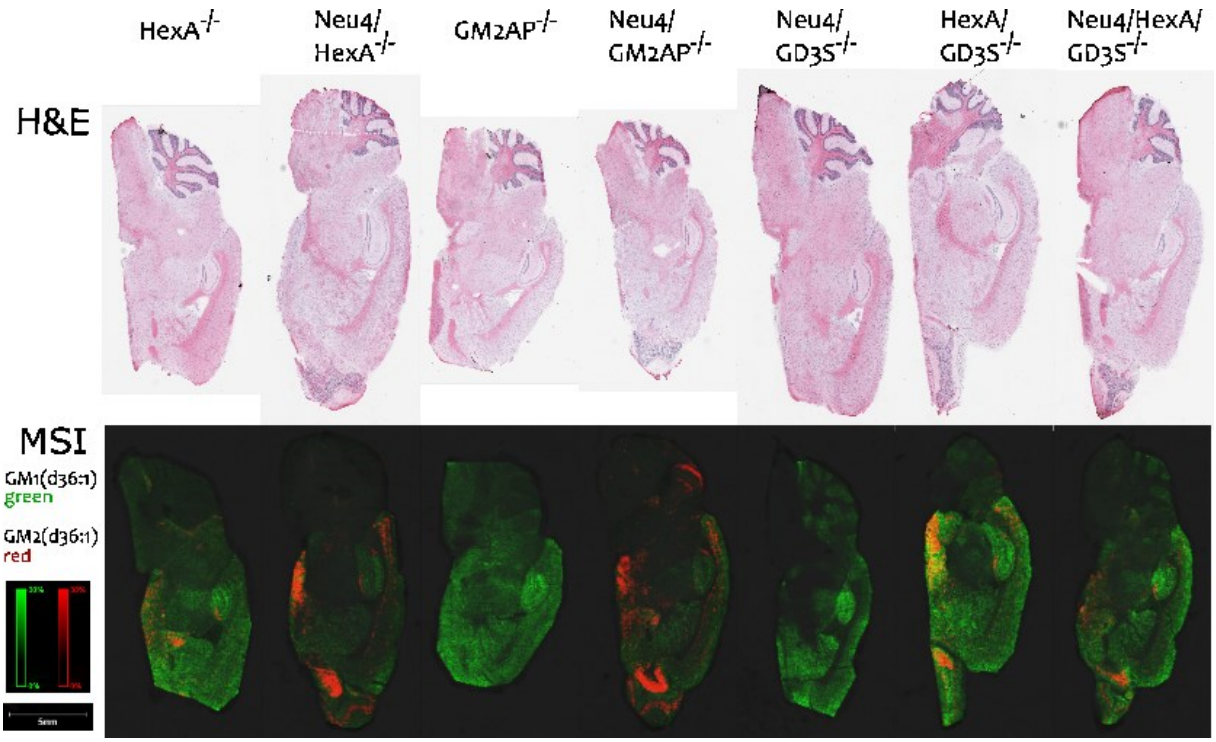

Figure 28: MALDI-TOF MSI of GM1, GM2 and GD1 in sagittal mouse brain slices of 6 month old GM2 gangliosidosis, GD3S$^{-/-}$ and Neu4$^{-/-}$ models. Fresh frozen brain slices were measured with DHB matrix in reflector negative mode with spatial resolution of 50 µm.

3.4.2 Neuraminidase 3

MALDI-TOF/TOF analysis for ganglioside pattern in mouse brains of Tay-Sachs disease combined with neuraminidase 3 (Neu3) deficiency were operated in tissue of 4.5 month old mice as described in material and methods (2.3.4). The GM2 accumulation was more severe compared to the neuraminidase 4 (Neu4) deficient samples, which was also shown with LC-MS/MS. Additionally, minor amounts of GA2, the direct metabolite of GM2, were detected. The storage pattern of GM2 was similar in the Neu3 deficient brains compared to the Neu4 deficient imaging results with the prominent areas of cerebellum, cortex, hippocampus, hypothalamus and olfactory bulb, but the overall signal was more diffuse and not as specific. Especially the fine linearly structure of GM2 signal in brains of Neu4 deficiency, which could be correlated to the corpus callosum, was not obvious in brains with Neu3 deficiency (Figure 29).

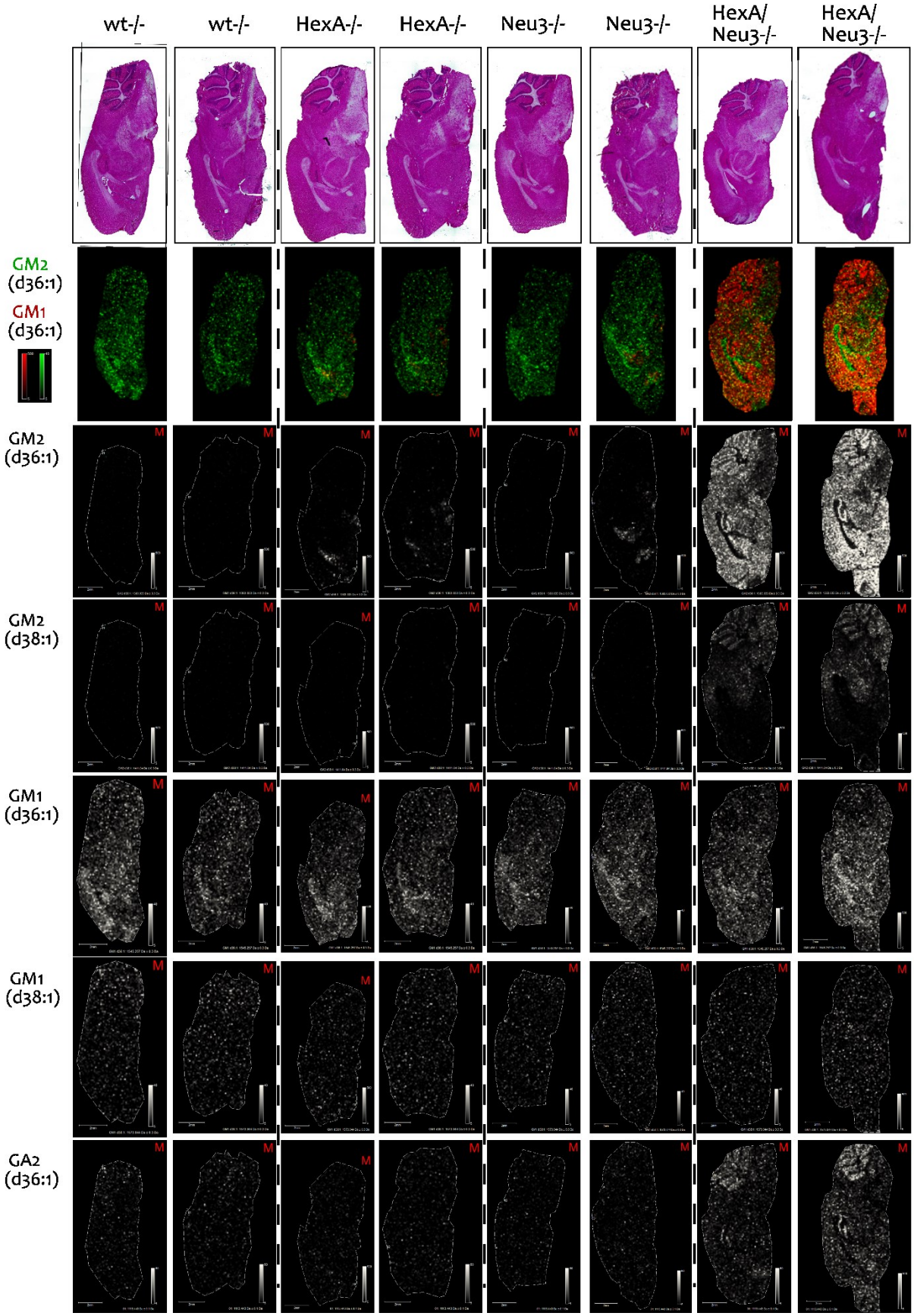

Figure 29: MALDI-TOF MSI of GM1, GM2 and GA2 in sagittal mouse brain slices of 4.5 month old GM2 gangliosidosis and Neu4 models. Fresh frozen brain slices were measured with phenyl-cyano-cinnamamide matrix in reflector negative mode with spatial resolution of 100 µm.

3.5 LC-MS/MS method development for the separation of hexosylceramides

In mammalian tissue the two main isoforms of hexosylceramide (HexCer) are β-glucosylceramide (β-GlcCer) and β-galactosylceramide (β-GalCer) [176]. Alpha-anomeric HexCers are described for marine sponge and bacteria [13,14]. With conventional mass spectrometry and fragmentation these isoforms can't be separated as they display the same mass. Most LC applications such as RP18 separation cannot differ between them as β-GlcCer and β-GalCer contain the same structure only differing in the stereochemistry of the hydroxyl group at position 4 (Figure 30).

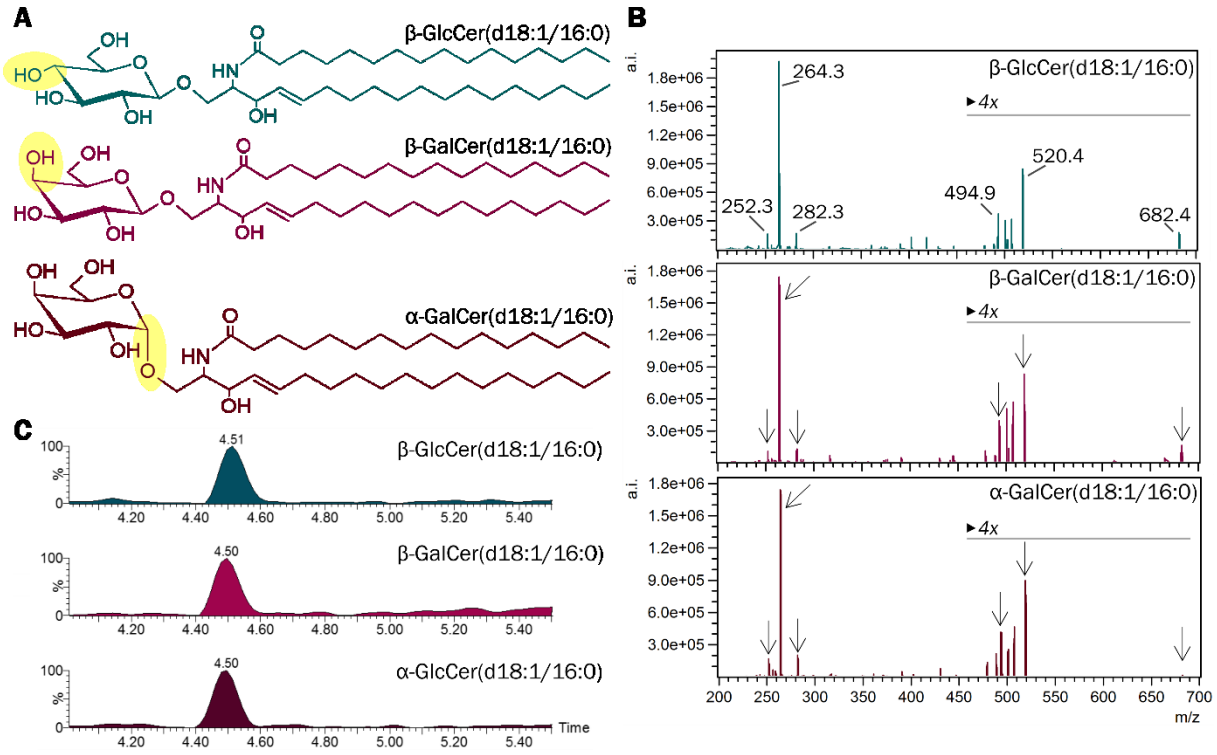

Figure 30: A: Stereochemical structures of β-GlcCer, β-GalCer, and α-GalCer containing a C18-sphingosine and an N-linked palmitic acid [HexCer(d18:1/16:0)]. B: Product ion spectra of corresponding HexCers obtained at 25 eV collision energy by ultra- performance LC-ESI-triple quadrupole MS2. Note, abundant product ions are detected in all three compounds. C: Extracted ion chromatograms from reversed phase chromatography (CSH C18) for the detection of HexCer(d18:1/16:0) from the three diastereomers, β-GlcCer, β-GalCer, and α-GalCer. Note the identical retention time of all three compounds [167].

3.5.1 Liquid chromatography (HILIC) parameter optimization and separation of HexCer isoforms β-GlcCer, β-GalCer and α-GalCer

With normal phase-high performance thin layer chromatography (HPTLC), all 4 stereoisomeric hexosylceramide standards can be separated, if the HPTLC plate had been impregnated with borate [165,166] and, if they contain identical ceramide anchors (Figure 31).

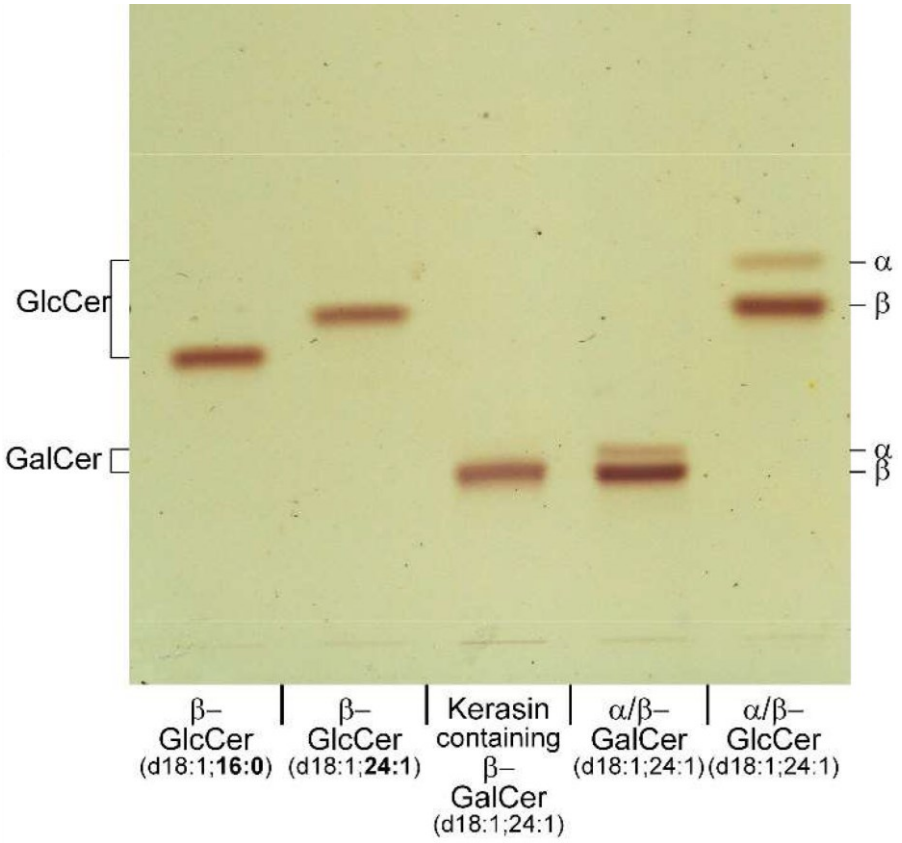

Figure 31: Various hexosylceramide standards were separated on a borate pre-impregnated normal phase HPTLC-plate and visualized with orcinol reagent. Note, all GalCers are retarded much stronger than any GlcCer due to complexation with borate. Furthermore, alpha-GlcCer and alpha-GalCer separate from their corresponding beta-anomers and migrate faster. However, retention times also depend on the type of attached ceramide anchor. β-GlcCer(d18:1;16:0), Rf = 0.34; β-GlcCer(d18:1;24:1), Rf = 0.39; Kerasin containing mainly β-GalCer(d18:1;24:1), Rf = 0.20; α/β-GalCer(d18:1;24:1), Rf = 0.22 and Rf = 0.2; and α/β-GlcCer(d18:1;24:1) Rf = 0.45 and Rf = 0.39. The α/β-HexCer mixtures contain about 15% α-anomer [167].

To quantitatively differentiate all four isomers in biological samples, chromatography has to be combined with information about the ceramide anchor. Therefore, a method for hydrophilic interaction chromatography coupled to tandem-mass spectrometry was developed. Initially, solvent gradient systems starting with 95-97% acetonitrile were used, but no separation of the stereoisomeric HexCer-mixtures on HILIC-columns used in the laboratory was observed (data

not shown). Consequently, the hydrophobicity of the starting solvent (solvent A) was increased: acetonitrile was exchanged by propionitrile and water (3%) exchanged by 2% of 2-butanol (since methanol in solvent A widened the peaks). In a gradient of increasing polarity solvent A was replaced by increasing proportions of solvent B (97% methanol, 2% 2-butanol, 1% water) in a nonlinear fashion using increasing steepness. As a result, β-GlcCer eluted first followed by β-GalCer, α-GlcCer and finally by α-GalCer, all of them containing the identical ceramide anchor Cer(d18:1/24:1) (Figure 32 A). Importantly, β-GlcCer and β-GalCer (R = 1.7) as well as β-GalCer and α-GalCer (R = 2.3) separated (R ≥ 1.5, Fig. 2A). Keeping β-GalCer constant at a concentration of 0.1 µg/mL, a dilution series of β-GlcCer followed a linear decreasing peak area and β-GlcCer was detected with an LOD of 2 ng/mL (25 fmol injected), corresponding to 1% of the abundant β-GalCer (Figure 32 B). Vice versa, keeping β-GlcCer constant (0.1 µg/mL), β-GalCer was detected in a dilution series down to an LOD of 7 ng/mL (86 fmol injected), corresponding to 5% of the abundant β-GlcCer (Figure 32 C). Furthermore, α-GalCer (75 ng/mL) could be quantified in the presence of 110fold concentration of the β-anomer (8 µg/mL) (Figure 32 D). Next, the retention times of endogenous hexosylceramides from mouse organs were investigated, with the initial and some further HexCer-standards: β-GlcCer(d18:1/(14 or 16 or 19 or 25:0), Kerasin (A mixture of NS type β-GalCers with non-hydroxy fatty acids (N) and sphingosine (S)), and Phrenosin (A mixture of AS type β-GalCers with α(R)-hydroxy fatty acids (A) and sphingosine (S)). Liver contains mainly NS-type β-GlcCers [177], stomach in addition substantial amounts of AS- and NP-type β-GlcCers [178], and intestine predominantly the AP-type besides AS-, and NP-type β-GlcCers [34,179,180]. Kidney is also enriched in β-GalCer [181,182] of the NS- and AS-type [177,183]. Combining data of retention times and associated MS^2-information (revealing the type of ceramide anchor) for standards and biological samples, decrease in retention times with longer acyl chain length were observed (roughly -0.016 ±0.005 min/CH_2-unit). Compared to NS-β-HexCer, corresponding AS-β-HexCer was delayed by +0.242 ±0.009 min, NP-HexCer by +0.084 ±0.004 min, and AP-HexCer by +0.282 ±0.008 min (Figure 32 E).

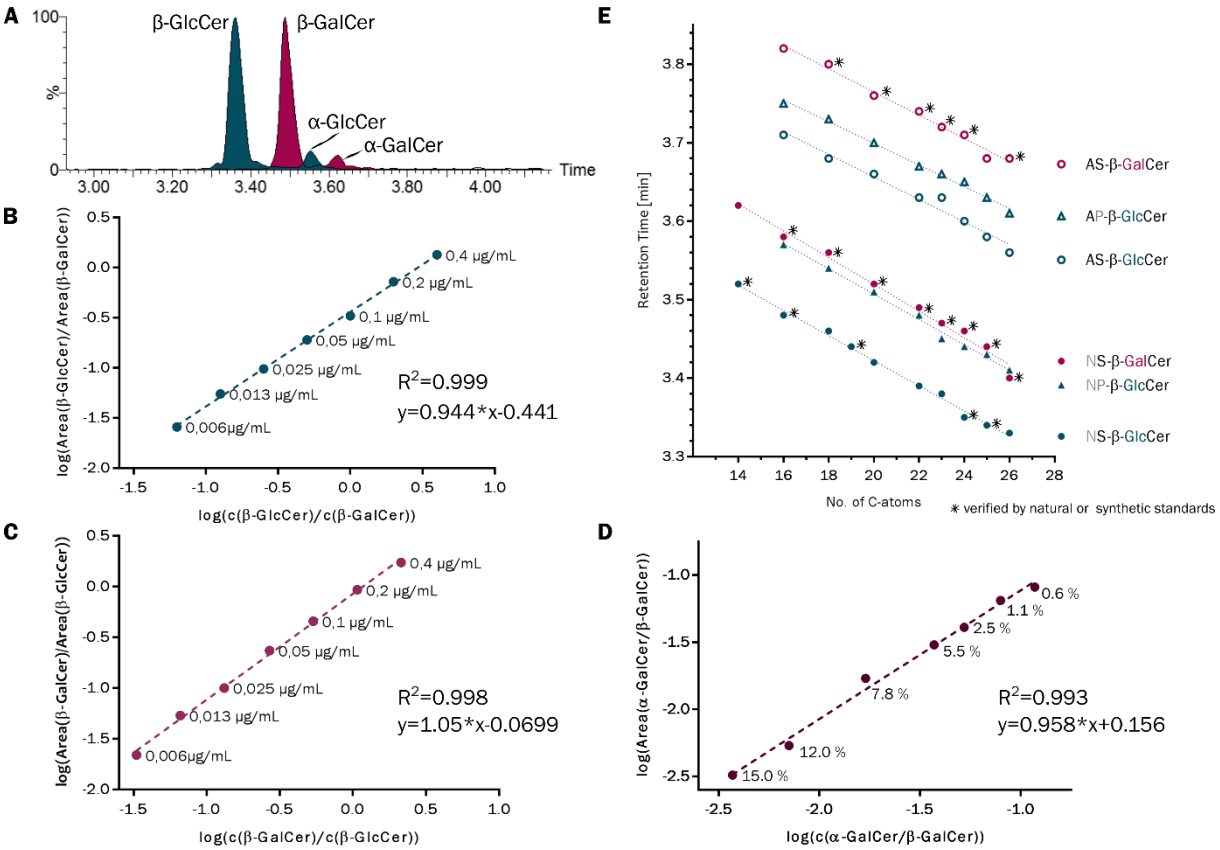

Figure 32: A: HILIC separation of a synthetic α/β-anomeric mixture of GlcCer(d18:1/24:1) (dark cyan) and a synthetic α/β-anomeric mixture of GalCer(d18:1/24:1) (red), each with approximately 15% α-content. B: Dilution of β-GlcCer(d18:1/24:1) in the presence of constant amounts of β-GalCer(d18:1/24:1). C: Dilution of β-GalCer(d18:1/24:1) in the presence of constant amounts of β-GlcCer(d18:1/24:1). D: Constant amounts of α-GalCer(d18:1/24:1) in the presence of increasing amounts of β-GalCer(d18:1/24:1). E: Retention times of standard HexCers marked with an asterisk and endogenous β-HexCers, which have been described in literature and were identified based on the behavior of standard compounds and on the molecular ion size. Note the relatively strong shift from nonhydroxy (NS) to α-hydroxy fatty acid containing compounds (AS), while introduction of phytosphingosine (NP) instead of sphingosine (NS) as well as decreasing acyl chain length contributed in a minor way to later elution. Additional double bonds as in HexCer[d18:1/24:1(15Z)] did not contribute to a significant retention time shift [167].

3.5.2 HILIC-MS/MS method proof-of-concept by comparison of HexCers with different ceramide composition in various mouse tissues

Applying the HILIC-MS²-based separation of β-GlcCer and β-GalCer, the distribution of both compounds in various mouse tissues were determined. The enrichment of β-GalCer mainly in brain (97%) and kidney (42%) was confirmed, and revealed in addition its abundance in lymph nodes (85%) and auricles (59%) (Figure 33). Results furthermore confirmed enrichment of nervonic acid within brain cerebrosides, whereas corresponding glucocerebrosides are enriched in stearic acid. The latter is the main acyl chain of neuronal gangliosides. Although

not always as clear cut, the acyl chain length distribution of cerebrosides and glucocerebrosides was not identical in any tissue investigated.

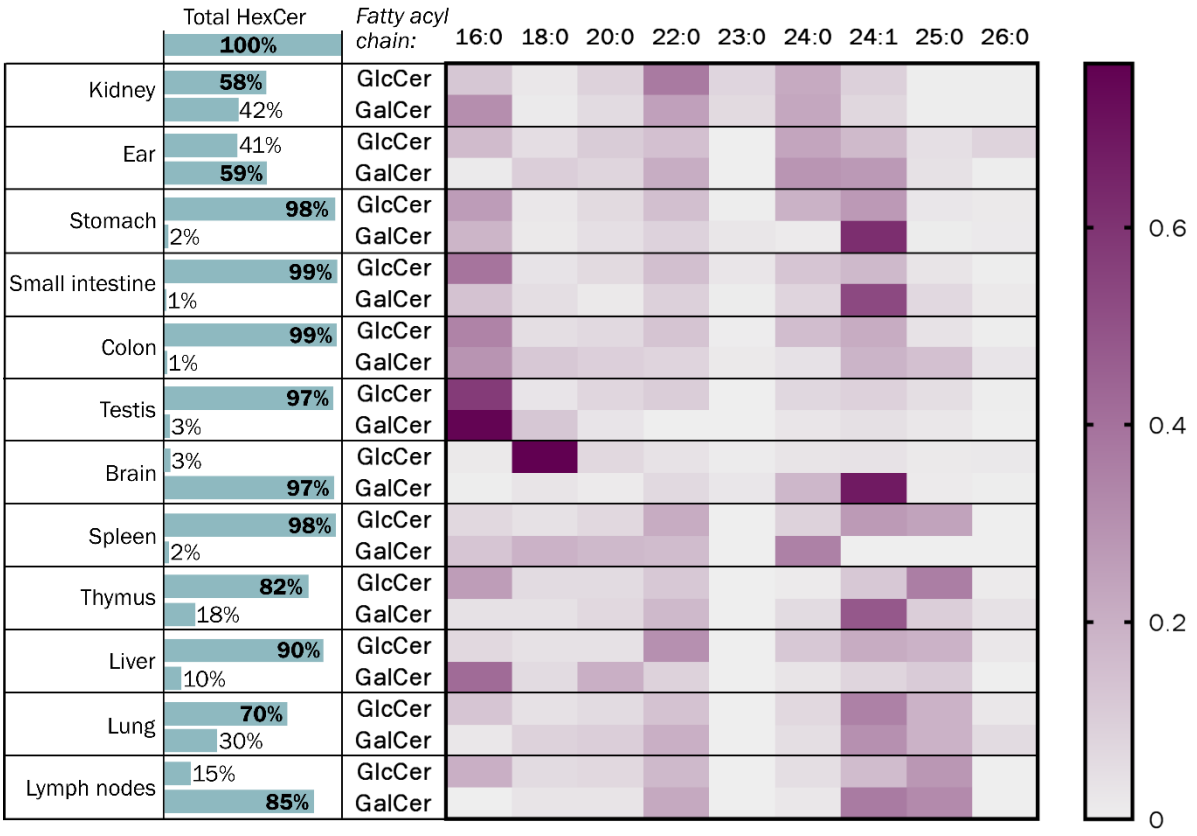

Figure 33: Relative distribution of β-GlcCer and β-GalCer in various mouse organs. NS-, AS-, NP-, and AP-HexCers were determined, which contained a C18-sphingoid base and N-bound fatty acids with the chain length C16 up to C26 (as annotated). Special structures with ultra-long acyl chains as they occur in epidermis (ultra-long omega hydroxyl fatty acids) or in male germ cells (ultra-long polyunsaturated fatty acids) as well as with different sphingoid bases (e.g., C20-sphingosine in brain or kidney papillae or C17-sphingosine in epidermis) were not considered in this study. Note, nervonic acid is mainly incorporated into brain cerebrosides, whereas corresponding glucocerebrosides are enriched in stearic acid, which is the typical acyl chain of neuronal gangliosides [167].

Glucosylceramidase beta 2 (*Gba2*) catalyzes the hydrolysis of β-GlcCer to glucose and ceramide at the cytosolic side of intracellular membranes [184]. Mice lacking Gba2-activity were reported with 2-3fold increased levels of β-GlcCer in liver [92,185]. Analysis of Hexosylceramides from liver, kidney and intestine of WT and Gba2-deficient mice revealed specifically β-GlcCers to increase in Gba2-deficient mice, but not corresponding β-GalCers (Figure 34). Interestingly, the increase of intestinal β-GlcCers was restricted to the rather minor NS-type, whereas AS-, NP-, and the dominant AP-type of β-GlcCers was not affected. Furthermore, HILIC-MS^2 signals corresponding to β-GlcCer, but not to β-GalCers, were significantly reduced in liver and kidney samples of mice with a hepatocyte-specific and renal proximal tubulus-specific deficiency of the glucosylceramide synthase (*Ugcgf/fAlbCre* and *Ugcgf/fPax8Cre*), respectively (Figure 34

A and D). However, mainly NS-type β-GlcCer were decreased and AS-type β-GlcCer even increased value in hepatocyte-Ugcg-deficient liver samples. Vice versa, β-GalCer accumulated more than 10fold in kidneys of CST-deficient mice due to a block in further conversion to sulfatides (Figure 34 D). Here, β-GlcCer concentrations did not change. Likewise, analysis of male kidney cortex samples from globotriaosylceramide synthase (Gb3S, A4galt)-deficient mice revealed a more than twofold increase of β-GalCers, which was almost exclusively due to an increase of NS-type cerebrosides (Figure 34 E). Levels of β-GlcCers were not affected by this model, too. All together, these data supported the correct association of chromatographic peaks to cerebrosides (β-GalCers) and glucocerebrosides (β-GlcCers), respectively.

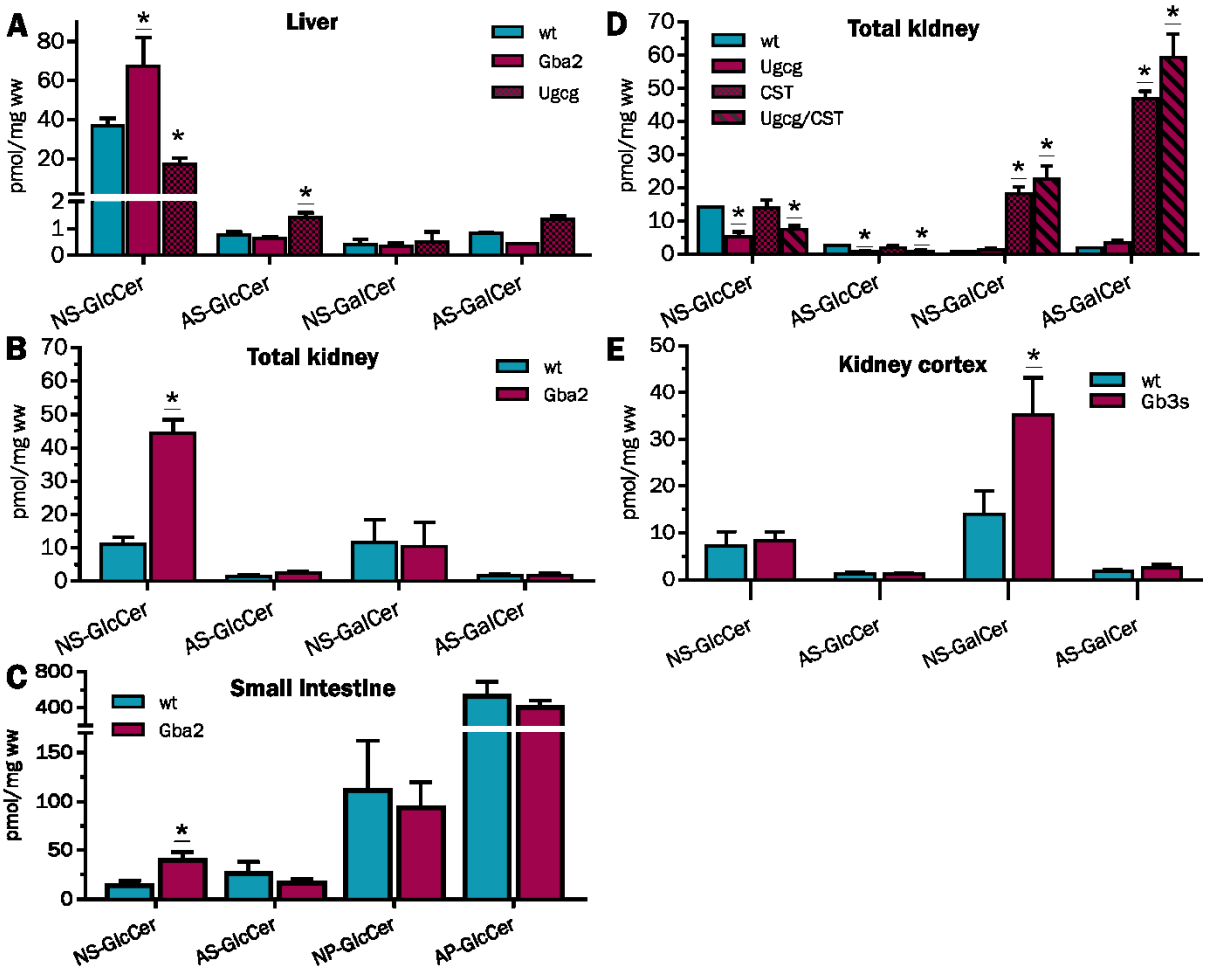

Figure 34: HILIC-MS²-based quantification of β-GlcCers and β- GalCers in liver of WT, Gba2$^{-/-}$, and Ugcgf/fAlbCre mice (A); kidney of WT and Gba2$^{-/-}$ mice (B); small intestine of WT, and Gba2$^{-/-}$ mice (C); kidney of WT, Ugcgf/fPax8Cre, CSTf/fPax8Cre, (Ugcg and CST)f/fPax8Cre mice (D); and in kidney cortex of WT and Gb3s$^{-/-}$ mice. Note the specific increase of NS-β-GlcCer in liver, kidney and small intestine of Gba2$^{-/-}$ mice, the selective decrease of NS-GlcCer in liver and of NS- and AS-GlcCer in kidney of Ugcgf/fAlbCre and Ugcgf/fPax8Cre [and (Ugcg and CST)f/fPax8Cre] mice, respectively (E). Vice versa, NS- and AS-β-GalCer accumulates in kidneys with CST-deficiency [CSTf/fPax8Cre and (Ugcg and CST)f/fPax8Cre] as well as NS-β-GalCer in cortex of Gb3s$^{-/-}$ mice. n = 3, except for (D) WT = 1 [167].

3.5.3 Separation of HexCers with different types of hydroxylation

Cerebrosides from brain are enriched in cerebrosides of the AS-type [186]. They contain 2R-hydroxy fatty acids[187] and depend on fatty acid 2-hydoxylase (*Fa2h*)[163,188], which specifically incorporates acyl chains with an α-hydroxy group in R-configuration [189]. Here the retention times of AS-type cerebrosides with corresponding synthetic standards containing a 2-hydroxyacyl chain with either R- or S-OH stereochemistry were compared. The β-GalCer standard with a 2R-hydroxy-stearoyl chain separated from the corresponding compound with 2S-hydroxy configuration and eluted together with corresponding AS-type cerebrosides from murine brain about 0.38±0.02 min later than the 2S-isomer (Figure 35). By that cerebrosides with 2S-hydroxy fatty acids elute significantly earlier (-0.27±0.02 min) than AS-type glucocerebrosides (β-GlcCer) with 2R-configuration at the α-hydroxy group and thus can be distinguished by this HILIC-method. In contrast to brain, stomach contains AS-type β-GlcCer. Normal levels depend on synthesis by *Fa2h* and loss of corresponding enzyme reduces the signal to about one tenth (Figure 35). Due to the specificity of the enzyme [189], this dependence implies the α-hydroxy acyl group of AS-β-GlcCers from stomach to be of 2R-configuration.

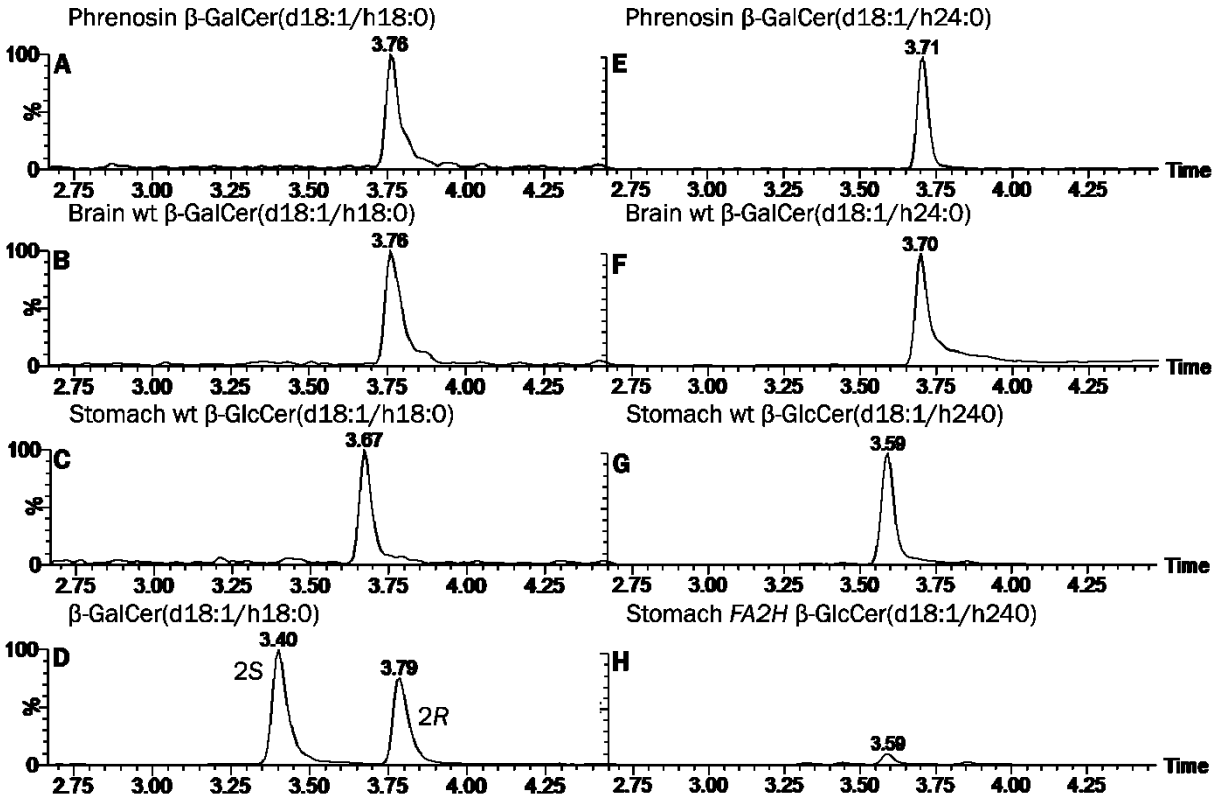

Figure 35: HILIC-MS²-based separation of AS-type β-GalCers with 2R- and 2S-hydroxy stearic acid. Extracted ion chromatogram (EIC) for AS-HexCer(d18:1/h18:0) and (d18:1/h24:0) from a purified mixture of brain AS-type β-GalCers [phrenosin (A, E)], the synthetic standards β-GalCer[d18:1/(2S)h18:0] and β-GalCer[d18:1/(2R)h18:0] (D), a mouse brain lipid extract enriched in neutral GSLs (B, F), and a stomach lipid extract from WT (C, G) and Fa2h$^{-/-}$

(H) mice. The intensity in (H) is normalized to that of the corresponding WT signal in (G). In compliance with a report that AS-type β-GalCer from brain contain 2R-hydroxy fatty acids, the AS-HexCer(d18:1/h18:0) from phrenosin and from mouse brain migrate together with the β-GalCer[d18:1/(2R)h18:0] standard. Note, the decrease of β-GalCer(d18:1/h24:0) with 2R-hydroxy configuration in Fa2h$^{-/-}$ stomach [167].

3.6 Hexosylceramide composition in mouse models of GM2 gangliosidosis and neuraminidase deficiency

The neurological phenotype in mice containing gene defects of HexA, Neu3 and Neu4 included reports of neurodegeneration, neuroinflammation and demyelination [85,89,102]. Cerebrosides or GalCer are found in high amounts in myelin sheath and oligodendrocytes of mouse brains and should be changed in case of demyelination and neuroinflammation. The role of glucocerebroside or GlcCer is mostly restricted as the base for ganglioside biosynthesis in the brain. Therefore it exists only in small amounts due to a high turn-over rate. Mouse brain lipid extracts enriched in neutral glycosphingolipids of WT mice as well as HexA$^{-/-}$, GM2AP$^{-/-}$, Neu3$^{-/-}$ and Neu4$^{-/-}$ mice were analyzed for their β-hexosylceramide composition using the newly developed HILIC-MS/MS approach described in the previous chapter. β-GalCer of NS-, AS- and NdS-type were found, whereby only NS-type β-GlcCer could be detected (Figure 36). Amounts of detected β-GlcCer corresponded to approximately 1% of total β-HexCer signal intensity in WT mice sent from the Turkish collaboration partner, which is in correlation with previous results of WT brain analysis (Figure 33). The results revealed significantly increased β-GlcCer levels in Neu3$^{-/-}$HexA$^{-/-}$ mice (Figure 36 A), whereby increased β-GlcCer in HexA$^{-/-}$, Neu4$^{-/-}$HexA$^{-/-}$, and GM2AP$^{-/-}$ mice was statistically not significant (Figure 36 B). Decreasing amounts of β-GalCer compared to WT mouse tissue could not be detected in any group analyzed as expected due to demyelination. However, significantly diminished β-GalCer levels for Neu4$^{-/-}$HexA$^{-/-}$ and GM2AP$^{-/-}$ mice in relation to HexA$^{-/-}$ were displayed (Figure 36 B).

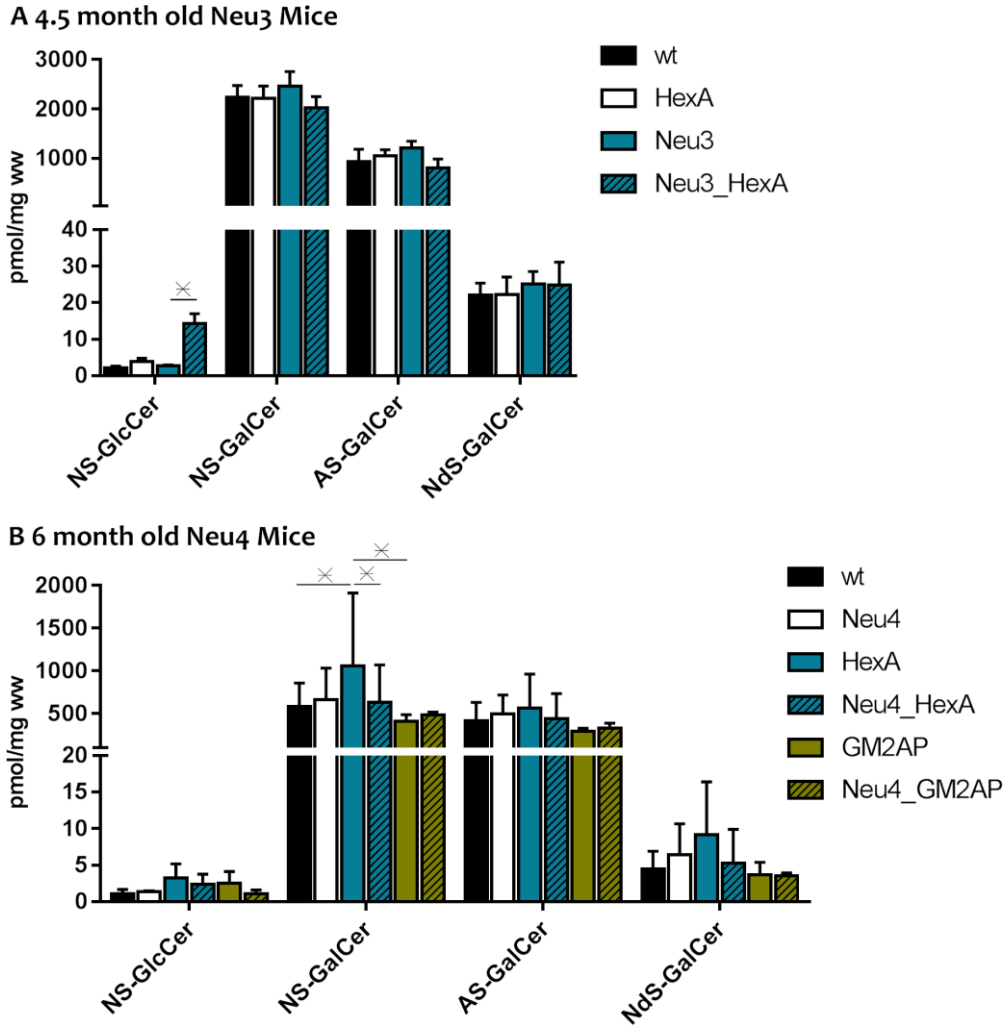

Figure 36: HILIC-MS² based separation of NS- and AS-type β-GlcCer and β-GalCer in mouse brain lipid extracts enriched in neutral GSLs of WT, GM2 gangliosidosis and neuraminidase deficiency. The intensities are normalized to the corresponding WT intensity (fold change). Black and roughly crossed bars corresponding to Neu4 and GM2AP represent sample sets with n=4 and fine crossed bars to Neu3 sample set with n=2. Two-Way Anova

3.7 Hexosylceramides in the context of T cell immune response

The analysis of hexosylceramides in various mouse tissue (Figure 33) revealed higher amounts of galactosylceramide (GalCer) in tissues of the immune system such as thymus, lung and lymph nodes that were quite unexpected. More detailed analysis of recent literature[119,124,190] showed that especially α-GalCer is a potent stimulator of invariant natural killer T (iNKT) cells, which develop and mature in thymus. Mammals produce β-GlcCer and β-GalCer, in contrast *bacteroides fragilis*, a member of the human gut microbiome, and the marine sponge *agelas mauritianus* produce α-GalCer [13]. Enzymes catalyzing the production of corresponding α-anomers in mammals have not been described so far. It only has been proposed that at very low levels α-GalCer is endogenously present and necessary for invariant natural killer T cell (iNKT cell) homeostasis [165].

3.7.1 α-GalCer in members of the human gut microbiome

B. fragilis has been reported to produce ceramides and α-GalCer containing an iso- or anteiso-branched C17, C18, and C19-sphinganin and a β(R)-hydroxylated and isobranched C17-fatty acid [14,191]. Here, α-GalCers from *B. fragilis* eluted 0.03 min before our calculated retention times (t_R = 4.00 - 4.03 min) for corresponding AS-type α-GalCers, but definitely beyond AS-type β-GalCers (t_R = 3.92 – 3.95 min, Δ = 0.05-0.06 min). This slight forward shift may be due to the hydroxy group of the acyl chain, which is for *B. fragilis* in 3(β)- but not in 2(α)-position of the fatty acid as well as the saturated sphingoid base (dS). This shift was consistent for all three compounds reported by B. fragilis (Figure 37 A and B). In addition to *B. fragilis*, lipid extracts of nine further bacteria of the human gut microbiome were analyzed. In *Prevotella copri* and *Bacteroides vulgatus* the identical HexCer peaks as for the BdS-type α-GalCers of *B. fragilis* (Figure 37 C) were detected. Overall levels of these compounds were at least 100fold lower than in *B. fragilis*. The other 7 species investigated did not contain quantifiable amounts of α-GalCer. Nevertheless, *B. ovatus*, *B. thetaiotaomicron*, and *B. caccae*, contained signals for α-GalCers, which were above the LOD in both, the HILIC and the RPLC method (Appendix V).

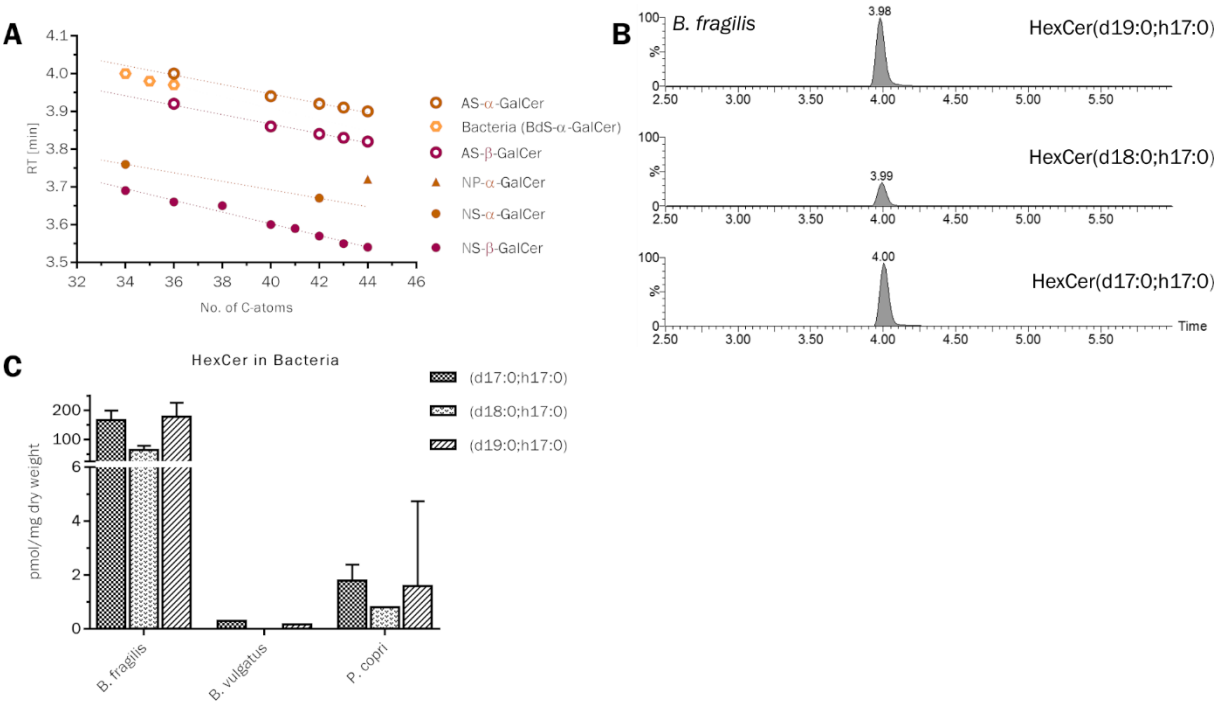

Figure 37: HILIC-MS²-based detection of α-GalCers from Bacteroides fragilis and identification of equivalent compounds in Bacteroides vulgatus and Prevotella copri. A) Comparison of the determined retention times of α-GalCers from B. fragilis with those of synthetic α-GalCer and β-GalCer standards and predicted values for AS-type α-GalCers. B) Extracted ion chromatograms for individual HexCer from B.fragilis. C) Quantification of the three α-GalCers in B. fragilis, B. vulgatus and P. copri. Note the 100fold amount of α-GalCers in B. fragilis. n = 3 [167].

3.7.2 Hexosylceramide detection in the mouse digestive tract by HILIC-MS/MS

Bacteroides fragilis is a member of the human gut microbiome, which is associated with colorectal cancer, metabolic syndrome and diarrhoea. *Bacteroides* strains were found to be the prominent genus (20-40%) in the mouse intestinal tract [133,137,192]. The developed HILIC-MS^2 method was used to analyze hexosylceramide composition in compartments of the mouse digestive tract from duodenum across jejunum, caecum and colon to the feces of WT Bl6 and axenic NMRI mice. β-GlcCer was the most abundant hexosylceramide and found to decrease from duodenum to feces in both Bl6 and NMRI mice. In contrast β-GalCer amounts increased from duodenum to feces, but displayed only 1-10% of the found hexosylceramides. Interestingly, small amounts of a predicted BdS-α-GalCer with a d18:0;h16:0 ceramide anchor were found, which eluted at the same retention time as the previously described α-GalCer(d17:0;h17:0) from *B. fragilis*. These predicted BdS-α-GalCer showed the same increasing signal pattern as β-GalCer and was not detected in bacteria-free (axenic) NMRI mouse caecum in contrast to the WT Bl6 caecum (Figure 38).

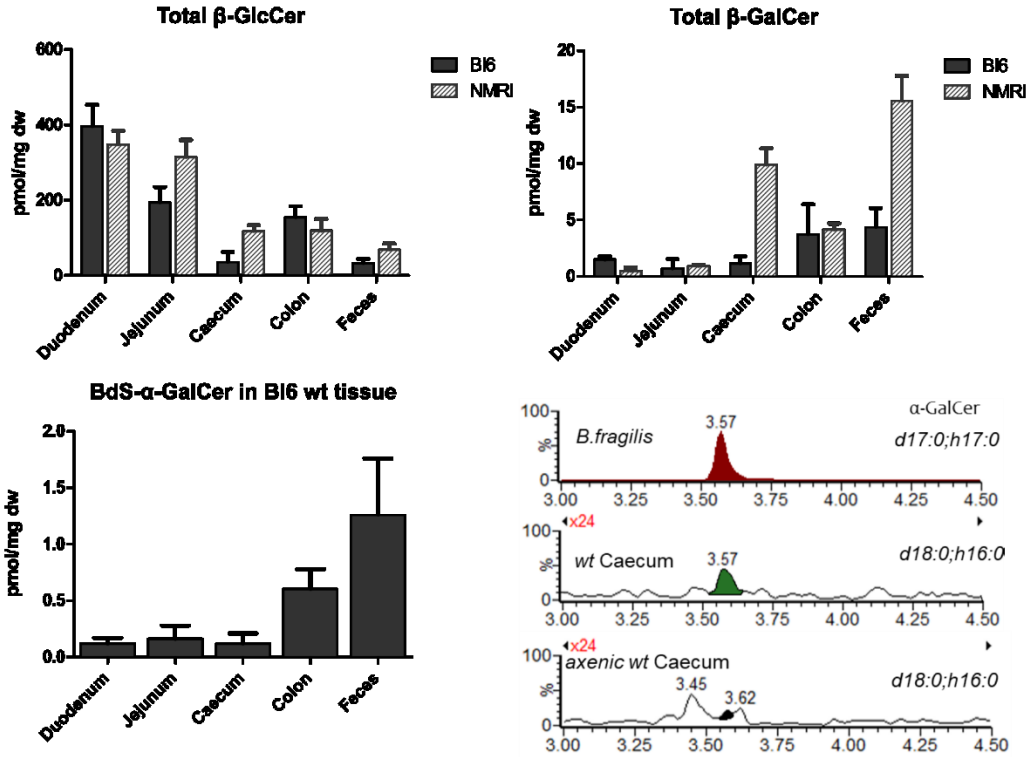

Figure 38: HILIC-MS^2 based analysis of WT Bl6 and axenic NMRI mouse intestinal tract. A) Total β-GlcCer amounts in digestive tract compartments of duodenum, jejunum, caecum, colon and feces. B) Total β-GalCer amounts in mouse intestinal tract. C) Predicted AdS-α-GalCer found in mouse digestive tract and D) extracted ion chromatogram for α-GalCer from B. fragilis compared to predicted α-GalCer from mouse caecum and missing peek from axenic mouse caecum sample. n=3

Next, fresh prepared tissue samples were either not treated at all or washed with PBS, and the washed-out content collected to investigate whether the detected BdS-α-GalCer may be connected to the epithelial cells of the intestinal tissue (washed) or the gut microbiome (content). Results showed that β-GlcCer and β-GalCer were both enhanced in PBS washed tissues compared to non-treated tissue and that the predicted BdS-α-GalCer is unchanged in the PBS washed tissue of jejunum, caecum and colon (Figure 39). The analyzed content displayed increased levels of BdS-α-GalCer for jejunum, caecum and colon, which could indicate bacterial origin. Nevertheless, β-GlcCer and β-GalCer amounts were as well increased in the content jejunum, caecum and colon and therefore the question of mammalian or bacterial HexCer origin remains open (Figure 39).

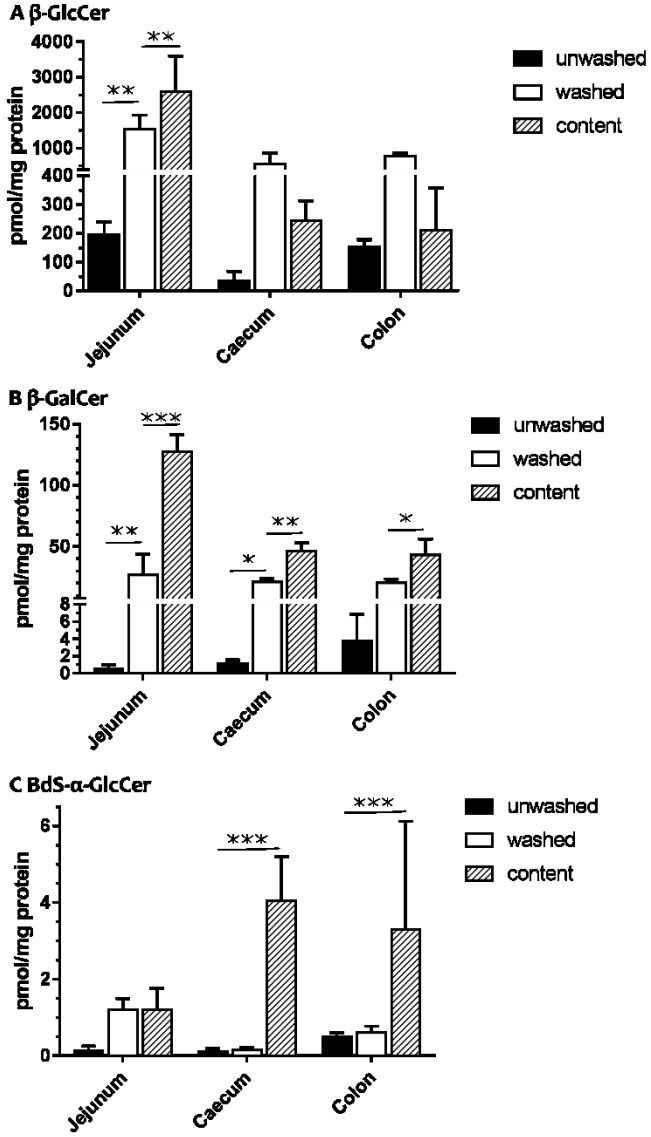

Figure 39: HILIC-MS² based analysis of WT Bl6 mouse intestinal tract compartments jejunum, caecum and colon of β-GlcCer (A), β-GalCer (B) and predicted BdS-α-GalCer (C). Not treated tissue samples, PBS washed tissue samples and washed-out content were compared to investigate mammalian or bacterial origin of HexCers. Two-way Anova, n=3

3.7.3 Hexosylceramide quantification in caecum and feces from WT mice under high fat diet conditions

Bacteroides in the mouse gut microbiome were reported to decrease under high fat diet conditions and obesity models [139]. *B.fragilis* as a member of the human gut microbiome produces α-GalCer. The detected and predicted BdS-α-GalCer could be produced by a type of Bacteroides in the mouse gut microbiome and should therefore decrease under high fat diet conditions. Mouse tissue samples were collected from an experimental set up of Dr. Silke Herzer from our department and prepared as described in material and methods (2.2.1). Hexosylceramides were analyzed by HILIC-MS/MS and detected types of HexCer were added up to total amounts of β-GlcCer, β-GalCer and BdS-α-GalCer. Mice were fed twice a day (morning /evening) with either 200 µL PBS, olive oil, milk fat Ghee or high fat diet (HFD) for five days. The different composition and type of fatty acids within the mentioned oil, fat and diet should lead to different effects on mice tissue [193]. HexCer-analysis revealed BdS-α-GalCer indeed to decrease in samples of mice fed with HFD, but other detected hexosylceramides decreased as well. Milk fat (Ghee) and olive oil diets did not induce significant changes of any HexCer group monitored. However significant values for all groups were detected under HFD (Figure 40).

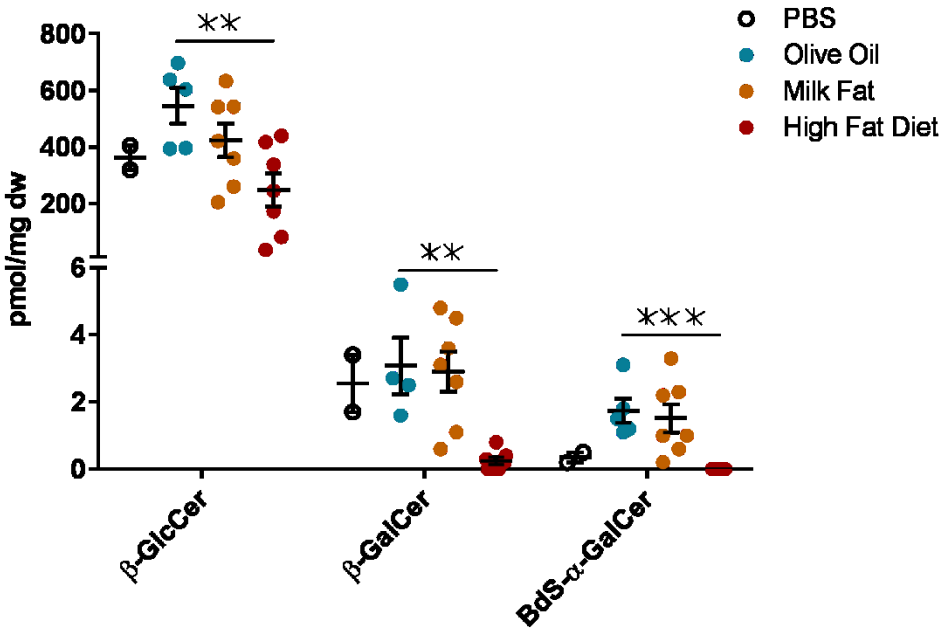

Figure 40: HILIC-MS² based analysis of hexosylceramides in lipid extracts from caecum of mice fed for 5 days twice a day with either 100 µL PBS, Olive oil, or milk fat (Ghee) in addition to chow diet or high fat diet. PBS n=2, olive oil, Ghee and HFD n≥3. Note the tendency of all detected hexosylceramide species to diminished amounts under high fat diet. Two-Way Anova.

4 Discussion

4.1 Brain ganglioside analysis is based on a HILIC-MS^2 method

Ganglioside (GG) analysis with LC-MS/MS can be based either on reversed phase (RP18) or HILIC chromatography, separating amphiphilic GG regarding their lipid moiety or glycan head group respectively. Additionally, GG ions can be detected in either positive or negative ion mode, whereby due to their sialic acid group in the glycan structure GGs naturally are deprotonated at physiological pH. The standard sphingolipid analysis in our laboratory previously was performed with RP18-MS/MS mainly in the positive mode as the ion sensitivity in positive mode has been shown to be better as in the negative mode, and RP18 based chromatography allowed time saving gradients with short re-equilibrium phases. The first attempt of this work was to test the feasibility of positive ion mode detection and RP18 chromatography by comparing it with negative ion mode and HILIC chromatography. Parameter decreasing ion sensitivity such as in-source decay (ISD) and adduct ion formation were tested with single-injected GG standards. Both ISD and ammonium adduct formation showed a tendency to increase with complexity of the GG, illustrating on the one hand the need for chromatographic baseline separation. On the other hand, monitoring the additional adduct ion formation increased the transitions necessary for GG detection and therefore reduces the number of different GGs that could be measured per one gradient run. Additionally, the existence of a protonated ion, a water-loss ion and an ammonium adduct ion decreased the total sensitivity per GG. In the negative ion mode the overall sensitivity was not as high as in the positive mode, however neither ISD nor adduct ion formation could be detected. The evaluation of the optimized source temperature and capillary voltage for ion generation in the ESI spray revealed no improvement for the positive ion mode such as adduct ion reduction. Adduct ion formation driven by salt additives such as lithium, sodium and ammonium were shown to enhance detection in ESI-MS/MS [194,195], and in analogy it was hypothesized that diethylenetriamine (DETA) with its three C_2-spaced amine groups could complex the carboxylate group of sialic acid by that both shifting (+)ESI ion formation towards the DETA-adduct and simultaneously enhancing the overall sensitivity for positive ion formation. Indeed, mass spectra generated by direct injection in the presence of DETA showed positive ions with more than 90% DETA adduct formation compared to less than 10% of protonated ions and no detectable sodium or potassium adducts. Unfortunately, the concentration of 10 mM DETA was so high that the surplus of DETA formed a yellow mist in the spray chamber. Derivatization of the GG glycan structure to transform the carboxylate group into a neutral or basic group

instead of adduct formation might rather be a necessary step to enhance sensitivity in (+)ESI as shown for per-*O*-benzoyl, permethyl and peracetyl derivatives of glycosphingolipids in combination with liquid chromatography [196–201].

RP18-based chromatography was tested for its limits to separate GGs with identical ceramide anchors as the use of methanol in the gradient system could be beneficial for ionization efficacy and gradient run times are short. The most promising combination of UPLC column and solvent system was the HSS PFP column, which is not a classical RP18 phase but based on a pentafluorophenyl phase, and an acetonitrile/water versus acetonitrile/2-propanol solvent system without methanol. Nevertheless, this system failed to separate the mono-sialic gangliosides GM2 and GM1 completely (50%) and showed even less separation efficacy for the more complex GGs. Consequently, a HILIC-based chromatography was developed and different solvent additives tested, whereby ammonium acetate showed the highest ionization efficacy in negative ion mode. The use of methanol in the HILIC gradient resulted in unidentified “ghost peaks” and peak widening, therefore an acetonitrile versus water solvent system was established. The final method for the analysis of GGs thus resulted in a HILIC-MS^2 method with negative ion detection similar to the already published gradients as no tested improvement of positive ion mode and RP18-based chromatography could overthrow their drawbacks regarding GG analysis. Finally, sample preparation was advanced revealing that for mouse brain samples initial anion exchange chromatography (DEAE) of the raw extract followed by saponification and desalination showed the highest overall response for GGs. Saponification as well as anion exchange chromatography by DEAE increased subsequent GG detection by reducing quenching effects due to other lipids like phospholipids, free fatty acids or cholesterol. Phospholipids are destroyed by saponification, however release free fatty acids, which would elute together with GG in the anionic lipid fraction upon anion exchange chromatography. Therefore, initial DEAE-fractionation reduced the load of phospholipids giving later rise to free fatty acids and improved final response for GG. Since the order of methods was significant, as starting with saponification and processing with DEAE afterwards decreased sensitivity, it demonstrated that fatty acids released from phospholipid saponification would be found in the acidic fraction of the gangliosides and quenched detection of GGs.

4.2 Neuraminidase 3 and 4 show overlapping but also distinct substrate processing

Tay-Sachs disease describes an autosomal-recessive genetic dysfunction of hexosaminidase A (HexA) which results in the severe lysosomal storage of ganglioside GM2 and early lethality for humans with the infantile on-set form. To date there is no effective treatment beyond palliative care despite fifty years of research including treatment approaches such as gene therapy, inhibitors, cord blood transplant, chaperone therapy, stem cell therapy and enzyme replacement therapy [70,96–100]. In mouse models of HexA deficiency only moderate GM2 accumulation was found, as well as no significant neuronal phenotype. Neuraminidases were investigated as possible bypass enzymes for the degradation of GM2 and a new opportunity for therapeutically approaches in humans [85,88,202]. Determining the specific substrates of neuraminidase 3 and 4 for mouse brain gangliosides (GG) *in vivo* is an essential step investigating the significance on the GM2 degradation bypass for each neuraminidase and for the significance to further drug developments. In this study, GG processing by neuraminidase 4 (Neu4) was examined by analyzing mouse brains with deficiency in Neu4 combined with the GG-synthesis enzymes *Galgt1*$^{-/-}$, *GM3S*$^{-/-}$ and *GD3S*$^{-/-}$ as well as the GM2 activator protein *GM2AP*$^{-/-}$ in the background of WT Bl6 or Tay-Sachs disease (*HexA*$^{-/-}$) mice. Analysis was performed with HILIC-MS^2 for the GGs and RP18-MS^2 for the neutral glycosphingolipid metabolites of the brain GGs. The results revealed that Neu4 depletion led to decreased ratios of GM1/GA1, which had been published previously [89,102]. However, Neu4 deficiency resulted in addition in higher ratios of GD1a/GM1, GM3/LacCer and GD3/GM3, and maybe GD1c or GD1α/GM1b, but not GM2/GA2. Whereby the impact of Neu4 loss was highest for the ratio of GM1/GA1 followed by that of GM3/LacCer. A convenient explanation for these results would be the involvement of Neu4 in GD1a and GM3 degradation, which would be in line with the decreased GM1 and increased GD1 levels as well as the increased GM3 and decreased LacCer levels. Similar analysis were performed in Neuraminidase 3 (Neu3) depleted mice which are crossbred with *HexA*$^{-/-}$ mice of Tay-Sachs disease mouse model. Neu4 and Neu3 enzymes were hypothesized to have similar substrate specificity due to *in situ* experiments [75]. Nevertheless, Neu3 showed increased GM2, GM3, GA2 and LacCer levels, but no impact on GM1 and GA1 levels. These results were published in Seyrantepe,..., von Gerichten *et al.* (2018) [85]. The results indicated Neu3 as the main actor in GM2 bypass reaction for Tay-Sachs disease in mice. Targeting Neu3 (or Neu4) as a therapeutically indication could lead to an overall changed GG pattern in the brain, but not only to a decreased

GM2 accumulation. GM3 was shown to inhibit EGF-induced autophosphorylation and reduced GM3 levels due to enhanced NEU3 expression could vice versa induce EGF phosphorylation which is correlated with human cancers [24,203,204]. Furthermore, the increase of GM3 levels could also originate in astrogliosis, or other immune cells activation in the detected neuroinflammation such as phagocytes, found in brains with Neu3 (Neu4) deficiency [85,89]. A future perspective for the research of Neu3/Neu4 involvement in the brain would be a gene rescue performed in mouse neurons or mouse brain with the human NEU3/NEU4 genes. This would answer the question, whether the human Neu3/Neu4 could bypass principally the TSD-block *in vivo*, a prerequisite to be targets of TSD treatment.

The decrease of GM1 due to Neu4 depletion was hypothesized to be caused as secondary effect by the demyelination in Neu4$^{-/-}$ mouse brains [89], which lead to the hypothesis that galactosylceramide (GalCer) as another glycosphingolipid involved in the myelin sheaths should be decreased, too. This topic is further elaborated in chapter 4.5.

4.3 MALDI remains the common technique for Mass Spectrometry Imaging

A basic aim of this work was to establish DESI-MS/MS as a technique for mass spectrometry imaging (MSI) to analyze the spatial distribution of (storage) gangliosides (GG) on brain sections. The results revealed that, with the ion source in hands, DESI was not an adaptable tool for MSI as it failed to detect GGs in mouse brain tissue despite several attempts to enhance GG sensitivity such as washing steps and on-tissue saponification of the abundant phospholipids. Furthermore, it occurred that the reproducibility and stability of this technique was a main issue as well as the low spatial resolution. Meanwhile the investigations of this work Waters Corporation purchased the license from Prosolia for the DESI sprayer and developed the spray device for more stability and better resolution, which made GG detection also possible. The combination of DESI with ion mobility spectrometry seems to have a positive impact for GG analysis in the mouse brain [151]. The comparison of DESI-MS/MS with the commonly used MALDI-TOF MSI discovered that MALDI showed better stability and sensitivity, if the brain tissue had been washed prior to analysis. Furthermore, MALDI-MSI provided a higher spatial resolution. The potential advantage of faster screening by DESI in connection with a triple-quadrupole instrument was bested by the development of the Bruker Rapiflex MALDI Tissuetyper TOF MS instrument, which demonstrates high-speed acquisition of tissue samples [205].

4.4 MSI reveals local neural GM2 accumulations similar for Neuraminidase 3 and 4 deficiencies on a Tay-Sachs disease background

Brain slices of mouse tissues with knockouts for neuraminidase 3 (Neu3) and 4 (Neu4) in combination with Tay-Sachs disease (*HexA*$^{-/-}$) were analyzed with MALDI-TOF mass spectrometry imaging and displayed a similar GM2 accumulation in hippocampus, hypothalamus, cortex, cerebellum and olfactory bulb. Whereby Neu4 revealed a sharply framed GM2 pattern in the GM2 gangliosidosis brains compared to the more diffuse GM2 signal in Neu3 deficient mouse brains. Additionally, fine structures that may be correlated to the area of corpus calosum were GM2-positive in Neu4 depleted brain slices, but not in Neu3 depleted. The results are in common with already published data localizing Neu3 expression abundantly in the cerebellum [206] and detecting GM2 as well as GM3 accumulation with antibodies against Neu3, GM2 and GM3 in the hippocampus and cortex [85,89,102]. A more detailed analysis of GM2 and GM1 signals in the images revealed that GM2 accumulation in the hippocampus and cortex is specifically increased due to Neu4 deficiency. The similar patterns in spatial neural GM2 accumulation for Neu3 and Neu4 deficiency in TSD models suggest a rather broad distribution of both sialidases, but dependency of GM2 accumulation on local GG turnover. A severe impact for the data generated would be the combination of MALDI MSI and other imaging techniques such as immunohistochemistry and *in situ* hybridization to proof the localization of Neu3 and Neu4 in neurons to directly correlate with GM2 turnover. Additionally, cell specific expression of Neu3/Neu4 and GM2 accumulation in the mouse brain (or human) could be further reviewed. Antibodies against distinct neural cell types such as mature neurons, astrocytes and microglia combined with in situ hybridization of Neu3/Neu4 could locate neuraminidase expression *in vivo*. Immune cell expression of neuraminidase may have an impact on disease therapy. Similar questions would be answered by using cell-specific knockouts for Neu3 (Neu4) for example by generating GFAP-Cre, CX3CR1-Cre or CamKII-Cre mice to target astrocytes, microglia or forebrain neurons in the background of Tay-Sachs disease.

4.5 Selective Analysis of diastereomeric hexosylceramides based on HILIC-MS^2 and proof of principle

Lipidomics is a fast growing field of interest impacting more and more medical research. Often all-in-one analysis is demanded and high throughput methods like direct infusion into high resolution mass spectrometers with MS^{all}-scans and subsequent data processing software try to fulfil these requests [207–209]. These MS-only techniques, however have their limitations and for example do not distinguish stereoisomeric compounds with qualitatively identical fragmentation behaviors. Separation and quantification of such stereoisomers therefore requires combination of MS with orthogonal methods, such as chromatography or ion mobility. LC, especially, is a wide-spread technique, often coupled to MS to increase specificity and sensitivity of detection. Here, a HILIC-based method is presented, which enables the separation of α- and β-anomers of GlcCer and GalCer comprising identical Cer anchors, which was not achieved with reversed phase LC. Diasteromeric HexCers are amphipathic molecules with their structural differences buried in the polar head group, but not the hydrophobic ceramide anchor, the latter interacting with the stationary phase in reversed phase LC and the former in HILIC. Coupling to MS^2 allows to identify differences in Cer anchor composition to unambiguously ascribe NS-, AS-, NP-, and AP-type HexCer-derived HILIC-peaks of biological samples according to their retention times to either GlcCer or GalCer with either α- or β-glycosidic linkage. The method can be used to analyze complex biological lipid extracts, as demonstrated by the application to various mouse organs and bacteria [167]. The correct assignment of peaks was supported by measuring a selective increase or decrease of β-GlcCer over β-GalCer in various tissues with GBA2 or UGCG deficiencies, respectively. Loss of GBA2 activity leads to the accumulation of the substrate β-GlcCer. In contrast, the lack of UGCG activity either in hepatocytes or in renal tubular cells omitted corresponding production of β-GlcCer, thereby reducing the overall β-GlcCer concentration of liver or kidney, as expected [33,35,92,210,211]. Further confirmation was obtained by detecting a selective increase of β-GalCer over β-GlcCer in organs lacking activity of either CST or Gb3S, for both of which β-GalCer is the substrate to produce either sulfatide SM4s or galabiaosylceramide, respectively [35,46,212]. Interestingly, however, the levels of not all β-GlcCer species went up with Gba2-deficiency and the levels of AS-type β-GlcCers remained unchanged. There are two possible explanations, which are: i) GBA2 may not be expressed in cells that express the AS-type; or ii) the AS-type β-GlcCer resides in lipid layers with no access to the cytosolic activity of GBA2. Whereas loss of UGCG activity in renal tubular epithelial cells caused a decrease of NS- and AS-type β-GlcCers in kidney, the hepatocyte-specific loss of UGCG activity, causing NS-types to go

down, even led to an increase of minor AS-type β-GlcCers. Because tissues are multi cell-type structures, the loss of enzyme activity in one specific cell type will always lead only to a loss of product in this but not the other cell types of the organ and thus not to a complete disappearance in organ extracts, if this product is synthesized by several cell types of the respective organ. An increase of a subspecies may imply either an increased relative abundance of the corresponding synthesizing cell type in mutant tissue or a reactive increased production or decreased catabolism of these compounds within the corresponding cells. The here established HILIC-MS^2 method on top separates AS-type cerebrosides containing the α-hydroxy group of the acyl chain either in 2*R*- or 2*S*-configuration, which has to be taken into account when analyzing biological samples. Both configurations may appear in biological samples and AS-type cerebrosides of the brain were reported to contain basically the 2*R*-configuration [187], which was confirmed here with this HILIC-MS^2 method. Screening different mouse tissues with this method, we further confirmed high abundance of cerebrosides in brain and kidney, whereas most other tissues, including liver and spleen, are dominated by the presence of glucocerebrosides. Two exceptions were identified: auricles and especially lymph nodes are relatively abundant in cerebrosides, as compared to glucocerebrosides, and further investigations need to address from which cell types they origin. As this method delivers data for individual species, it allows to detect differences in ceramide anchor compositions between cerebrosides and glucocerebrosides or to follow changes in these compositions upon aging, activation, or disease progression. Here we plotted the relative acyl chain length distributions of cerebrosides against those of glucocerebrosides found in wild type mouse tissues. As expected, brain cerebrosides are rich in nervonic acid, a major component of myelin sheaths [186,213]. In contrast, the small amount of brain glucocerebrosides is synthesized by majority with stearic acid. This points to neuronal cell origin as these cells convert this compound to complex gangliosides such as GM1a, GD1a, GD1b, or GT1b, all of which are known to basically contain stearic acid in their lipid anchor [186,214]. Likewise, nervonic acid was the major fatty acid incorporated into cerebrosides of colon, small intestine, thymus and lymph nodes, whereas glucocerebrosides of these organs were enriched with the shorter palmitic acid. In conclusion this points to different cell types or differentiation stages of cells forming either cerebrosides or glucocerebrosides and expressing different pattern of ceramide synthases, which remains to be investigated.

4.6 Levels of β-GlcCer and β-GalCer in brain of TSD models

The decrease of GM1 due to Neu4 depletion (4.4) was hypothesized to be caused as secondary effect by the demyelination in Neu4$^{-/-}$ mouse brains [89], which lead to the hypothesis that β-GalCer, the major lipid in myelin sheaths (30% of myelin lipids), should be decreased, too. Analysis of neutral brain extracts from mice with either Neu3 or Neu4 deficiency in the background of Tay-Sachs disease revealed, however, no changes in β-GalCer levels until the age of 6 month. A trend for reduced β-GalCer levels was detected only in mouse brains with *GM2AP*$^{-/-}$ and *Neu4*$^{-/-}$*GM2AP*$^{-/-}$ genotype. On the other hand, defective GG-catabolism could affect the homestatic levels of β-GlcCer, which is an intermediate in GG-synthesis and degradation. Interestingly, β-GlcCer levels increased in HexA$^{-/-}$ mouse brains, an effect even more pronounced in the *Neu3*$^{-/-}$*HexA*$^{-/-}$ genotype. One explanation may be that the severe amount of GM2 lysosomal storage can lead to co-precipitation/trapping of other glycosphingolipids such as β-GlcCer in the lamellar lipid sheets accumulating in neuronal lysosomes [4].

4.7 α-Galactosylceramide, most potent stimulator of invariant natural killer T cells (iNKT cells) was detected in bacteria of the human gut microbiome

In contrast to the afford discussed cerebrosides and glucocerebrosides (chapter 4.6), invariant natural killer T cells are activated most effectively when recognizing galactosylceramide with an α-glycosidic linkage presented on the cell surface receptor CD1d of antigen presenting cells [215,216]. One natural bacterial source of this compound in contact with our body is *Bacteroides fragilis*, a bacterial member of the human gut microbiome [14]. Here the detection of α-GalCers from *B.fragilis* by HILIC-MS^2 with unique retention time was shown to separate from the β-glycosidic mammalian counterparts. To address if other bacteria of the human gut microbiome may also express these immune stimulatory compounds, an initial set of 10 bacteria of the human gut microbiome was analyzed. Subsequently potential changes of its levels upon intestinal inflammation were addressed in a model of colitis. In colitis, the intestinal barrier gets leaky for bacteria, which finally may lead to sepsis [133]. Here, at least 2 other bacteria of the human gut microbiome revealed quantifiable amounts of α-GalCer and further 3 strains delivered signals corresponding to α-GalCer, which were above the lower detection limit. Although concentration of α-GalCer in all these five strains was at least 100fold lower than in *B.fragilis*, the results demonstrate that there might be a remarkable high number of bacteria present in our gut, which is capable to synthesize the immunogenic α-anomeric variant of GalCer. On the other hand it should be of interest, whether the relatively high concentrations

of α-GalCer in *B. fragilis* contribute to its potential to cause diarrhea and colitis, which results in a higher risk for cancer [136,137]. The results obtained in this study underline at least the power of the method to screen for such immunogenic compounds and further support the idea that α-GalCer is a common natural CD1d-ligand for iNKT cell activation in immune host defense. Very low amounts of endogenously produced α-GalCer (and eventually α-GlcCer) have also been discussed to contribute to successive iNKT cell maturation [12]. In this context and due to lack of knowledge of mammalian α-GalCer synthases, endolysosomal catabolism of α-GalCer has been discussed to regulate levels of α-GalCer on antigen presenting cells. Cerebrosidase and glucosylceramidase are specific for β-glycosylceramides and seem not to turn over α-GalCer. Catabolism rather appears to be initiated by acidic ceramidase releasing the lyso-compound α-GalSph, which, in contrast to α-GalCer, is a substrate for α-Galactosidase (GLA). Pharmacological inhibition of either these enzymes or defective activity in Fabry disease thereby induce a pro-inflammatory phenotype of iNKT cells [12,130,217,218].

To further investigate the idea of bacterial α-GalCer originated from the gut microbiome as an alternative to endogenously synthesized, tissue samples from different parts of the mouse intestinal tract were screened for hexosylceramides. Interestingly, β-GlcCer and β-GalCer levels changed controversy from early intestine area duodenum over jejunum, caecum and colon, and finally feces in WT Bl6 and NMRI mice. β-GlcCer continuously decreased in parallel to a continuous increase of β-GalCer, changing the β-GalCer percentage from 1% of the total HexCer to 10-30% β-GalCer. These changes can contribute to a shift in cell types, the increasing amount of bacterial content or the metabolic digests of the intestine. More importantly, a potential α-GalCer was detected especially in colon and caecum of WT Bl6 mice, but not in bacteria-free (axenic) NMRI mice. The retention time is the same as the *B.fragilis* associated α-GalCer(d17:0;β-h17:0) but the transition suggests a ceramide backbone corresponding to d18:0;h16:0. As there is not much known about specific glycosphingolipid expression of mouse bacteria, further experiments were conducted to proof bacterial origin of this predicted BdS-α-GalCer. Comparison of unwashed and PBS-washed tissue as well as the washed-out content showed BdS-α-GalCer amounts are higher in unwashed tissues and content compared to the washed tissue, which supports the idea of bacterial origin. Metabolic digestion products as source of these particular BdS-α-GalCer could not be excluded. Another attempt to narrow down the source of the BdS-α-GalCer was based on reports that Bacteroides populations were decreased in the gut microbiome under high-fat diet (HFD) conditions [139,140]. The BdS-α-GalCer levels, if produced by a bacterium similar to *B.fragilis*, should therefore

decrease in the gut microbiome of mice fed with HFD. Analysis of caecum and feces from mice fed five days with a high-fat diet showed indeed decreased levels of the predicted BdS-α-GalCer. The amounts of β-GlcCer and β-GalCer, however, were also significantly reduced in mice under HFD, not allowing a conclusion of BdS-α-GalCer being of bacterial (Bacteroides) origin. The purification and concentration of the BdS-α-GalCer from caecum and feces of WT mice combined with structural elucidations/verifications such as high resolution mass spectrometry and specific MS fragmentation of the sodium adduct should give proof of a possible α-glycosidic linkage (ratio of MS^2 fragment $[M+Na-Hexose]^+$ over $[M+Na+H_20-Hex]^+$) as well as the possible β-hydroxylation of the amid bound fatty acid (McLafferty fragmentation products) [219–221].

5 References

(1) Hakomori, S. Bifunctional Role of Glycosphingolipids. *J. Biol. Chem.* **1990**, *265* (31), 18713–18716.

(2) Gault, C. R.; Obeid, L. M.; Hannun, Y. A. An Overview of Sphingolipid Metabolism: From Synthesis to Breakdown. *Adv. Exp. Med. Biol.* **2010**, *688*, 1–23.

(3) Merrill, A. H. Sphingolipid and Glycosphingolipid Metabolic Pathways in the Era of Sphingolipidomics. *Chem. Rev.* **2011**, *111* (10), 6387–6422.

(4) Sandhoff, R.; Schulze, H.; Sandhoff, K. *Ganglioside Metabolism in Health and Disease*; Elsevier Inc., 2018.

(5) Jenemann, R.; Gröne, H.-J. Cell-Specific in Vivo Functions of Glycosphingolipids: Lessons from Genetic Deletions of Enzymes Involved in Glycosphingolipid Synthesis. *Prog. Lipid Res.* **2013**, *52* (2), 231–248.

(6) Young, M. M.; Kester, M.; Wang, H.-G. Sphingolipids: Regulators of Crosstalk between Apoptosis and Autophagy. *J. Lipid Res.* **2013**, *54* (1), 5–19.

(7) Schnaar, R. L.; Kinoshita, T. *Glycosphingolipids*; Cold Spring Harbor Laboratory Press, 2015.

(8) Olsen, I.; Jantzen, E. Sphingolipids in Bacteria and Fungi. *Anaerobe* **2001**, *7* (2), 103–112.

(9) Larsen, P. J.; Tennagels, N. On Ceramides, Other Sphingolipids and Impaired Glucose Homeostasis. *Mol. Metab.* **2014**, *3* (3), 252–260.

(10) Stahl, N.; Jurevics, H.; Morell, P.; Suzuki, K.; Popko, B. Isolation, Characterization, and Expression of CDNA Clones That Encode Rat UDP-Galactose: Ceramide Galactosyltransferase. *J. Neurosci. Res.* **1994**, *38* (2), 234–242.

(11) Ichikawa, S.; Sakiyama, H.; Suzuki, G.; Hidari, K. I.; Hirabayashi, Y. Expression Cloning of a CDNA for Human Ceramide Glucosyltransferase That Catalyzes the First Glycosylation Step of Glycosphingolipid Synthesis. *Proc. Natl. Acad. Sci. U. S. A.* **1996**, *93* (10), 4638–4643.

(12) Kain, L.; Webb, B.; Anderson, B. L.; Deng, S.; Holt, M.; Constanzo, A.; Zhao, M.; Self, K.; Teyton, A.; Everett, C.; et al. The Identification of the Endogenous Ligands of Natural Killer T Cells Reveals the Presence of Mammalian α-Linked Glycosylceramides. *Immunity* **2014**, *41* (4), 543–554.

(13) Natori, T.; Koezuka, Y.; Higa, T. Agelasphins, Novel α-Galactosylceramides from the Marine Sponge Agelas Mauritianus. *Tetrahedron Lett.* **1993**, *34* (35), 5591–5592.

(14) Wieland Brown, L. C.; Penaranda, C.; Kashyap, P. C.; Williams, B. B.; Clardy, J.; Kronenberg, M.; Sonnenburg, J. L.; Comstock, L. E.; Bluestone, J. A.; Fischbach, M. A.; et al. Production of α-Galactosylceramide by a Prominent Member of the Human Gut Microbiota. *PLoS Biol.* **2013**, *11* (7), e1001610.

(15) Klenk, E. Die Fettstoffe Des Gehirns Bei Amaurotischer Idiotie Und Niemann-Pick'scher Krankheit. *Ber. Ges. Physiol* **1937**, *96*, 659–660.

(16) Kuhn, R.; Wiegandt, H. Die Konstitution Der Ganglioside Gn , Gm Und Giv. *Zeitschrift für Naturforsch.* **1963**, *18* (7), 541–543.

(17) Liang, Y.-J.; Yang, B.-C.; Chen, J.-M.; Lin, Y.-H.; Huang, C.-L.; Cheng, Y.-Y.; Hsu, C.-Y.; Khoo, K.-H.; Shen, C.-N.; Yu, J. Changes in Glycosphingolipid Composition During Differentiation of Human Embryonic Stem Cells to Ectodermal or Endodermal Lineages. *Stem Cells* **2011**, *29* (12), 1995–2004.

(18) Rahmann, H. Functional Meaning of Neuronal Gangliosides for the Process of Thermal Adaptation in Vertebrates. *J. Therm. Biol.* **1983**, *8* (4), 404–407.

(19) Yu, R. K.; Tsai, Y.-T.; Ariga, T. Functional Roles of Gangliosides in Neurodevelopment: An Overview of Recent Advances. *Neurochem. Res.* **2012**, *37* (6), 1230–1244.

(20) Caughlin, S.; Maheshwari, S.; Weishaupt, N.; Yeung, K. K.-C.; Cechetto, D. F.; Whitehead, S. N. Age-Dependent and Regional Heterogeneity in the Long-Chain Base of A-Series Gangliosides Observed in the Rat Brain Using MALDI Imaging. *Sci. Rep.* **2017**, *7* (1), 16135.

(21) Inokuchi, J. Membrane Microdomains and Insulin Resistance. *FEBS Lett.* **2010**, *584* (9), 1864–1871.

(22) Ohmi, Y.; Ohkawa, Y.; Yamauchi, Y.; Tajima, O.; Furukawa, K.; Furukawa, K. Essential Roles of Gangliosides in the Formation and Maintenance of Membrane Microdomains in Brain Tissues. *Neurochem. Res.* **2012**, *37* (6), 1185–1191.

(23) Nordström, V.; Willershäuser, M.; Herzer, S.; Rozman, J.; von Bohlen und Halbach, O.; Meldner, S.; Rothermel, U.; Kaden, S.; Roth, F. C.; Waldeck, C.; et al. Neuronal Expression of Glucosylceramide Synthase in Central Nervous System Regulates Body Weight and Energy Homeostasis. *PLoS Biol.* **2013**, *11* (3), e1001506.

(24) Coskun, Ü.; Grzybek, M.; Drechsel, D.; Simons, K. Regulation of Human EGF Receptor by Lipids. *Proc. Natl. Acad. Sci. U. S. A.* **2011**, *108* (22), 9044–9048.

(25) Bosio, A.; Binczek, E.; Stoffel, W. Functional Breakdown of the Lipid Bilayer of the Myelin Membrane in Central and Peripheral Nervous System by Disrupted Galactocerebroside Synthesis. *Proc. Natl. Acad. Sci.* **1996**, *93* (23), 13280–13285.

(26) Coetzee, T.; Fujita, N.; Dupree, J.; Shi, R.; Blight, A.; Suzuki, K.; Suzuki, K.; Popko, B. Myelination in the Absence of Galactocerebroside and Sulfatide: Normal Structure with Abnormal Function and Regional Instability. *Cell* **1996**, *86* (2), 209–219.

(27) Yamashita, T.; Wada, R.; Sasaki, T.; Deng, C.; Bierfreund, U.; Sandhoff, K.; Proia, R. L. A Vital Role for Glycosphingolipid Synthesis during Development and Differentiation. *Proc. Natl. Acad. Sci. U. S. A.* **1999**, *96* (16), 9142–9147.

(28) Jennemann, R.; Sandhoff, R.; Wang, S.; Kiss, E.; Gretz, N.; Zuliani, C.; Martin-Villalba, A.; Jager, R.; Schorle, H.; Kenzelmann, M.; et al. Cell-Specific Deletion of Glucosylceramide Synthase in Brain Leads to Severe Neural Defects after Birth. *Proc. Natl. Acad. Sci.* **2005**, *102* (35), 12459–12464.

(29) Yamashita, T.; Allende, M. L.; Kalkofen, D. N.; Werth, N.; Sandhoff, K.; Proia, R. L. ConditionalLoxP-Flanked Glucosylceramide Synthase Allele Controlling Glycosphingolipid Synthesis. *genesis* **2005**, *43* (4), 175–180.

(30) Watanabe, S.; Endo, S.; Oshima, E.; Hoshi, T.; Higashi, H.; Yamada, K.; Tohyama, K.;

Yamashita, T.; Hirabayashi, Y. Glycosphingolipid Synthesis in Cerebellar Purkinje Neurons: Roles in Myelin Formation and Axonal Homeostasis. *Glia* **2010**, *58* (10), 1197–1207.

(31) Herzer, S.; Meldner, S.; Gröne, H.-J.; Nordström, V. Fasting-Induced Lipolysis and Hypothalamic Insulin Signaling Are Regulated by Neuronal Glucosylceramide Synthase. *Diabetes* **2015**, *64* (10), 3363–3376.

(32) Saadat, L.; Dupree, J. L.; Kilkus, J.; Han, X.; Traka, M.; Proia, R. L.; Dawson, G.; Popko, B. Absence of Oligodendroglial Glucosylceramide Synthesis Does Not Result in CNS Myelin Abnormalities or Alter the Dysmyelinating Phenotype of CGT-Deficient Mice. *Glia* **2010**, *58* (4), 391–398.

(33) Jennemann, R.; Rothermel, U.; Wang, S.; Sandhoff, R.; Kaden, S.; Out, R.; van Berkel, T. J.; Aerts, J. M.; Ghauharali, K.; Sticht, C.; et al. Hepatic Glycosphingolipid Deficiency and Liver Function in Mice. *Hepatology* **2010**, *51* (5), 1799–1809.

(34) Jennemann, R.; Kaden, S.; Sandhoff, R.; Nordström, V.; Wang, S.; Volz, M.; Robine, S.; Amen, N.; Rothermel, U.; Wiegandt, H.; et al. Glycosphingolipids Are Essential for Intestinal Endocytic Function. *J. Biol. Chem.* **2012**, *287* (39), 32598–32616.

(35) Stettner, P.; Bourgeois, S.; Marsching, C.; Traykova-Brauch, M.; Porubsky, S.; Nordstrom, V.; Hopf, C.; Koesters, R.; Sandhoff, R.; Wiegandt, H.; et al. Sulfatides Are Required for Renal Adaptation to Chronic Metabolic Acidosis. *Proc. Natl. Acad. Sci.* **2013**, *110* (24), 9998–10003.

(36) Amen, N.; Mathow, D.; Rabionet, M.; Sandhoff, R.; Langbein, L.; Gretz, N.; Jäckel, C.; Gröne, H.-J.; Jennemann, R. Differentiation of Epidermal Keratinocytes Is Dependent on Glucosylceramide:Ceramide Processing. *Hum. Mol. Genet.* **2013**, *22* (20), 4164–4179.

(37) Hirahara, Y.; Tsuda, M.; Wada, Y.; Honke, K. CDNA Cloning, Genomic Cloning, and Tissue-Specific Regulation of Mouse Cerebroside Sulfotransferase. *Eur. J. Biochem.* **2000**, *267* (7), 1909–1917.

(38) Eckhardt, M. The Role and Metabolism of Sulfatide in the Nervous System. *Mol. Neurobiol.* **2008**, *37* (2–3), 93–103.

(39) Takahashi, T.; Suzuki, T. Role of Sulfatide in Normal and Pathological Cells and Tissues. *J. Lipid Res.* **2012**, *53* (8), 1437–1450.

(40) Ishizuka, I. Chemistry and Functional Distribution of Sulfoglycolipids. *Prog. Lipid Res.* **1997**, *36* (4), 245–319.

(41) Honke, K.; Hirahara, Y.; Dupree, J.; Suzuki, K.; Popko, B.; Fukushima, K.; Fukushima, J.; Nagasawa, T.; Yoshida, N.; Wada, Y. Paranodal Junction Formation and Spermatogenesis Require Sulfoglycolipids. *Proc. Natl. Acad. Sci.* **2002**, *99* (7), 4227–4232.

(42) Ishibashi, T.; Dupree, J. L.; Ikenaka, K.; Hirahara, Y.; Honke, K.; Peles, E.; Popko, B.; Suzuki, K.; Nishino, H.; Baba, H. A Myelin Galactolipid, Sulfatide, Is Essential for Maintenance of Ion Channels on Myelinated Axon but Not Essential for Initial Cluster Formation. *J. Neurosci.* **2002**, *22* (15), 6507–6514.

(43) Hayashi, A.; Kaneko, N.; Tomihira, C.; Baba, H. Sulfatide Decrease in Myelin Influences Formation of the Paranodal Axo-glial Junction and Conduction Velocity in the Sciatic Nerve. *Glia*

2013, *61* (4), 466–474.

(44) Hirahara, Y.; Bansal, R.; Honke, K.; Ikenaka, K.; Wada, Y. Sulfatide Is a Negative Regulator of Oligodendrocyte Differentiation: Development in Sulfatide-Null Mice. *Glia* **2004**, *45* (3), 269–277.

(45) Okuda, T.; Tokuda, N.; Numata, S.; Ito, M.; Ohta, M.; Kawamura, K.; Wiels, J.; Urano, T.; Tajima, O.; Furukawa, K.; et al. Targeted Disruption of Gb3/CD77 Synthase Gene Resulted in the Complete Deletion of Globo-Series Glycosphingolipids and Loss of Sensitivity to Verotoxins. *J. Biol. Chem.* **2006**, *281* (15), 10230–10235.

(46) Porubsky, S.; Speak, A. O.; Salio, M.; Jennemann, R.; Bonrouhi, M.; Zafarulla, R.; Singh, Y.; Dyson, J.; Luckow, B.; Lehuen, A.; et al. Globosides but Not Isoglobosides Can Impact the Development of Invariant NKT Cells and Their Interaction with Dendritic Cells. *J. Immunol.* **2012**, *189* (6), 3007–3017.

(47) Morace, I. Globotriaosylceramide, the Shigatoxin Receptor, Contributes to Tubular Protein Absorption and Toxic Acute Kidney Failure, University of Heidelberg, Medical Sciences, 2017.

(48) Furuya, S.; Irie, F.; Hashikawa, T.; Nakazawa, K.; Kozakai, A.; Hasegawa, A.; Sudo, K.; Hirabayashi, Y. Ganglioside GD1 Alpha in Cerebellar Purkinje Cells. Its Specific Absence in Mouse Mutants with Purkinje Cell Abnormality and Altered Immunoreactivity in Response to Conjunctive Stimuli Causing Long-Term Desensitization. *J. Biol. Chem.* **1994**, *269* (51), 32418–32425.

(49) Yamashita, T.; Hashiramoto, A.; Haluzik, M.; Mizukami, H.; Beck, S.; Norton, A.; Kono, M.; Tsuji, S.; Daniotti, J. L.; Werth, N.; et al. Enhanced Insulin Sensitivity in Mice Lacking Ganglioside GM3. *Proc. Natl. Acad. Sci. U. S. A.* **2003**, *100* (6), 3445–3449.

(50) Wang, X.-Q.; Lee, S.; Wilson, H.; Seeger, M.; Iordanov, H.; Gatla, N.; Whittington, A.; Bach, D.; Lu, J.; Paller, A. S. Ganglioside GM3 Depletion Reverses Impaired Wound Healing in Diabetic Mice by Activating IGF-1 and Insulin Receptors. *J. Invest. Dermatol.* **2014**, *134* (5), 1446–1455.

(51) Menichella, D. M.; Jayaraj, N. D.; Wilson, H. M.; Ren, D.; Flood, K.; Wang, X.-Q.; Shum, A.; Miller, R. J.; Paller, A. S. Ganglioside GM3 Synthase Depletion Reverses Neuropathic Pain and Small Fiber Neuropathy in Diet-Induced Diabetic Mice. *Mol. Pain* **2016**, *12*, 174480691666628.

(52) Niimi, K.; Nishioka, C.; Miyamoto, T.; Takahashi, E.; Miyoshi, I.; Itakura, C.; Yamashita, T. Impairment of Neuropsychological Behaviors in Ganglioside GM3-Knockout Mice. *Biochem. Biophys. Res. Commun.* **2011**, *406* (4), 524–528.

(53) Okada, M.; Itoh Mi, M.; Haraguchi, M.; Okajima, T.; Inoue, M.; Oishi, H.; Matsuda, Y.; Iwamoto, T.; Kawano, T.; Fukumoto, S.; et al. B-Series Ganglioside Deficiency Exhibits No Definite Changes in the Neurogenesis and the Sensitivity to Fas-Mediated Apoptosis but Impairs Regeneration of the Lesioned Hypoglossal Nerve. *J. Biol. Chem.* **2002**, *277* (3), 1633–1636.

(54) Kawai, H.; Sango, K.; Mullin, K. A.; Proia, R. L. Embryonic Stem Cells with a Disrupted GD3 Synthase Gene Undergo Neuronal Differentiation in the Absence of B-Series Gangliosides. *J. Biol. Chem.* **1998**, *273* (31), 19634–19638.

(55) Kawai, H.; Allende, M. L.; Wada, R.; Kono, M.; Sango, K.; Deng, C.; Miyakawa, T.; Crawley, J. N.; Werth, N.; Bierfreund, U.; et al. Mice Expressing Only Monosialoganglioside GM3 Exhibit

Lethal Audiogenic Seizures. *J. Biol. Chem.* **2001**, *276* (10), 6885–6888.

(56) Ribeiro-Resende, V. T.; Gomes, T. A.; de Lima, S.; Nascimento-Lima, M.; Bargas-Rega, M.; Santiago, M. F.; Reis, R. A. de M.; de Mello, F. G. Mice Lacking GD3 Synthase Display Morphological Abnormalities in the Sciatic Nerve and Neuronal Disturbances during Peripheral Nerve Regeneration. *PLoS One* **2014**, *9* (10), e108919.

(57) Wang, J.; Yu, R. K. Interaction of Ganglioside GD3 with an EGF Receptor Sustains the Self-Renewal Ability of Mouse Neural Stem Cells in Vitro. *Proc. Natl. Acad. Sci. U. S. A.* **2013**, *110* (47), 19137–19142.

(58) Wang, J.; Cheng, A.; Wakade, C.; Yu, R. K. Ganglioside GD3 Is Required for Neurogenesis and Long-Term Maintenance of Neural Stem Cells in the Postnatal Mouse Brain. *J. Neurosci.* **2014**, *34* (41), 13790–13800.

(59) Ariga, T.; Itokazu, Y.; McDonald, M. P.; Hirabayashi, Y.; Ando, S.; Yu, R. K. Brain Gangliosides of a Transgenic Mouse Model of Alzheimer's Disease with Deficiency in GD3-Synthase: Expression of Elevated Levels of a Cholinergic-Specific Ganglioside, GT1aα. **2013**.

(60) Bernardo, A.; Harrison, F. E.; McCord, M.; Zhao, J.; Bruchey, A.; Davies, S. S.; Roberts, L. J.; Mathews, P. M.; Matsuoka, Y.; Ariga, T. Elimination of GD3 Synthase Improves Memory and Reduces Amyloid-β Plaque Load in Transgenic Mice. *Neurobiol. Aging* **2009**, *30* (11), 1777–1791.

(61) Akkhawattanangkul, Y.; Maiti, P.; Xue, Y.; Aryal, D.; Wetsel, W. C.; Hamilton, D.; Fowler, S. C.; McDonald, M. P. Targeted Deletion of GD3 Synthase Protects against MPTP-induced Neurodegeneration. *Genes, Brain Behav.* **2017**, *16* (5), 522–536.

(62) Takamiya, K.; Yamamoto, A.; Furukawa, K.; Yamashiro, S.; Shin, M.; Okada, M.; Fukumoto, S.; Haraguchi, M.; Takeda, N.; Fujimura, K.; et al. Mice with Disrupted GM2/GD2 Synthase Gene Lack Complex Gangliosides but Exhibit Only Subtle Defects in Their Nervous System. *Proc. Natl. Acad. Sci. U. S. A.* **1996**, *93* (20), 10662–10667.

(63) Sheikh, K. A.; Sun, J.; Liu, Y.; Kawai, H.; Crawford, T. O.; Proia, R. L.; Griffin, J. W.; Schnaar, R. L. Mice Lacking Complex Gangliosides Develop Wallerian Degeneration and Myelination Defects. *Proc. Natl. Acad. Sci. U. S. A.* **1999**, *96* (13), 7532–7537.

(64) Chiavegatto, S. A Functional Role for Complex Gangliosides: Motor Deficits in GM2/GD2 Synthase Knockout Mice. *Exp. Neurol.* **2000**, *166* (2), 227–234.

(65) Sugiura, Y.; Furukawa, K.; Tajima, O.; Mii, S.; Honda, T. Sensory Nerve-Dominant Nerve Degeneration and Remodeling in the Mutant Mice Lacking Complex Gangliosides. *Neuroscience* **2005**, *135* (4), 1167–1178.

(66) Sha, S.; Zhou, L.; Yin, J.; Takamiya, K.; Furukawa, K.; Furukawa, K.; Sokabe, M.; Chen, L. Deficits in Cognitive Function and Hippocampal Plasticity in GM2/GD2 Synthase Knockout Mice. *Hippocampus* **2014**, *24* (4), 369–382.

(67) Yin, X.; Crawford, T. O.; Griffin, J. W.; Tu, P.; Lee, V. M.-Y.; Li, C.; Roder, J.; Trapp, B. D. Myelin-Associated Glycoprotein Is a Myelin Signal That Modulates the Caliber of Myelinated Axons. *J. Neurosci.* **1998**, *18* (6), 1953–1962.

(68) Wu, G.; Xie, X.; Lu, Z.-H.; Ledeen, R. W. Cerebellar Neurons Lacking Complex Gangliosides Degenerate in the Presence of Depolarizing Levels of Potassium. *Proc. Natl. Acad. Sci.* **2001**, *98* (1), 307–312.

(69) Wu, G.; Lu, Z.-H.; Xie, X.; Ledeen, R. W. Susceptibility of Cerebellar Granule Neurons from GM2/GD2 Synthase-Null Mice to Apoptosis Induced by Glutamate Excitotoxicity and Elevated KCl: Rescue by GM1 and LIGA20. *Glycoconj. J.* **2004**, *21* (6), 305–313.

(70) Sandhoff, K.; Harzer, K. Gangliosides and Gangliosidoses: Principles of Molecular and Metabolic Pathogenesis. *J. Neurosci.* **2013**, *33* (25), 10195–10208.

(71) Miyagi, T.; Yamaguchi, K. Mammalian Sialidases: Physiological and Pathological Roles in Cellular Functions. *Glycobiology* **2012**, *22* (7), 880–896.

(72) d'Azzo, A.; Bonten, E. Molecular Mechanisms of Pathogenesis in a Glycosphingolipid and a Glycoprotein Storage Disease. *Biochem. Soc. Trans.* **2010**, *38* (6), 1453–1457.

(73) Bonten, E.; van der Spoel, A.; Fornerod, M.; Grosveld, G.; d'Azzo, A. Characterization of Human Lysosomal Neuraminidase Defines the Molecular Basis of the Metabolic Storage Disorder Sialidosis. *Genes Dev.* **1996**, *10* (24), 3156–3169.

(74) Pshezhetsky, A. V.; Ashmarina, M. Lysosomal Multienzyme Complex: Biochemistry, Genetics, and Molecular Pathophysiology. *Prog. Nucleic Acid Res. Mol. Biol.* **2001**, *69*, 81–94.

(75) Smutova, V.; Albohy, A.; Pan, X.; Korchagina, E.; Miyagi, T.; Bovin, N.; Cairo, C. W.; Pshezhetsky, A. V. Structural Basis for Substrate Specificity of Mammalian Neuraminidases. *PLoS One* **2014**, *9* (9), e106320.

(76) Timur, Z. K.; Akyildiz Demir, S.; Marsching, C.; Sandhoff, R.; Seyrantepe, V. Neuraminidase-1 Contributes Significantly to the Degradation of Neuronal B-Series Gangliosides but Not to the Bypass of the Catabolic Block in Tay-Sachs Mouse Models. *Mol. Genet. Metab. reports* **2015**, *4*, 72–82.

(77) Miyagi, T.; Wada, T.; Iwamatsu, A.; Hata, K.; Yoshikawa, Y.; Tokuyama, S.; Sawada, M. Molecular Cloning and Characterization of a Plasma Membrane-Associated Sialidase Specific for Gangliosides. *J. Biol. Chem.* **1999**, *274* (8), 5004–5011.

(78) Monti, E.; Bassi, M. T.; Papini, N.; Riboni, M.; Manzoni, M.; Venerando, B.; Croci, G.; Preti, A.; Ballabio, A.; Tettamanti, G.; et al. Identification and Expression of NEU3, a Novel Human Sialidase Associated to the Plasma Membrane. *Biochem. J.* **2000**, *349* (Pt 1), 343–351.

(79) Zanchetti, G.; Colombi, P.; Manzoni, M.; Anastasia, L.; Caimi, L.; Borsani, G.; Venerando, B.; Tettamanti, G.; Preti, A.; Monti, E.; et al. Sialidase NEU3 Is a Peripheral Membrane Protein Localized on the Cell Surface and in Endosomal Structures. *Biochem. J.* **2007**, *408* (2), 211–219.

(80) Albohy, A.; Li, M. D.; Zheng, R. B.; Zou, C.; Cairo, C. W. Insight into Substrate Recognition and Catalysis by the Human Neuraminidase 3 (NEU3) through Molecular Modeling and Site-Directed Mutagenesis. *Glycobiology* **2010**, *20* (9), 1127–1138.

(81) Ha, K. T.; Lee, Y. C.; Cho, S. H.; Kim, J. K.; Kim, C. H. Molecular Characterization of Membrane Type and Ganglioside-Specific Sialidase (Neu3) Expressed in E. Coli. *Mol. Cells* **2004**, *17* (2), 267–273.

(82) Papini, N.; Anastasia, L.; Tringali, C.; Croci, G.; Bresciani, R.; Yamaguchi, K.; Miyagi, T.; Preti, A.; Prinetti, A.; Prioni, S.; et al. The Plasma Membrane-Associated Sialidase MmNEU3 Modifies the Ganglioside Pattern of Adjacent Cells Supporting Its Involvement in Cell-to-Cell Interactions. *J. Biol. Chem.* **2004**, *279* (17), 16989–16995.

(83) Kappagantula, S.; Andrews, M. R.; Cheah, M.; Abad-Rodriguez, J.; Dotti, C. G.; Fawcett, J. W. Neu3 Sialidase-Mediated Ganglioside Conversion Is Necessary for Axon Regeneration and Is Blocked in CNS Axons. *J. Neurosci.* **2014**, *34* (7), 2477–2492.

(84) Wang, J.; Wu, G.; Miyagi, T.; Lu, Z.-H.; Ledeen, R. W. Sialidase Occurs in Both Membranes of the Nuclear Envelope and Hydrolyzes Endogenous GD1a. *J. Neurochem.* **2009**, *111* (2), 547–554.

(85) Seyrantepe, V.; Demir, S. A.; Timur, Z. K.; Von Gerichten, J.; Marsching, C.; Erdemli, E.; Oztas, E.; Takahashi, K.; Yamaguchi, K.; Ates, N.; et al. Murine Sialidase Neu3 Facilitates GM2 Degradation and Bypass in Mouse Model of Tay-Sachs Disease. *Exp. Neurol.* **2018**, *299* (Pt A), 26–41.

(86) Bigi, A.; Morosi, L.; Pozzi, C.; Forcella, M.; Tettamanti, G.; Venerando, B.; Monti, E.; Fusi, P. Human Sialidase NEU4 Long and Short Are Extrinsic Proteins Bound to Outer Mitochondrial Membrane and the Endoplasmic Reticulum, Respectively. *Glycobiology* **2010**, *20* (2), 148–157.

(87) Yamaguchi, K.; Hata, K.; Koseki, K.; Shiozaki, K.; Akita, H.; Wada, T.; Moriya, S.; Miyagi, T. Evidence for Mitochondrial Localization of a Novel Human Sialidase (NEU4). *Biochem. J.* **2005**, *390* (Pt 1), 85–93.

(88) Seyrantepe, V.; Canuel, M.; Carpentier, S.; Landry, K.; Durand, S.; Liang, F.; Zeng, J.; Caqueret, A.; Gravel, R. A.; Marchesini, S.; et al. Mice Deficient in Neu4 Sialidase Exhibit Abnormal Ganglioside Catabolism and Lysosomal Storage. *Hum. Mol. Genet.* **2008**, *17* (11), 1556–1568.

(89) Pan, X.; De Aragão, C. D. B. P.; Velasco-Martin, J. P.; Priestman, D. A.; Wu, H. Y.; Takahashi, K.; Yamaguchi, K.; Sturiale, L.; Garozzo, D.; Platt, F. M.; et al. Neuraminidases 3 and 4 Regulate Neuronal Function by Catabolizing Brain Gangliosides. *FASEB J.* **2017**, *31* (8), 3467–3483.

(90) Massimo, A.; Maura, S.; Nicoletta, L.; Giulia, M.; Valentina, M.; Elena, C.; Alessandro, P.; Rosaria, B.; Sandro, S. Current and Novel Aspects on the Non-Lysosomal β-Glucosylceramidase GBA2. *Neurochem. Res.* **2016**, *41* (1–2), 210–220.

(91) Yildiz, Y.; Matern, H.; Thompson, B.; Allegood, J. C.; Warren, R. L.; Ramirez, D. M. O.; Hammer, R. E.; Hamra, F. K.; Matern, S.; Russell, D. W. Mutation of Beta-Glucosidase 2 Causes Glycolipid Storage Disease and Impaired Male Fertility. *J. Clin. Invest.* **2006**, *116* (11), 2985–2994.

(92) Gonzalez-Carmona, M. A.; Sandhoff, R.; Tacke, F.; Vogt, A.; Weber, S.; Canbay, A. E.; Rogler, G.; Sauerbruch, T.; Lammert, F.; Yildiz, Y. Beta-Glucosidase 2 Knockout Mice with Increased Glucosylceramide Show Impaired Liver Regeneration. *Liver Int.* **2012**, *32* (9), 1354–1362.

(93) Sandhoff, K.; Harzer, K.; Wässle, W.; Jatzkewitz, H. ENZYME ALTERATIONS AND LIPID STORAGE IN THREE VARIANTS OF TAY-SACHS DISEASE. *J. Neurochem.* **1971**, *18* (12), 2469–2489.

(94) Sandhoff, K.; Jatzkewitz, H.; Peters, G. Infantile Amaurotic Idiocy and Related Forms as

Ganglioside Storage Diseases. *Naturwissenschaften* **1969**, *56* (7), 356–362.

(95) Kolter, T.; Sandhoff, K. Sphingolipid Metabolism Diseases. *Biochim. Biophys. Acta (BBA)-Biomembranes* **2006**, *1758* (12), 2057–2079.

(96) Kaufman, B.; Basu, S.; Roseman, S.; Aronson, S. M.; Volk, B. W. Inborn Disorders of Sphingolipid Metabolism. *by SM. Aronson, BW Volk) Pergamon Press. New York* **1966**, 193.

(97) Cachon-Gonzalez, M. B.; Zaccariotto, E.; Cox, T. M. Genetics and Therapies for GM2 Gangliosidosis. *Curr. Gene Ther.* **2018**, *18* (2), 68–89.

(98) Bembi, B.; Marchetti, F.; Guerci, V. I.; Ciana, G.; Addobbati, R.; Grasso, D.; Barone, R.; Cariati, R.; Fernandez-Guillen, L.; Butters, T.; et al. Substrate Reduction Therapy in the Infantile Form of Tay-Sachs Disease. *Neurology* **2006**, *66* (2), 278–280.

(99) von Specht, B. U.; Geiger, B.; Arnon, R.; Passwell, J.; Keren, G.; Goldman, B.; Padeh, B. Enzyme Replacement in Tay-Sachs Disease. *Neurology* **1979**, *29* (6), 848–854.

(100) Martino, S.; Marconi, P.; Tancini, B.; Dolcetta, D.; De Angelis, M. G. C.; Montanucci, P.; Bregola, G.; Sandhoff, K.; Bordignon, C.; Emiliani, C.; et al. A Direct Gene Transfer Strategy via Brain Internal Capsule Reverses the Biochemical Defect in Tay–Sachs Disease. *Hum. Mol. Genet.* **2005**, *14* (15), 2113–2123.

(101) Sango, K.; Yamanaka, S.; Hoffmann, A.; Okuda, Y.; Grinberg, A.; Westphal, H.; McDonald, M. P.; Crawley, J. N.; Sandhoff, K.; Suzuki, K.; et al. Mouse Models of Tay–Sachs and Sandhoff Diseases Differ in Neurologic Phenotype and Ganglioside Metabolism. *Nat. Genet.* **1995**, *11* (2), 170–176.

(102) Seyrantepe, V.; Lema, P.; Caqueret, A.; Dridi, L.; Hadj, S. B.; Carpentier, S.; Boucher, F.; Levade, T.; Carmant, L.; Gravel, R. A.; et al. Mice Doubly-Deficient in Lysosomal Hexosaminidase a and Neuraminidase 4 Show Epileptic Crises and Rapid Neuronal Loss. *PLoS Genet.* **2010**, *6* (9), e1001118.

(103) Bendelac, A.; Rivera, M. N.; Park, S.-H.; Roark, J. H. MOUSE CD1-SPECIFIC NK1 T CELLS: Development, Specificity, and Function. *Annu. Rev. Immunol.* **1997**, *15* (1), 535–562.

(104) Anderson, B.; Teyton, L.; Bendelac, A.; Savage, P. Stimulation of Natural Killer T Cells by Glycolipids. *Molecules* **2013**, *18* (12), 15662–15688.

(105) Zhou, D.; Cantu, C.; Sagiv, Y.; Schrantz, N.; Kulkarni, A. B.; Qi, X.; Mahuran, D. J.; Morales, C. R.; Grabowski, G. A.; Benlagha, K. Editing of CD1d-Bound Lipid Antigens by Endosomal Lipid Transfer Proteins. *Science (80-.).* **2004**, *303* (5657), 523–527.

(106) Kang, S.-J.; Cresswell, P. Saposins Facilitate CD1d-Restricted Presentation of an Exogenous Lipid Antigen to T Cells. *Nat. Immunol.* **2004**, *5* (2), 175.

(107) Vartabedian, V. F.; Savage, P. B.; Teyton, L. The Processing and Presentation of Lipids and Glycolipids to the Immune System. *Immunol. Rev.* **2016**, *272* (1), 109–119.

(108) Kronenberg, M. Toward an Understanding of NKT Cell Biology: Progress and Paradoxes. *Annu. Rev. Immunol.* **2005**, *26*, 877–900.

(109) Schneiders, F. L.; Scheper, R. J.; von Blomberg, B. M. E.; Woltman, A. M.; Janssen, H. L. A.; van den Eertwegh, A. J. M.; Verheul, H. M. W.; de Gruijl, T. D.; van der Vliet, H. J. Clinical

Experience with α-Galactosylceramide (KRN7000) in Patients with Advanced Cancer and Chronic Hepatitis B/C Infection. *Clin. Immunol.* **2011**, *140* (2), 130–141.

(110) Tsuji, M. Glycolipids and Phospholipids as Natural CD1d-Binding NKT Cell Ligands. *Cell. Mol. Life Sci. C.* **2006**, *63* (16), 1889–1898.

(111) Karl, O. A.; Im, J. S.; Molano, A.; Dutronc, Y.; Illarionov, P. A.; Forestier, C.; Fujiwara, N.; Arias, I.; Miyake, S.; Yamamura, T. Modulation of CD1d-Restricted NKT Cell Responses by Using N-Acyl Variants of α-Galactosylceramides. *Proc. Natl. Acad. Sci. U. S. A.* **2005**, *102* (9), 3383–3388.

(112) Sullivan, B. A.; Nagarajan, N. A.; Wingender, G.; Wang, J.; Scott, I.; Tsuji, M.; Franck, R. W.; Porcelli, S. A.; Zajonc, D. M.; Kronenberg, M. Mechanisms for Glycolipid Antigen-Driven Cytokine Polarization by Vα14i NKT Cells. *J. Immunol.* **2010**, *184* (1), 141–153.

(113) Bendelac, A.; Savage, P. B.; Teyton, L. The Biology of NKT Cells. *Annu. Rev. Immunol.* **2007**, *25*, 297–336.

(114) Brennan, P. J.; Brigl, M.; Brenner, M. B. Invariant Natural Killer T Cells: An Innate Activation Scheme Linked to Diverse Effector Functions. *Nat. Rev. Immunol.* **2013**, *13* (2), 101–117.

(115) Zhou, D.; Mattner, J.; Cantu, C.; Schrantz, N.; Yin, N.; Gao, Y.; Sagiv, Y.; Hudspeth, K.; Wu, Y.-P.; Yamashita, T.; et al. Lysosomal Glycosphingolipid Recognition by NKT Cells. *Science (80-.).* **2004**, *306* (5702), 1786–1789.

(116) Porubsky, S.; Speak, A. O.; Luckow, B.; Cerundolo, V.; Platt, F. M.; Gröne, H.-J. Normal Development and Function of Invariant Natural Killer T Cells in Mice with Isoglobotrihexosylceramide (IGb3) Deficiency. *Proc. Natl. Acad. Sci. U. S. A.* **2007**, *104* (14), 5977–5982.

(117) Speak, A. O.; Salio, M.; Neville, D. C. A.; Fontaine, J.; Priestman, D. A.; Platt, N.; Heare, T.; Butters, T. D.; Dwek, R. A.; Trottein, F.; et al. Implications for Invariant Natural Killer T Cell Ligands Due to the Restricted Presence of Isoglobotrihexosylceramide in Mammals. *Proc. Natl. Acad. Sci.* **2007**, *104* (14), 5971–5976.

(118) Gumperz, J. E.; Christopher, R.; Makowska, A.; Lum, D.; Sugita, M.; Podrebarac, T.; Koezuka, Y.; Porcelli, S. A.; Cardell, S.; Brenner, M. B.; et al. Murine CD1d-Restricted T Cell Recognition of Cellular Lipids. *Immunity* **2000**, *12* (2), 211–221.

(119) Cox, D.; Fox, L.; Tian, R.; Bardet, W.; Skaley, M.; Mojsilovic, D.; Gumperz, J.; Hildebrand, W. Determination of Cellular Lipids Bound to Human CD1d Molecules. *PLoS One* **2009**, *4* (5), e5325.

(120) Facciotti, F.; Ramanjaneyulu, G. S.; Lepore, M.; Sansano, S.; Cavallari, M.; Kistowska, M.; Forss-Petter, S.; Ni, G.; Colone, A.; Singhal, A.; et al. Peroxisome-Derived Lipids Are Self Antigens That Stimulate Invariant Natural Killer T Cells in the Thymus. *Nat. Immunol.* **2012**, *13* (5), 474–480.

(121) Zeissig, S.; Murata, K.; Sweet, L.; Publicover, J.; Hu, Z.; Kaser, A.; Bosse, E.; Iqbal, J.; Hussain, M. M.; Balschun, K.; et al. Hepatitis B Virus–induced Lipid Alterations Contribute to Natural Killer T Cell–dependent Protective Immunity. *Nat. Med.* **2012**, *18* (7), 1060–1068.

(122) Stanic, A. K.; De Silva, a D.; Park, J.-J.; Sriram, V.; Ichikawa, S.; Hirabyashi, Y.; Hayakawa, K.; Van Kaer, L.; Brutkiewicz, R. R.; Joyce, S. Defective Presentation of the CD1d1-Restricted Natural Va14Ja18 NKT Lymphocyte Antigen Caused by Beta-D-Glucosylceramide Synthase Deficiency. *Proc. Natl. Acad. Sci. U. S. A.* **2003**, *100* (4), 1849–1854.

(123) Margalit, M.; Ghazala, S. A.; Alper, R.; Elinav, E.; Klein, A.; Doviner, V.; Sherman, Y.; Thalenfeld, B.; Engelhardt, D.; Rabbani, E.; et al. Glucocerebroside Treatment Ameliorates ConA Hepatitis by Inhibition of NKT Lymphocytes. *Am. J. Physiol. Liver Physiol.* **2005**, *289* (5), G917–G925.

(124) Brennan, P. J.; Tatituri, R. V. V; Brigl, M.; Kim, E. Y.; Tuli, A.; Sanderson, J. P.; Gadola, S. D.; Hsu, F.-F.; Besra, G. S.; Brenner, M. B. Invariant Natural Killer T Cells Recognize Lipid Self Antigen Induced by Microbial Danger Signals. *Nat. Immunol.* **2011**, *12* (12), 1202–1211.

(125) Popovic, Z. V.; Rabionet, M.; Jennemann, R.; Krunic, D.; Sandhoff, R.; Gröne, H.-J.; Porubsky, S. Glucosylceramide Synthase Is Involved in Development of Invariant Natural Killer T Cells. *Front. Immunol.* **2017**, *8*, 848.

(126) Pellicci, D. G.; Clarke, A. J.; Patel, O.; Mallevaey, T.; Beddoe, T.; Le Nours, J.; Uldrich, A. P.; McCluskey, J.; Besra, G. S.; Porcelli, S. A.; et al. Recognition of β-Linked Self Glycolipids Mediated by Natural Killer T Cell Antigen Receptors. *Nat. Immunol.* **2011**, *12* (9), 827–833.

(127) Wu, D. Y.; Segal, N. H.; Sidobre, S.; Kronenberg, M.; Chapman, P. B. Cross-Presentation of Disialoganglioside GD3 to Natural Killer T Cells. *J. Exp. Med.* **2003**, *198* (1), 173–181.

(128) Paget, C.; Mallevaey, T.; Speak, A. O.; Torres, D.; Fontaine, J.; Sheehan, K. C. F.; Capron, M.; Ryffel, B.; Faveeuw, C.; Leite de Moraes, M.; et al. Activation of Invariant NKT Cells by Toll-like Receptor 9-Stimulated Dendritic Cells Requires Type I Interferon and Charged Glycosphingolipids. *Immunity* **2007**, *27* (4), 597–609.

(129) Jahng, A.; Maricic, I.; Aguilera, C.; Cardell, S.; Halder, R. C.; Kumar, V. Prevention of Autoimmunity by Targeting a Distinct, Noninvariant CD1d-Reactive T Cell Population Reactive to Sulfatide. *J. Exp. Med.* **2004**, *199* (7), 947–957.

(130) Kim, J.; Kim, J. H.; Winau, F. Thinking Inside the Box: Endogenous α-Anomeric Lipid Antigens. *Immunity* **2014**, *41* (4), 505–506.

(131) Brennan, P. J.; Tatituri, R. V. V; Heiss, C.; Watts, G. F. M.; Hsu, F.-F.; Veerapen, N.; Cox, L. R.; Azadi, P.; Besra, G. S.; Brenner, M. B. Activation of INKT Cells by a Distinct Constituent of the Endogenous Glucosylceramide Fraction. *Proc. Natl. Acad. Sci. U. S. A.* **2014**, *111* (37), 13433–13438.

(132) Eckburg, P. B.; Bik, E. M.; Bernstein, C. N.; Purdom, E.; Dethlefsen, L.; Sargent, M.; Gill, S. R.; Nelson, K. E.; Relman, D. A. Diversity of the Human Intestinal Microbial Flora. *Science (80-.).* **2005**, *308* (5728), 1635–1638.

(133) Louis, P.; Hold, G. L.; Flint, H. J. The Gut Microbiota, Bacterial Metabolites and Colorectal Cancer. *Nat. Rev. Microbiol.* **2014**, *12* (10), 661–672.

(134) Hemarajata, P.; Versalovic, J. Effects of Probiotics on Gut Microbiota: Mechanisms of Intestinal Immunomodulation and Neuromodulation. *Therap. Adv. Gastroenterol.* **2013**, *6* (1), 39–51.

(135) Sears, C. L. Enterotoxigenic Bacteroides Fragilis: A Rogue among Symbiotes. *Clin. Microbiol.*

Rev. **2009**, *22* (2), 349–369.

(136) Rhee, K.-J.; Wu, S.; Wu, X.; Huso, D. L.; Karim, B.; Franco, A. A.; Rabizadeh, S.; Golub, J. E.; Mathews, L. E.; Shin, J. Induction of Persistent Colitis by a Human Commensal, Enterotoxigenic Bacteroides Fragilis, in Wild-Type C57BL/6 Mice. *Infect. Immun.* **2009**, *77* (4), 1708–1718.

(137) Wick, E. C.; Sears, C. L. Bacteroides Spp. and Diarrhea. *Curr. Opin. Infect. Dis.* **2010**, *23* (5), 470–474.

(138) An, D.; Oh, S. F.; Olszak, T.; Neves, J. F.; Avci, F. Y.; Erturk-Hasdemir, D.; Lu, X.; Zeissig, S.; Blumberg, R. S.; Kasper, D. L. Sphingolipids from a Symbiotic Microbe Regulate Homeostasis of Host Intestinal Natural Killer T Cells. *Cell* **2014**, *156* (1–2), 123–133.

(139) Hildebrandt, M. A.; Hoffmann, C.; Sherrill–Mix, S. A.; Keilbaugh, S. A.; Hamady, M.; Chen, Y.; Knight, R.; Ahima, R. S.; Bushman, F.; Wu, G. D. High-Fat Diet Determines the Composition of the Murine Gut Microbiome Independently of Obesity. *Gastroenterology* **2009**, *137* (5), 1716–1724.e2.

(140) Ma, X.; Torbenson, M.; Hamad, A. R. A.; Soloski, M. J.; Li, Z. High-Fat Diet Modulates Non-CD1d-Restricted Natural Killer T Cells and Regulatory T Cells in Mouse Colon and Exacerbates Experimental Colitis. *Clin. Exp. Immunol.* **2007**, *151* (1), 130–138.

(141) Anumula, K. R.; Dhume, S. T. High Resolution and High Sensitivity Methods for Oligosaccharide Mapping and Characterization by Normal Phase High Performance Liquid Chromatography Following Derivatization with Highly Fluorescent Anthranilic Acid. *Glycobiology* **1998**, *8* (7), 685–694.

(142) Merrill, A. H.; Sullards, M. C. Opinion Article on Lipidomics: Inherent Challenges of Lipidomic Analysis of Sphingolipids. *Biochim. Biophys. Acta - Mol. Cell Biol. Lipids* **2017**, *1862* (8), 774–776.

(143) Sullards, M. C.; Allegood, J. C.; Kelly, S.; Wang, E.; Haynes, C. A.; Park, H.; Chen, Y.; Merrill, A. H. Structure-Specific, Quantitative Methods for Analysis of Sphingolipids by Liquid Chromatography-Tandem Mass Spectrometry: “Inside-Out” Sphingolipidomics. *Methods Enzymol.* **2007**, *432* (07), 83–115.

(144) Fuchs, B.; Süß, R.; Schiller, J. An Update of MALDI-TOF Mass Spectrometry in Lipid Research. *Progress in Lipid Research*. Pergamon October 1, 2010, pp 450–475.

(145) Shaner, R. L.; Allegood, J. C.; Park, H.; Wang, E.; Kelly, S.; Haynes, C. A.; Sullards, M. C.; Merrill, A. H. Quantitative Analysis of Sphingolipids for Lipidomics Using Triple Quadrupole and Quadrupole Linear Ion Trap Mass Spectrometers. *J. Lipid Res.* **2009**, *50* (8), 1692–1707.

(146) Sullards, M. C.; Liu, Y.; Chen, Y.; Merrill, A. H. Analysis of Mammalian Sphingolipids by Liquid Chromatography Tandem Mass Spectrometry (LC-MS/MS) and Tissue Imaging Mass Spectrometry (TIMS). *Biochimica et Biophysica Acta - Molecular and Cell Biology of Lipids*. Elsevier November 1, 2011, pp 838–853.

(147) Fong, B.; Norris, C.; Lowe, E.; McJarrow, P. Liquid Chromatography–High-Resolution Mass Spectrometry for Quantitative Analysis of Gangliosides. *Lipids* **2009**, *44* (9), 867–874.

(148) Ma, L.; MacGibbon, A. K. H.; Jan Mohamed, H. J. B.; Loy, S.; Rowan, A.; McJarrow, P.; Fong,

B. Y. Determination of Ganglioside Concentrations in Breast Milk and Serum from Malaysian Mothers Using a High Performance Liquid Chromatography-Mass Spectrometry-Multiple Reaction Monitoring Method. *Int. Dairy J.* **2015**, *49*, 62–71.

(149) Li, Y.; Thapa, P.; Hawke, D.; Kondo, Y.; Furukawa, K.; Furukawa, K.; Hsu, F.-F.; Adlercreutz, D.; Weadge, J.; Palcic, M. M.; et al. Immunologic Glycosphingolipidomics and NKT Cell Development in Mouse Thymus. *J. Proteome Res.* **2009**, *8* (6), 2740–2751.

(150) Nakamura, K.; Suzuki, Y.; Goto-Inoue, N.; Yoshida-Noro, C.; Suzuki, A. Structural Characterization of Neutral Glycosphingolipids by Thin-Layer Chromatography Coupled to Matrix-Assisted Laser Desorption/Ionization Quadrupole Ion Trap Time-of-Flight MS/MS. *Anal. Chem.* **2006**, *78* (16), 5736–5743.

(151) Škrášková, K.; Claude, E.; Jones, E. A.; Towers, M.; Ellis, S. R.; Heeren, R. M. A. Enhanced Capabilities for Imaging Gangliosides in Murine Brain with Matrix-Assisted Laser Desorption/Ionization and Desorption Electrospray Ionization Mass Spectrometry Coupled to Ion Mobility Separation. *Methods* **2016**.

(152) Woods, A. S.; Colsch, B.; Jackson, S. N.; Post, J.; Baldwin, K.; Roux, A.; Hoffer, B.; Cox, B. M.; Hoffer, M.; Rubovitch, V.; et al. Gangliosides and Ceramides Change in a Mouse Model of Blast Induced Traumatic Brain Injury. *ACS Chem. Neurosci.* **2013**, *4* (4), 594–600.

(153) Harris, D. C. *Lehrbuch Der Quantitativen Analyse*; Springer-Verlag, 2014.

(154) Gross, J. H. *Mass Spectrometry: A Textbook*; Springer Science & Business Media, 2006.

(155) Gessel, M. M.; Norris, J. L.; Caprioli, R. M. MALDI Imaging Mass Spectrometry: Spatial Molecular Analysis to Enable a New Age of Discovery. *J. Proteomics* **2014**, *107*, 71–82.

(156) Norris, J. L.; Caprioli, R. M. Analysis of Tissue Specimens by Matrix-Assisted Laser Desorption/Ionization Imaging Mass Spectrometry in Biological and Clinical Research. *Chem. Rev.* **2013**, *113* (4), 2309–2342.

(157) Aichler, M.; Walch, A. MALDI Imaging Mass Spectrometry: Current Frontiers and Perspectives in Pathology Research and Practice. *Lab. Investig.* **2015**, *95* (4), 422–431.

(158) KRIEGSMANN, J.; KRIEGSMANN, M.; CASADONTE, R. MALDI TOF Imaging Mass Spectrometry in Clinical Pathology: A Valuable Tool for Cancer Diagnostics (Review). *Int. J. Oncol.* **2015**, *46* (3), 893–906.

(159) Takats, Z.; Wiseman, J. M.; Gologan, B.; Cooks, R. G. Mass Spectrometry Sampling Under Ambient Conditions with Desorption Electrospray Ionization. *Science (80-.).* **2004**, *306* (5695), 471–473.

(160) Wiseman, J. M.; Puolitaival, S. M.; Takáts, Z.; Cooks, R. G.; Caprioli, R. M. Mass Spectrometric Profiling of Intact Biological Tissue by Using Desorption Electrospray Ionization. *Angew. Chemie - Int. Ed.* **2005**, *44* (43), 7094–7097.

(161) Wiseman, J. M.; Ifa, D. R.; Venter, A.; Cooks, R. G. Ambient Molecular Imaging by Desorption Electrospray Ionization Mass Spectrometry. *Nat. Protoc.* **2008**, *3* (3), 517–524.

(162) Stettner, P.; Bourgeois, S.; Marsching, C.; Traykova-Brauch, M.; Porubskya, S.; Nordström, V.; Hopf, C.; Koesters, R.; Sandhoff, R.; Wiegandt, H.; et al. Sulfatides Are Required for Renal

Adaptation to Chronic Metabolic Acidosis. *PNAS* **2013**, *110* (24), 9998–10003.

(163) Zoller, I.; Meixner, M.; Hartmann, D.; Bussow, H.; Meyer, R.; Gieselmann, V.; Eckhardt, M. Absence of 2-Hydroxylated Sphingolipids Is Compatible with Normal Neural Development But Causes Late-Onset Axon and Myelin Sheath Degeneration. *J. Neurosci.* **2008**, *28* (39), 9741–9754.

(164) Eley, A.; Greenwood, D. F. Comparative Growth of Bacteroides Species in Various Anaerobic Culture Media. *J. Med. Microbiol.* **1985**, *19* (2), 195–201.

(165) Kain, L.; Webb, B.; Anderson, B. L.; Deng, S.; Holt, M.; Costanzo, A.; Zhao, M.; Self, K.; Teyton, A.; Everett, C.; et al. The Identification of the Endogenous Ligands of Natural Killer T Cells Reveals the Presence of Mammalian α-Linked Glycosylceramides. *Immunity* **2014**, *41* (4), 543–554.

(166) Kean, E. L. Separation of Gluco-and Galactocerebrosides by Means of Borate Thin-Layer Chromatography. *J. Lipid Res.* **1966**, *7* (3), 449–452.

(167) von Gerichten, J.; Schlosser, K.; Lamprecht, D.; Morace, I.; Eckhardt, M.; Wachten, D.; Jennemann, R.; Gröne, H.-J.; Mack, M.; Sandhoff, R. Diastereomer-Specific Quantification of Bioactive Hexosylceramides from Bacteria and Mammals. *J. Lipid Res.* **2017**, *58* (6), 1247–1258.

(168) Fülöp, A.; Porada, M. B.; Marsching, C.; Blott, H.; Meyer, B.; Tambe, S.; Sandhoff, R.; Junker, H. D.; Hopf, C. 4-Phenyl-α-Cyanocinnamic Acid Amide: Screening for a Negative Ion Matrix for MALDI-MS Imaging of Multiple Lipid Classes. *Anal. Chem.* **2013**, *85* (19), 9156–9163.

(169) Fong, B.; Norris, C.; Lowe, E.; McJarrow, P. Liquid Chromatography-High-Resolution Mass Spectrometry for Quantitative Analysis of Gangliosides. *Lipids* **2009**, *44* (9), 867–874.

(170) Zhang, J.; Ren, Y.; Huang, B.; Tao, B.; Ransborg Pedersen, M.; Li, D. Determination of Disialoganglioside GD3 and Monosialoganglioside GM3 in Infant Formulas and Whey Protein Concentrates by Ultra-Performance Liquid Chromatography/Electrospray Ionization Tandem Mass Spectrometry. *J. Sep. Sci.* **2012**, *35* (8), 937–946.

(171) Masson, E. A. Y.; Sibille, E.; Martine, L.; Chaux-Picquet, F.; Bretillon, L.; Berdeaux, O. Apprehending Ganglioside Diversity: A Comprehensive Methodological Approach. *J. Lipid Res.* **2015**, *56* (9), 1821–1835.

(172) Oikawa, N.; Matsubara, T.; Fukuda, R.; Yasumori, H.; Hatsuta, H.; Murayama, S.; Sato, T.; Suzuki, A.; Yanagisawa, K. Imbalance in Fatty-Acid-Chain Length of Gangliosides Triggers Alzheimer Amyloid Deposition in the Precuneus. *PLoS One* **2015**, *10* (3), e0121356.

(173) Ikeda, K.; Shimizu, T.; Taguchi, R. Targeted Analysis of Ganglioside and Sulfatide Molecular Species by LC/ESI-MS/MS with Theoretically Expanded Multiple Reaction Monitoring. *J. Lipid Res.* **2008**, *49* (12), 2678–2689.

(174) Lee, H.; German, J. B.; Kjelden, R.; Lebrilla, C. B.; Barile, D. Quantitative Analysis of Gangliosides in Bovine Milk and Colostrum- Based Dairy Products by Ultrahigh Performance Liquid Chromatography-Tandem Mass Spectrometry. **2013**.

(175) Basit, A.; Piomelli, D.; Armirotti, A. Rapid Evaluation of 25 Key Sphingolipids and Phosphosphingolipids in Human Plasma by LC-MS/MS. *Anal. Bioanal. Chem.* **2015**, *407* (17),

5189–5198.

(176) Kolter, T.; Sandhoff, K. Sphingolipide–ihre Stoffwechselwege Und Die Pathobiochemie Neurodegenerativer Erkrankungen. *Angew. Chemie* **1999**, *111* (11), 1632–1670.

(177) Imgrund, S.; Hartmann, D.; Farwanah, H.; Eckhardt, M.; Sandhoff, R.; Degen, J.; Gieselmann, V.; Sandhoff, K.; Willecke, K. Adult Ceramide Synthase 2 (CERS2)-Deficient Mice Exhibit Myelin Sheath Defects, Cerebellar Degeneration, and Hepatocarcinomas. *J. Biol. Chem.* **2009**, *284* (48), 33549–33560.

(178) Bouhours, D.; Bouhours, J.-F. Developmental Changes of the Lipidic Part of the Neutral Glycosphingolipids of the Rat Stomach. *J. Biol. Chem.* **1985**, *260* (4), 2172–2177.

(179) Okabe, K.; Keenan, R. W.; Schmidt, G. Phytosphingosine Groups as Quantitatively Significant Components of the Sphingolipids of the Mucosa of the Small Intestines of Some Mammalian Species. *Biochem. Biophys. Res. Commun.* **1968**, *31* (1), 137–143.

(180) Umesaki, Y.; SUZUKI, A.; KASAMA, T.; TOHYAMA, K.; MUTAI, M.; YAMAKAWA, T. Presence of Asialo GM, and Glucosylceramide in the Intestinal Mucosa of Mice and Induction of Fucosyl Asialo GM, by Conventionalization of Germ-Free Mice. *J. Biochem.* **1981**, *90* (6), 1731–1738.

(181) Kaye, E. M.; Ullman, M. D. Separation and Quantitation of Perbenzoylated Glucocerebroside and Galactocerebroside by High-Performance Liquid Chromatography. *Anal. Biochem.* **1984**, *138* (2), 380–385.

(182) Adams, E. P.; Gray, G. M. The Carbohydrate Structures of the Neutral Ceramide Glycolipids in Kidneys of Different Mouse Strains with Special Reference to the Ceramide Dihexosides. *Chem. Phys. Lipids* **1968**, *2* (2), 147–155.

(183) Marsching, C.; Rabionet, M.; Mathow, D.; Jennemann, R.; Kremser, C.; Porubsky, S.; Bolenz, C.; Willecke, K.; Grone, H.-J.; Hopf, C.; et al. Renal Sulfatides: Sphingoid Base-Dependent Localization and Region-Specific Compensation of CerS2-Dysfunction. *J. Lipid Res.* **2014**, *55* (11), 2354–2369.

(184) Körschen, H. G.; Yildiz, Y.; Raju, D. N.; Schonauer, S.; Bönigk, W.; Jansen, V.; Kremmer, E.; Kaupp, U. B.; Wachten, D. The Non-Lysosomal β-Glucosidase GBA2 Is a Non-Integral Membrane-Associated Protein at the Endoplasmic Reticulum (ER) and Golgi. *J. Biol. Chem.* **2013**, *288* (5), 3381–3393.

(185) Yildiz, Y.; Hoffmann, P.; Vom Dahl, S.; Breiden, B.; Sandhoff, R.; Niederau, C.; Horwitz, M.; Karlsson, S.; Filocamo, M.; Elstein, D.; et al. Functional and Genetic Characterization of the Non-Lysosomal Glucosylceramidase 2 as a Modifier for Gaucher Disease. *Orphanet J. Rare Dis.* **2013**, *8*, 151.

(186) Kishimoto, Y.; Radin, N. S. Occurrence of 2-Hydroxy Fatty Acids in Animal Tissues. *J. Lipid Res.* **1963**, *4* (2), 139–143.

(187) Hammarström, S. Configuration of 2-hydroxy Acids from Brain Cerebrosides Determined by Gas Chromatography. *FEBS Lett.* **1969**, *5* (3), 192–195.

(188) Eckhardt, M.; Yaghootfam, A.; Fewou, S. N.; Zöller, I.; Gieselmann, V. A Mammalian Fatty Acid Hydroxylase Responsible for the Formation of α-Hydroxylated Galactosylceramide in Myelin.

Biochem. J. **2005**, *388* (1), 245–254.

(189) Guo, L.; Zhang, X.; Zhou, D.; Okunade, A. L.; Su, X. Stereospecificity of Fatty Acid 2-Hydroxylase and Differential Functions of 2-Hydroxy Fatty Acid Enantiomers. *J. Lipid Res.* **2012**, *53* (7), 1327–1335.

(190) Haig, N. A.; Guan, Z.; Li, D.; McMichael, A.; Raetz, C. R. H.; Xu, X.-N. Identification of Self-Lipids Presented by CD1c and CD1d Proteins. *J. Biol. Chem.* **2011**, *286* (43), 37692–37701.

(191) Miyagawa, E.; AZUMA, R.; SUTO, T.; YANO, I. Occurrence of Free Ceramides in Bacteroides Fragilis NCTC 9343. *J. Biochem.* **1979**, *86* (2), 311–320.

(192) Arora, T.; Sharma, R. Fermentation Potential of the Gut Microbiome: Implications for Energy Homeostasis and Weight Management. *Nutr. Rev.* **2011**, *69* (2), 99–106.

(193) Valdearcos, M.; Robblee, M. M.; Benjamin, D. I.; Nomura, D. K.; Xu, A. W.; Koliwad, S. K. Microglia Dictate the Impact of Saturated Fat Consumption on Hypothalamic Inflammation and Neuronal Function. *Cell Rep.* **2014**, *9* (6), 2124–2139.

(194) Hsu, F.-F.; Bohrer, A.; Turk, J. Formation of Lithiated Adducts of Glycerophosphocholine Lipids Facilitates Their Identification by Electrospray Ionization Tandem Mass Spectrometry. *J. Am. Soc. Mass Spectrom.* **1998**, *9* (5), 516–526.

(195) Huang, N.; Siegel, M. M.; Kruppa, G. H.; Laukien, F. H. Automation of a Fourier Transform Ion Cyclotron Resonance Mass Spectrometer for Acquisition, Analysis, and e-Mailing of High-Resolution Exact-Mass Electrospray Ionization Mass Spectral Data. *J. Am. Soc. Mass Spectrom.* **1999**, *10* (11), 1166–1173.

(196) Gross, S. K.; McCluer, R. H. High-Performance Liquid Chromatographic Analysis of Neutral Glycosphingolipids as Their per-O-Benzoyl Derivatives. *Anal. Biochem.* **1980**, *102* (2), 429–433.

(197) Hellerqvist, C. G.; Rudén, U.; Mäkelä, P. H. The Group C2-Type Modification of the B-Type Lipopolysaccharide in a Hybrid between Salmonella Groups B and C2. *FEBS J.* **1972**, *25* (1), 96–101.

(198) Waeghe, T. J.; Darvill, A. G.; McNeil, M.; Albersheim, P. Determination, by Methylation Analysis, of the Glycosyl-Linkage Compositions of Microgram Quantities of Complex Carbohydrates. *Carbohydr. Res.* **1983**, *123* (2), 281–304.

(199) Domon, B.; Mueller, D. R.; Richter, W. J. Tandem Mass Spectrometric Analysis of Fixed-charge Derivatized Oligosaccharides. *J. Mass Spectrom.* **1994**, *29* (12), 713–719.

(200) Liptáak, M.; Heerma, W. Fast-atom Bombardment Mass Spectrometric Study of Some N-and S-glycosides of Acetylated Hexose Isomers. *Rapid Commun. mass Spectrom.* **1993**, *7* (7), 676–679.

(201) Egge, H.; Peter-Katalinić, J. Fast Atom Bombardment Mass Spectrometry for Structural Elucidation of Glycoconjugates. *Mass Spectrom. Rev.* **1987**, *6* (3), 331–393.

(202) Timur, Z. K.; Demir, S. A.; Marsching, C.; Sandhoff, R.; Seyrantepe, V. Neuraminidase-1 Contributes Significantly to the Degradation of Neuronal B-Series Gangliosides but Not to the Bypass of the Catabolic Block in Tay–Sachs Mouse Models. *Mol. Genet. Metab. reports* **2015**, *4*, 72–82.

(203) Wada, T.; Hata, K.; Yamaguchi, K.; Shiozaki, K.; Koseki, K.; Moriya, S.; Miyagi, T. A Crucial Role of Plasma Membrane-Associated Sialidase in the Survival of Human Cancer Cells. *Oncogene* **2007**, *26* (17), 2483–2490.

(204) Hakomori, S.; Handa, K. Regulation of Growth Factor Receptors by Glycosphingolipids. In *Glycosignals in Cancer: Mechanisms of Malignant Phenotypes*; Springer Japan: Tokyo, 2016; pp 77–93.

(205) Prentice, B. M.; Caprioli, R. M. The Need for Speed in Matrix-Assisted Laser Desorption/Ionization Imaging Mass Spectrometry. *Postdoc J. a J. Postdr. Res. Postdr. Aff.* **2016**, *4* (3), 3–13.

(206) Hasegawa, T.; Yamaguchi, K.; Wada, T.; Takeda, A.; Itoyama, Y.; Miyagi, T. Molecular Cloning of Mouse Ganglioside Sialidase and Its Increased Expression in Neuro2a Cell Differentiation. *J. Biol. Chem.* **2000**, *275* (11), 8007–8015.

(207) Han, X.; Yang, K.; Gross, R. W. Multi-Dimensional Mass Spectrometry-Based Shotgun Lipidomics and Novel Strategies for Lipidomic Analyses. *Mass Spectrom. Rev.* **2012**, *31* (1), 134–178.

(208) Merrill, A. H.; Sullards, M. C. Opinion Article on Lipidomics: Inherent Challenges of Lipidomic Analysis of Sphingolipids. *Biochim. Biophys. Acta - Mol. Cell Biol. Lipids* **2017**, *1862* (8), 774–776.

(209) Surma, M. A.; Herzog, R.; Vasilj, A.; Klose, C.; Christinat, N.; Morin-Rivron, D.; Simons, K.; Masoodi, M.; Sampaio, J. L. An Automated Shotgun Lipidomics Platform for High Throughput, Comprehensive, and Quantitative Analysis of Blood Plasma Intact Lipids. *Eur. J. Lipid Sci. Technol.* **2015**, *117* (10), 1540–1549.

(210) Yildiz, Y.; Hoffmann, P.; vom Dahl, S.; Breiden, B.; Sandhoff, R.; Niederau, C.; Horwitz, M.; Karlsson, S.; Filocamo, M.; Elstein, D.; et al. Functional and Genetic Characterization of the Non-Lysosomal Glucosylceramidase 2 as a Modifier for Gaucher Disease. *Orphanet J. Rare Dis.* **2013**, *8* (1), 151.

(211) Walden, C. M.; Sandhoff, R.; Chuang, C.-C.; Yildiz, Y.; Butters, T. D.; Dwek, R. A.; Platt, F. M.; van der Spoel, A. C. Accumulation of Glucosylceramide in Murine Testis, Caused by Inhibition of Beta-Glucosidase 2: Implications for Spermatogenesis. *J. Biol. Chem.* **2007**, *282* (45), 32655–32664.

(212) Ogawa, D.; Shikata, K.; Honke, K.; Sato, S.; Matsuda, M.; Nagase, R.; Tone, A.; Okada, S.; Usui, H.; Wada, J.; et al. Cerebroside Sulfotransferase Deficiency Ameliorates L-Selectin-Dependent Monocyte Infiltration in the Kidney after Ureteral Obstruction. *J. Biol. Chem.* **2004**, *279* (3), 2085–2090.

(213) Imgrund, S.; Hartmann, D.; Farwanah, H.; Eckhardt, M.; Sandhoff, R.; Degen, J.; Gieselmann, V.; Sandhoff, K.; Willecke, K. Adult Ceramide Synthase 2 (CERS2)-Deficient Mice Exhibit Myelin Sheath Defects, Cerebellar Degeneration, and Hepatocarcinomas. *J. Biol. Chem.* **2009**, *284* (48), 33549–33560.

(214) Ginkel, C.; Hartmann, D.; vom Dorp, K.; Zlomuzica, A.; Farwanah, H.; Eckhardt, M.; Sandhoff,

R.; Degen, J.; Rabionet, M.; Dere, E.; et al. Ablation of Neuronal Ceramide Synthase 1 in Mice Decreases Ganglioside Levels and Expression of Myelin-Associated Glycoprotein in Oligodendrocytes. *J. Biol. Chem.* **2012**, *287* (50), 41888–41902.

(215) Kawano, T.; Cui, J.; Koezuka, Y.; Toura, I.; Kaneko, Y.; Motoki, K.; Ueno, H.; Nakagawa, R.; Sato, H.; Kondo, E.; et al. CD1d-Restricted and TCR-Mediated Activation of Valpha14 NKT Cells by Glycosylceramides. *Science* **1997**, *278* (5343), 1626–1629.

(216) Brossay, L.; Chioda, M.; Burdin, N.; Koezuka, Y.; Casorati, G.; Dellabona, P.; Kronenberg, M. CD1d-Mediated Recognition of an α-Galactosylceramide by Natural Killer T Cells Is Highly Conserved through Mammalian Evolution. *J. Exp. Med.* **1998**, *188* (8), 1521–1528.

(217) Pereira, C. S.; Azevedo, O.; Maia, M. L.; Dias, A. F.; Sa-Miranda, C.; Macedo, M. F. Invariant Natural Killer T Cells Are Phenotypically and Functionally Altered in Fabry Disease. *Mol. Genet. Metab.* **2013**, *108* (4), 241–248.

(218) Darmoise, A.; Teneberg, S.; Bouzonville, L.; Brady, R. O.; Beck, M.; Kaufmann, S. H. E.; Winau, F. Lysosomal α-Galactosidase Controls the Generation of Self Lipid Antigens for Natural Killer T Cells. *Immunity* **2010**, *33* (2), 216–228.

(219) Han, X.; Cheng, H. Characterization and Direct Quantitation of Cerebroside Molecular Species from Lipid Extracts by Shotgun Lipidomics. *J. Lipid Res.* **2004**, *46* (1), 163–175.

(220) Han, X. Characterization and Direct Quantitation of Ceramide Molecular Species from Lipid Extracts of Biological Samples by Electrospray Ionization Tandem Mass Spectrometry. **2002**.

(221) Brennan, P. J.; Cheng, T.-Y.; Pellicci, D. G.; Watts, G. F. M.; Veerapen, N.; Young, D. C.; Rossjohn, J.; Besra, G. S.; Godfrey, D. I.; Brenner, M. B.; et al. Structural Determination of Lipid Antigens Captured at the CD1d-T-Cell Receptor Interface. *Proc. Natl. Acad. Sci. U. S. A.* **2017**, *114* (31), 8348–8353.

6 List of abbreviations

AcOH	acetic acid
AdS	α-hydroxy and dihydrosphingosine
a-GSL	acidic glycosphingolipids
Alb	albumin
AP	α-hydroxy and phytosphingosine
APC	antigen presenting cells
Ar	argon
AS	α-hydroxy and sphingosine
B4Galnt1	N-acetylgalactosaminyl transferase
BdS	β-hydroxy and dihydrosphingosine
Bl6	black 6 mouse strain
CamK	calcium/calmodulin-dependent kinase II α
CD1d	cluster of differentiation 1d
Cer	ceramide
CerS	ceramide synthase
CERT	ceramide transfer protein
CID	collision induced dissociation
Cnp	2', 3' cyclic nucleotide 3' phosphodiesterase
CNS	central nervous system
Cre	cyclization recombinase
CST	cerebroside sulfotransferase
DEAE	Diethylaminoethylcellulose
DES	dihydroceramide desaturase
DESI	Desorption electrospry ionization
DETA	diethylentriamine
DHB	2,5-dihydrobenzoic acid
dS	dihydrosphingosine
dw	dry weight
EGFR	epidermal growth factor receptor
eLPA	ether-bonded lyso phosphatidic acid
ER	endoplasmativ reticulum
ESCRT	endosomal sorting complexes required for transport
ESI	electrospray ionization
EtOH	ethanol
eV	electron voltage/energy

f/f	floxed/floxed
FA	fatty acid
Fa2h	fatty acid 2 hydroxylase
FS	full scan
GalCer	Galactosylceramide
Galgt1	N-acetylgalactosaminyl transferase
GalNAc	N-acetyl galactosamine
Gb3S	Gb3 synthase
Gba2	non-lysosomal β-glucosylceramidase
GC	gas chromatography
GD3S	GD3 synthase
GG	Ganglioside
GlcCer	Glucosylceramide
GM2AP	GM2 activator protein
GM3S	GM3 synthase
GSL	glycosphingolipid
H	hydrogen
H&E	hematoxiln and eosin
HexA	Hexosaminidase A
HexCer	Hexosylceramide
HexNac	N-acetyl hexosamine
HFD	high fat diet
HILIC	hydrophilic interaction chromatography
HPTLC	high performance rhin layer chromatography
iNKT	invariant natural killer T cells
ISD	internal standard
ISD	in-source decay
ITO	indium tin oxide
K14	keratinocyte 14
KDSR	3-ketosphinganine reductase
LacCer	lactosylceramide
LC	Liquid chromatography
loxP	locus of crossing x over P
LPC	lyso phospahtidylcholine
LV	luminal vesicle
M	mass ion

m/z	mass over charge
MALDI	Matrix assisted laser desorption/ionization
MRM	multi reaction monitoring
MS/MS	Tandem mass spectrometry
MS^2	Tandem mass spectrometry
MSI	Mass spectrometry imaging
Nd:YAG	neodymium-doped yttrium aluminum garnet
NdS	non-hydroxy and dihydrosphingosine
Neu	neuraminidase
NeuAc	neuraminic acid
n-GSL	neutral glycosphingolipids
NP	non-hydroxy and phytosphingosine
NS	non-hydroxy and sphingosine
Pax8	paired box protein 8
PBS	phosphate buffered saline
PC	phosphatidylcholine
PI	phosphatidylinositol
pLPE	ether-bonded lyso phosphoethanolamine
PNS	peripheral nervous system
PS	phosphatidylserine
PS	precursor scan
QqQ	Triple quadrupole
R	resolution
Rf	retenrion factor
RP	reversed phase
RT	retenrion time
Rt	retenrion time
SAP	saposin
SM	sphingomyelin
So	sphingosine
SPT	serine palmitoyl transferase
SRM	single reaction monitoring
St3galt5	GM3/GM4 - sialyltransferase
St8sia1	GD3 synthase
TCR	T cell receptor
TFA	triflour acetic acid

TGN	trans-golgi network
TIC	total ion current
TLC	thin layer chromatography
TOF	time-of-flight
TSD	Tay-Sachs disease
Ugcg	GlcCer synthase
Ugt8a	GalCer synthase
UPLC	ultra performace liquid chromatography
Vil	villi
WT	wildtype
wt	wildtype
ww	wet weight

7 Acknowledgements

First, I would like to thank my Supervisor Dr. Roger Sandhoff for accepting me as a doctoral student in his group and his inspiring guidance. I very much appreciated his enthusiasm for science, his bride knowledge and the stimulating discussions. His trust and encouragement in challenging situations were indispensable to successfully accomplish this project.

I also would like to express my gratitude towards Prof. Dr. Hermann-Josef Gröne for the opportunity to pursue my thesis in his laboratory.

Thanks to Volkan Seyrantepe and his Laboratory from the University of Izmir for the great collaboration and scientific discussions.

Furthermore, I would like to thank the members of the examination committee and thesis advisory committee Prof. Matthias Mayer, Dr. Guoliang Cui and Prof. Sabine Strahl for constructive criticism and valuable ideas for the project and thesis.

Most especially I would like to thank Dr. Carsten Hopf and his laboratory from the University of Applied Sciences Mannheim for the collaboration and scientific advices.

Thanks to all the members of the department for technical advice and support, especially Dominic Lamprecht for all the work he invested during his Bachelor and Master Thesis, Benita von Tümpling-Radosta for all the lipid extractions, Richard Jennemann for whatever advice was needed, and Dr. Viola Nordström and Dr. Silke Herzer for the special Brain/Neuron knowledge.

8 Appendix

Gradient #1
A 50 MeOH 50 H2O
B 99 isoProp 1 MeOH
10 mM Amform 0.1% FA

Time(min)	Flow Rate	%A	%B	Curve
Initial	0.450	60.0	40.0	Initial
0.20	0.450	60.0	40.0	8
5.50	0.450	10.0	90.0	8
7.00	0.450	10.0	90.0	6
7.25	0.450	60.0	40.0	6
9.00	0.450	60.0	40.0	6

Gradient #2
A 50 MeOH 50 H2O
B 99 isoProp 1 MeOH
10 mM Amform 0.1% FA

Time(min)	Flow Rate	%A	%B	Curve
Initial	0.450	60.0	40.0	Initial
0.10	0.450	60.0	40.0	6
1.00	0.450	45.0	55.0	6
5.50	0.450	15.0	85.0	6
7.00	0.450	15.0	85.0	6
7.25	0.450	60.0	40.0	6
9.00	0.450	60.0	40.0	6

Gradient #3
A 60 ACN 40 H2O
B 99 isoProp 1 MeOH
10 mM Amform 0.1% FA

Time(min)	Flow Rate	%A	%B	Curve
Initial	0.450	60.0	40.0	Initial
0.20	0.450	60.0	40.0	8
5.50	0.450	10.0	90.0	8
7.00	0.450	10.0	90.0	6
7.25	0.450	60.0	40.0	6
9.00	0.450	60.0	40.0	6

Gradient #4
A 60 ACN 40 H2O
B 99 isoProp 1 MeOH
10 mM Amform 0.1% FA

Time(min)	Flow Rate	%A	%B	Curve
Initial	0.450	50.0	50.0	Initial
0.10	0.450	50.0	50.0	6
5.50	0.450	15.0	85.0	6
7.00	0.450	10.0	90.0	6
7.25	0.450	50.0	50.0	6
8.00	0.450	50.0	50.0	6

Gradient #5
A 60 ACN 40 H2O
B 99 isoProp 1 MeOH
10 mM Amform 0.1% FA

Time(min)	Flow Rate	%A	%B	Curve
Initial	0.450	50.0	50.0	Initial
0.10	0.450	50.0	50.0	8
5.50	0.450	15.0	85.0	8
7.00	0.450	10.0	90.0	6
7.25	0.450	50.0	50.0	6
8.00	0.450	50.0	50.0	6

Gradient #6
A 60 ACN 40 H2O 10 mM Amform 0.1% FA
B 78 isoProp 20 MeOH 2 H2O 10 mM Amform

Time(min)	Flow Rate	%A	%B	Curve
Initial	0.450	70.0	30.0	Initial
0.10	0.450	70.0	30.0	6
5.50	0.450	10.0	90.0	6
7.00	0.450	10.0	90.0	6
7.25	0.450	70.0	30.0	6
8.00	0.450	70.0	30.0	6

Gradient #7
A 60 ACN 40 H2O 10 mM Amform 0.1% FA
B 78 isoProp 20 MeOH 2 H2O 10 mM Amform

Time(min)	Flow Rate	%A	%B	Curve
Initial	0.450	60.0	40.0	Initial
0.10	0.450	60.0	40.0	6
5.50	0.450	20.0	80.0	6
7.00	0.450	10.0	90.0	6
7.25	0.450	60.0	40.0	6
8.00	0.450	60.0	40.0	6

Appendix I: Solvent systems tested as gradients for the analysis of gangliosides with BEH C18 (50x2.1) column.

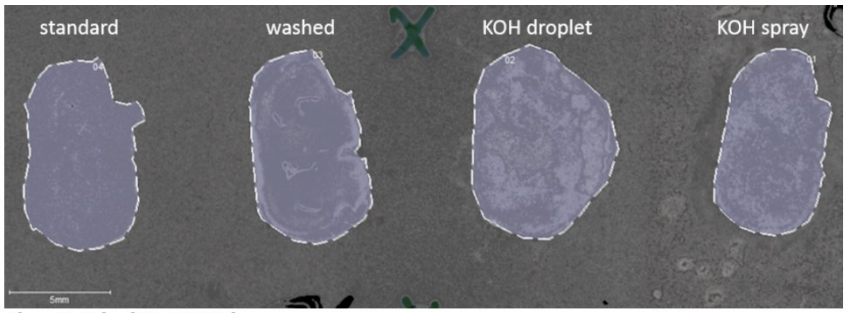

1) **standard: untreated**
2) **washed: 2x20µL 10% CH_3COOH**
3) **KOH droplet: 0.1M KOH in 10%MeOH directly on tissue & wash**
4) **KOH spray: 0.1M KOH in 10% MeOH sprayed 5x20µL/min & wash**

→ **All incubated in SunDigest: 2h, 37°C, 95% humidity**

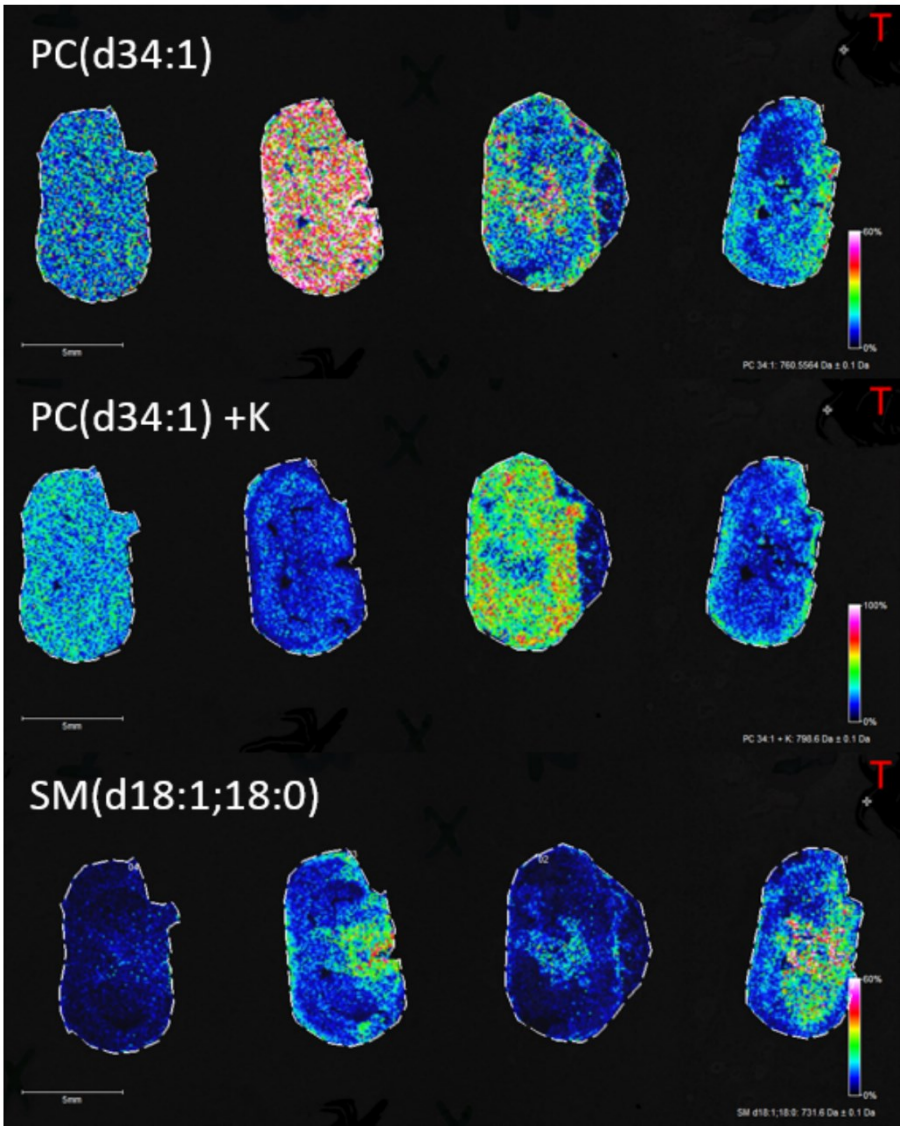

Appendix II: MALDI-TOF test of on-tissue saponification with 0.1M KOH. Fresh frozen WT mouse brain slices were either untreated, washed with 10% acetic acid or treated with 0.1M KOH as spray or droplet and washed. DHB matrix was applied and phosphocholine (PC) and sphingomyelin (SM) measured in positive reflector mode with a spatial resolution of 100 µm.

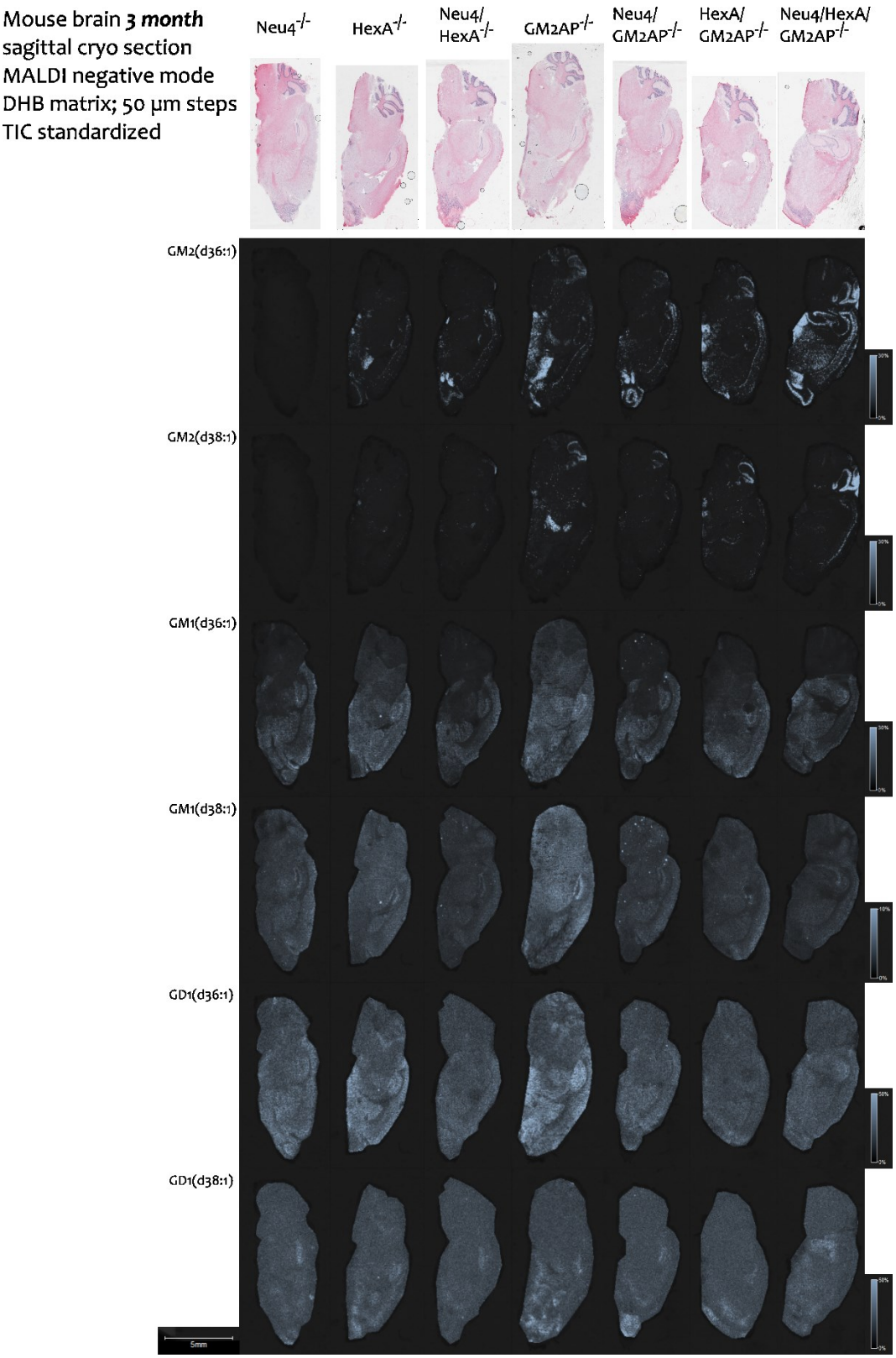

Appendix III: Mass spectrometry imaging with MALDI-TOF of gangliosides. Fresh frozen slices of mouse brain from 3 month old GM2 gangliosidosis mice with Neu4 deficiency were sprayed with DHB matrix and measured in reflector negative mode with a spatial resolution of 50 µm.

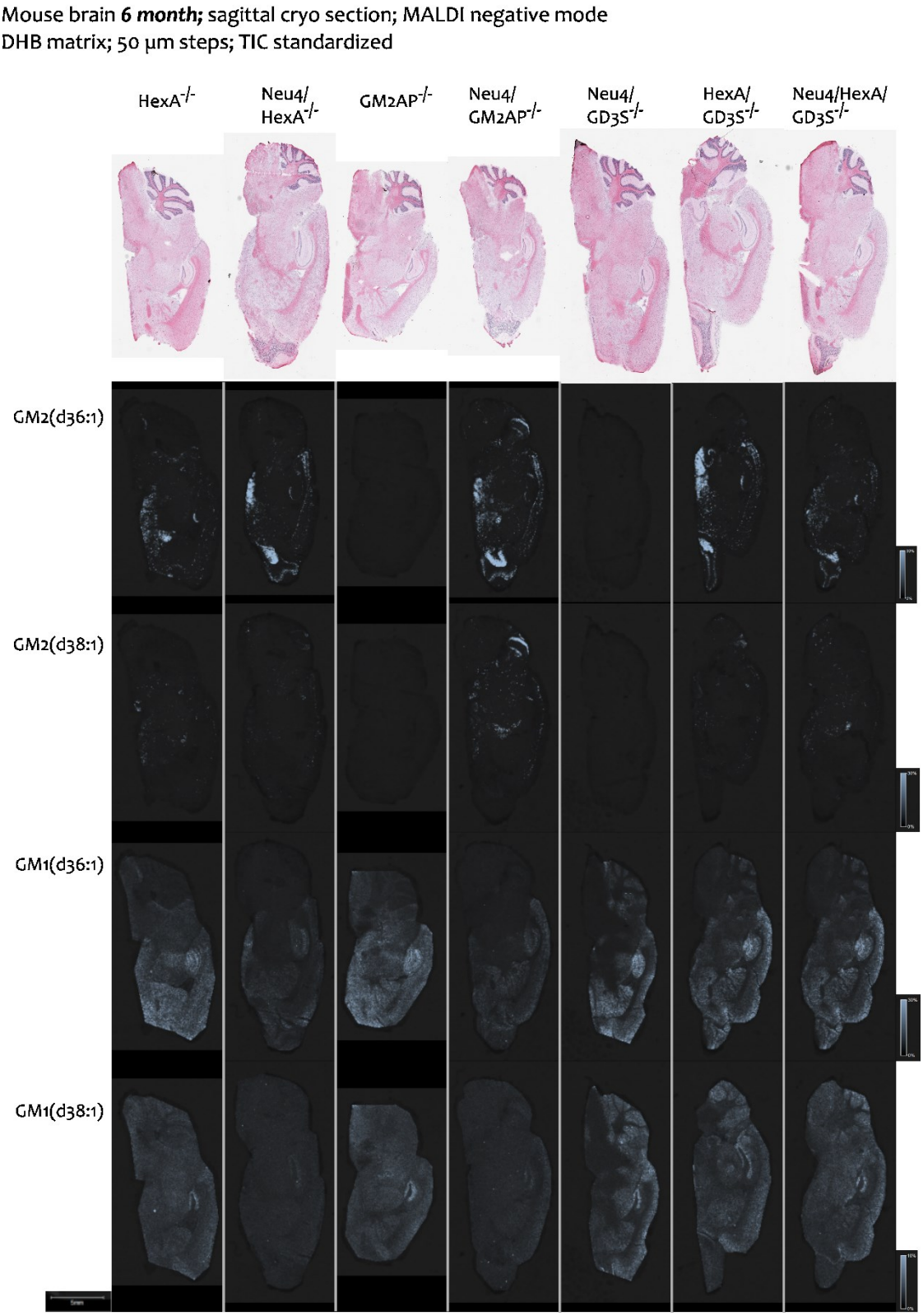

Appendix IV: Mass spectrometry imaging with MALDI-TOF of gangliosides. Fresh frozen slices of mouse brain from 6 month old GM2 gangliosidosis mice with Neu4 deficiency were sprayed with DHB matrix and measured in reflector negative mode with a spatial resolution of 50 µm.

Anchor:	**(d17:0;h17:0)**			**(d18:0;h17:0)**			**(d19:0;h17:0)**		
Compound:	**HexCer**		**Cer**	**HexCer**		**Cer**	**HexCer**		**Cer**
	[pmol/mg dry weight]		[A.U.][a]	[pmol/mg dry weight]		[A.U.]	[pmol/mg dry weight]		[A.U.]
Mode:	**HILIC**	**RP18**		**HILIC**	**RP18**		**HILIC**	**RP18**	
Strain									
B. ovatus	0.08[b]	0.04	0.35 ±0.27[c]	0.02	n.d.	0.54 ±0.37	0.02	n.d.	0.70 ±0.47
B. thetaio-taomicron	0.06 ±0.02	0.04	0.40 ±0.03	0.02	n.d.	0.60 ±0.01	0.06	0.05	0.64 ±0.05
B. intestinalis	0.04 ±0.02	n.d.	n.d.	0.02	n.d.	n.d.	0.02	0.05	n.d.
B. caccae	0.06 ±0.02	n.d.	n.d.	0.03	n.d.	0.06 ±0.01	0.05 ±0.03	0.1	n.d.
B. uniformis	0.05	n.d.	0.13 ±0.04	n.d.	n.d.	0.29	0.02 ±0.02	n.d.	0.55 ±0.4
Lacto-bacillus	0.04	0.02	n.d.	n.d.	0.04	n.d.	n.d.	0.08	n.d.
Bifido-bacterium	0.05	n.d.	n.d.	0.02	n.d.	n.d.	n.d.	0.05	n.d.

[a] A.U. are arbitrary units of the peak area as compared to the internal HexCer standard.

[b] If single values are plotted, the compound was only detected in one out of two samples.

[c] n = 2.

Appendix V: LC-MS² detection of sphingolipids in different bacteria of the human gut microbiome.